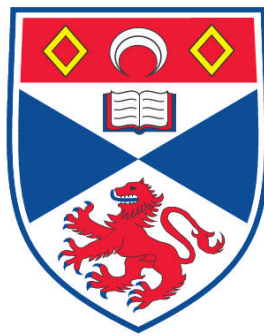# ALTERNATIVE TECHNIQUES FOR THE PRODUCTION AND MANIPULATION OF ULTRACOLD ATOMS

## Graham D. Bruce

## A Thesis Submitted for the Degree of PhD
## at the
## University of St. Andrews

**2012**

# Alternative Techniques for the Production and Manipulation of Ultracold Atoms

## Graham D. Bruce
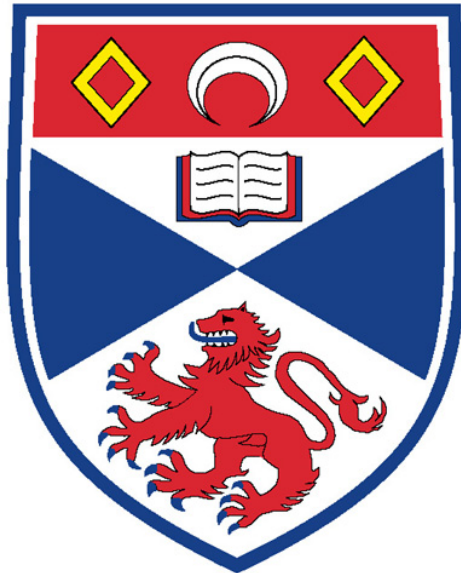
Thesis submitted for the degree of Doctor of Philosophy
of the University of St Andrews

24th January, 2012

# Abstract

This Thesis contains details of the construction and characterisation of a compact apparatus for the cooling of ultracold atoms to quantum degeneracy, and their manipulation in flexible holographic optical traps. We have designed and built two iterations of this apparatus. The first version consists of a stainless steel single-cell vacuum chamber, in which we confine $^{87}$Rb and $^6$Li or $^7$Li in a Magneto-Optical Trap. We characterise the alternative methods of pulsed atomic dispenser and Light Induced Atomic Desorption (LIAD) to rapidly vary the background pressure in the vacuum chamber with the view to enabling efficient evaporative cooling in the single chamber, loading MOTs of up to $10^8$ atoms using pulsed dispensers. The LIAD is found to be ineffective in loading large MOTs in this setup, while the pulsed dispensers method gradually increases the background pressure in the chamber over time.

Based on the results of this first iteration, we designed and built a second single-chamber apparatus for cooling of $^{87}$Rb to quantum degeneracy. The LIAD technique was used to successfully load MOTs containing $8 \times 10^7$ atoms in this single pyrex cell with a rapidly-varying background pressure. The lifetime of an atomic cloud loaded from the MOT into a magnetic trap increased by a factor of 6 when LIAD was used.

The holographic optical traps for cold atoms are generated using a Spatial Light Modulator, and we present our novel method for improving the quality of holographic light patterns to the point where they are suitable for trapping ultracold atoms using a feedback algorithm. As demonstrations of this new capability, we show power-law optical traps which provide an efficient, reversible route to Bose-Einstein Condensation and a dynamic ring trap for the investigation of superfluidity in cold atoms.

# Declaration

I, Graham David Bruce, hereby certify that this thesis, which is approximately 39,000 words in length, has been written by me, that it is the record of work carried out by me and that it has not been submitted in any previous application for a higher degree.

I was admitted as a research student in October 2007 and as a candidate for the degree of Doctor of Philosophy in October 2007; the higher study for which this is a record was carried out in the University of St Andrews between 2007 and 2011.

date: 24-Jan-12    signature of candidate:

I hereby certify that the candidate has fulfilled the conditions of the Resolution and Regulations appropriate for the degree of Doctor of Philosophy in the University of St Andrews and that the candidate is qualified to submit this thesis in application for that degree.

date: 24-Jan-12    signature of supervisor:

In submitting this thesis to the University of St Andrews we understand that we are giving permission for it to be made available for use in accordance with the regulations of the University Library for the time being in force, subject to any copyright vested in the work not being affected thereby. We also understand that the title and the abstract will be published, and that a copy of the work may be made and supplied to any bona fide library or research worker, that my thesis will be electronically accessible for personal or research use unless exempt by award of an embargo as requested below, and that the library has the right to migrate my thesis into new electronic forms as required to ensure continued access to the thesis. We have obtained any third-party copyright permissions that may be required in order to allow such access and migration, or have requested the appropriate embargo below.

The following is an agreed request by candidate and supervisor regarding the electronic publication of this thesis:

Access to Printed copy and electronic publication of thesis through the University of St Andrews.

date: 24-Jan-12    signature of candidate:

date: 24-Jan-12    signature of supervisor:

iv

# Acknowledgements

I must firstly thank Donatella Cassettari for giving me my initial insight into cold atomic physics back in the "recruitment lecture" of 2005/6, and then for putting up with me for the subsequent summer, MPhys and now PhD projects. You have been an ever-reliable source of ideas, clarifications and education, a great mentor and a good friend.

My time in the lab has mostly been shared with Lara Torralbo-Campo, who has been an excellent colleague, I think we've driven each other mad at times but have achieved a great deal together. In the early days, David Gherardi was an excellent source of borrowed equipment and always available for advice, while our postdoc Giuseppe Smirne has been a great friend, educator and proof-reader since his arrival in 2008.

I have been fortunate to work with a large number of talented and ambitious undergraduate students in both the cold atoms and the SLM lab, whose efforts greatly contributed to the success of the lab. In chronological order, thanks to Martin, Taka, Sarah, James, Joseph, Tiffany, Caroline, Ed, Alistair, Steven, Pierre and David! My knowledge of the state-of-the-art within the field of cold atoms was helped immensely by the regular meetings of the Cold Atoms Discussion Group, so I would like to thank all the contributors since we started in 2008.

Outside the lab, the departmental technicians and secretaries have provided invaluable support over the years, while the other inhabitants of 112 have always been willing to lend a hand, whether loaning equipment or literally providing pairs of hands for those awkward tasks that seem to come around with alarming frequency. The greater population of the physics department have been a very friendly community and made it very hard for me to leave St Andrews. Thanks especially to those who have involved me in other areas of department life, particularly in teaching and outreach: two activities that have been an absolute pleasure to take part in when not in the lab.

A large part of the writing of this thesis has taken place since my move to Strathclyde, and I must thank all my coworkers there for checking up on me and making sure that the writing progressed steadily and smoothly. Special mention to Jon Pritchard for proof-reading the introduction to this thesis!

My parents, sister Gillian and the rest of my extended family have been a source of love, encouragement and support my whole life, and that certainly continued during the PhD years. I am indebted to you in so many ways, and this acknowledgment does not come close to expressing how thankful I am. The Trimbles and their extended family also deserve thanks for welcoming me with open arms and supporting me in this venture.

My final thanks must be reserved for my wife Leanne. You've been my constant companion through this whole journey supporting me and I couldn't have achieved this without you. Thanks for reminding me that there's more to life than the inside of the lab, while still understanding on those occasions that I have to be there at odd hours. I can never thank you or love you too much.

# Publications and Presentations

## Journal publications

1. Graham D. Bruce, Sarah L. Bromley, Giuseppe Smirne, Lara Torralbo-Campo and Donatella Cassettari, "Holographic power-law traps for the efficient production of Bose-Einstein condensates", Phys. Rev. A **84**, 053410 (2011)

2. Graham D. Bruce, James Mayoh, Giuseppe Smirne, Lara Torralbo-Campo and Donatella Cassettari, "A smooth, holographically generated ring trap for the investigation of superfluidity in ultracold atoms", Phys. Scr. **T143**, 014008 (2011)

## Oral presentations

1. "Novel Optical Traps for Ultracold Atoms", Seminar, Universität Basel, May 2011

2. "Novel Optical Traps for Ultracold Atoms", Seminar, University of Strathclyde, May 2011

3. "Novel Optical Traps for Ultracold Atoms", Seminar, University of Sussex, May 2011

4. "Novel Optical Traps for Ultracold Atoms", Seminar, Universität Stuttgart, May 2011

5. "Novel Optical Traps for Ultracold Atoms", SUPA AGM, University of St Andrews, March 2011

6. "Exotic Optical Traps for Ultracold Atoms", UK Network for Research at the Interface Between Cold-Atom and Condensed Matter Physics Annual Meeting, University of St Andrews, August 2010

## Poster presentations

1. Lara Torralbo-Campo, Graham D. Bruce, Giuseppe Smirne, and Donatella Cassettari, "A Compact System for Ultracold Atoms", Condensed Matter and Materials Physics 2011, University of Manchester, December 2011

2. Lara Torralbo-Campo, Graham D. Bruce, Giuseppe Smirne, and Donatella Cassettari, "Towards Ultracold Atoms in Exotic Optical Traps", UK Network for Research at the Interface Between Cold-Atom and Condensed Matter Physics Annual Meeting, University of St Andrews, August 2010

3. Lara Torralbo-Campo, Graham D. Bruce, Giuseppe Smirne, and Donatella Cassettari, "Towards Ultracold Atoms in Exotic Optical Traps", International Conference on Atomic Physics XXII, Cairns, Tropical North Queensland, Australia, July 2010

4. Graham D. Bruce, James Mayoh, Lara Torralbo-Campo, Giuseppe Smirne, and Donatella Cassettari, "Exotic optical traps for ultracold atoms", 17th Central European Workshop on Quantum Optics, University of St Andrews, June 2010

5. Lara Torralbo-Campo, Graham D. Bruce, Giuseppe Smirne, and Donatella Cassettari, "Towards Ultracold Atoms in Arbitrary Optical Lattices", Condensed Matter and Materials Physics 2009, University of Warwick, December 2009

6. Giuseppe Smirne, Graham D. Bruce, Lara Torralbo-Campo, Victoria C. Chan, and Donatella Cassettari, "Towards sympathetic cooling of a Bose-Fermi mixture", Bose-Einstein Condensation, Les Houches Pre-doc School, October 2008

7. Giuseppe Smirne, Graham D. Bruce, Lara Torralbo-Campo, Victoria C. Chan, and Donatella Cassettari, "Towards sympathetic cooling of a Bose-Fermi mixture", Cold Atoms and Optical Lattices, University of Oxford, September 2008

8. Giuseppe Smirne, Graham D. Bruce, Lara Torralbo-Campo, Victoria C. Chan, and Donatella Cassettari, "Towards sympathetic cooling of a Bose-Fermi mixture", International Conference on Atomic Physics XXI, University of Connecticut, July 2008

# Contents

# Chapter 1

# The production and manipulation of ultracold atomic gases

## 1.1 Bose-Einstein Condensation

For a quantum system of $N$ indistinguishable particles at temperature $T$, the number of particles $n$ with energy $\epsilon$ is given by the Maxwell-Boltzmann distribution

$$n_{MB}(\epsilon) = g(\epsilon) \exp[(\mu - \epsilon)/k_B T], \tag{1.1}$$

where $k_B$ is the Boltzmann constant, $g(\epsilon)$ is the density of states and $\mu$ is the chemical potential (loosely, the energy required to add another particle to the system), provided that there is little competition for states, i.e. $g(\epsilon) >> n(\epsilon)$ [1].

As the temperature of the ensemble decreases, the average number of particles at low energy levels will increase, and (1.1) will no longer hold. The statistics that particles obey now depends on their fundamental nature.

If two identical particles are symmetric with respect to exchange, they are called bosons and have integer spin (in units of $\hbar$), whilst if they are anti-symmetric with respect to exchange they are called fermions, and they always have half-integer spin.

The wavefunction $\Psi$ for a typical boson pair, with one boson in state $a$ and one in state $b$, labeled 1 or 2, will satisfy

$$\Psi_{boson}(1,2) = \frac{1}{\sqrt{2}}[\psi_a(1)\psi_b(2) + \psi_a(2)\psi_b(1)], \tag{1.2}$$

where $\psi$ denotes the wavefunction of an individual particle.

The corresponding wavefunction for fermions is

$$\Psi_{fermion}(1,2) = \frac{1}{\sqrt{2}}[\psi_a(1)\psi_b(2) - \psi_a(2)\psi_b(1)]. \tag{1.3}$$

If the particles are forced into the same state, (1.2) and (1.3) show one of the most important results in quantum mechanics:

$$\Psi_{boson}(1,2) = \sqrt{2}[\psi_a(1)\psi_a(2)], \tag{1.4}$$
$$\Psi_{fermion}(1,2) = 0. \tag{1.5}$$

Bosons can occupy the same state, but the probability of two fermions occupying the same state is zero. This is the famous Pauli Exclusion Principle [2], which leads to bosons and fermions obeying different quantum statistics when the competition for states increases.

Bosons obey Bose-Einstein statistics [3, 4, 5], and can be described by the Bose-Einstein distribution function

$$n_{BE}(\epsilon) = \frac{g(\epsilon)}{\exp[(\epsilon - \mu)/k_B T] - 1}. \tag{1.6}$$

Meanwhile, fermions are described by Fermi-Dirac Statistics [6, 7], and the Fermi-Dirac distribution function

$$n_{FD}(\epsilon) = \frac{g(\epsilon)}{\exp[(\epsilon - \mu)/k_B T] + 1}. \tag{1.7}$$

At high temperatures these both tend to the Maxwell-Boltzmann distribution and the number of particles per state remains much less than unity. However, as the temperature is decreased, the chemical potential approaches the value of the lowest energy state, and the occupation approaches unity.

As this point is approached (for typical experiments with atomic gases this is at $T < 1\mu$K), the gases become quantum degenerate gases with properties very different to "normal" gases: Bose-Einstein condensates (BECs) for bosons, Degenerate Fermi gases (DFGs) for fermions.

Quantum degenerate effects occur when the thermal de Broglie wavelength $\lambda_{dB}$ of the particles of mass $m$ ($h$ is the Planck constant) becomes comparable to their separation $d$ and the wavepackets associated with the particles begin to overlap, where

$$\lambda_{dB} = h/\sqrt{2\pi m k_B T}. \tag{1.8}$$

This statement is equivalent to saying that the phase-space density of the particles $\rho \lambda_{dB}^3$ is greater than approximately unity, where $\rho$ is the number density.

At this point, the bosons in the system rapidly accumulate in the same state, and thus the sample begins to exhibit a collective behaviour. The BEC is now described by a giant matterwave and behaves like a bosonic superfluid. The relationship between a BEC and a classical gas can be thought of as similar to that between a laser and a light bulb [8].

As fermions cannot occupy the same state, at low temperature they form the so-called Fermi sea with one particle per state and the states filled sequentially from the lowest up (see Figure 1.1). The most energetic particle's energy is called the Fermi energy, which can be associated with a Fermi temperature $T_F$. For quantum degeneracy, one requires $T << T_F$.

BECs and DFGs were first hypothesized in the 1920s, but in atomic gases BECs were not experimentally realized until 1995 [9, 10, 11] and the first DFG was only achieved in 1999 [12], although there were previously indications that BEC was present in liquid Helium [13, 14]. However, the extraordinary properties of the quantum degenerate system are not so clear in these superfluids, due to the strong inter-particle interactions. The ultracold atomic samples of the last 16 years are
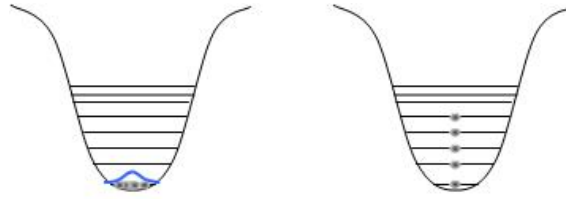
**Figure 1.1:** *At low temperatures, bosons congregate in one energy level and can be described by a single "matterwave", whilst fermions form a "Fermi sea".*

one of the hottest topics in physics today; providing highly controllable quantum systems. They are proving to be of considerable interest to the condensed matter community, amongst others.

In the remainder of this chapter, I will review some of the topical areas of investigation using ultracold atoms, before introducing the theory of the creation of ultracold gases and motivating theoretical descriptions of trapped quantum degenerate atoms which will be used in later chapters of this thesis. I will then discuss the evolution of alternative techniques to produce and manipulate these ultracold atoms, as motivation for the work contained in the remainder of the thesis on the development of alternative techniques to trap cold atoms in a compact but highly flexible apparatus.

## 1.2  Key Experiments with Ultracold Atoms

One of the most unique aspects of experiments with ultracold atoms is the unparalleled control one has in tuning the system. The first example of this control is over the interactions of the atoms in the gas.

The energy levels of two freely colliding atoms and of a molecular bound state have differing magnetic moments, so can be tuned relative to each other by application of an external magnetic field. A Feshbach resonance exists where these two energy levels are equal. By sweeping the magnetic field through the Feshbach resonance, the interactions between the atoms in the sample can be tuned from attractive to repulsive, as characterized by the $s$-wave scattering length $a_s$, which is positive for repulsive interactions and negative for attractive interactions.

In the regime where the magnetic field leaves the energy of the molecular bound state lower than the energy of the colliding atoms, it is favourable for the atoms to form molecules. For homonuclear systems of fermions the regime where the applied magnetic field values give these effects is called the BEC side of the Feshbach resonance. On the other side of the resonance, fermionic atoms pair loosely in momentum space [15, 16]. Although these pairs are unstable in isolation they can exist when surrounded by alike pairs [17]. The system on this side of the resonance is governed by BCS theory, and is known as the BCS side of the resonance, due to the similarity to Cooper pairs in superfluids and in superconductors.

Ultracold atoms on either side of a Feshbach resonance exhibit superfluid behaviour, which has been shown in a number of ways: the observation of no heating

of a BEC below a certain critical velocity (c.f. no disturbance to the flow of the superfluid by an obstacle) [18]; demonstrations of vortex arrays (signifying irrotational flow) [19, 20, 21]; and persistent flow of a rotating toroidal BEC [22, 23]. These cold atomic and molecular systems are seen as a step forward in studying superfluidity (and the related field of superconductivity), as other interactions common to condensed matter systems, e.g. van der Waals interactions in liquid helium, are much reduced. This, added to the high degree of control over atoms available due to their sensitivity to electric and magnetic fields, means they are an ideal system for studying superfluidity in the hope of gaining greater insight into the phenomenon. In particular, quantum degenerate Fermi gases with their Cooper pairs bear a close resemblance to superconductors, and have raised hopes for an explanation for high temperature superconductivity.

Another bridge between ultracold atoms and condensed matter physics has been demonstrated using periodic arrays of optical traps known as optical lattices [24]. These optical lattices, generated by interference of multiple laser beams, are now one of the most commonly-used techniques in ultracold atomic physics, as they allow experimenters to create near-perfect arrays and are well described by the Hubbard Hamiltonian, which is used to describe the electron gas in metallic systems as well as cold atoms in optical lattices:

$$\hat{H} = -J \sum_{\langle i,j \rangle, \sigma} \hat{c}_{i,\sigma}^{+} \hat{c}_{j,\sigma} + U \sum_{i} \hat{n}_{i\uparrow} \hat{n}_{i\downarrow} - \sum_{i,\sigma} \left( \mu - \epsilon_{i,\sigma} \right) \hat{n}_{i,\sigma}. \tag{1.9}$$

The three terms of this Hamiltonian describe: the energy $J$ for an atom to move from one site to the neighbouring one; the interaction energy $U$ required for double-occupancy of a lattice site; and a spatially varying correction $\epsilon_{i,\sigma}$ of the chemical potential $\mu$ which is caused by the spatial variation of the Gaussian laser beams which form a standard optical lattice and any other underlying confinement. $J$ is controlled by the intensity of the trapping light, while $U$ can be varied using Feshbach resonances. The third term of the Hamiltonian tends to cause annoyance to theorists as it can be responsible for "washing out" many interesting physical effects, so is frequently ignored in analysis (see, e.g., [25]).

By varying $J$ a BEC in a lattice can be varied from a superfluid state where the atoms flow freely from site to site (high $J$) to a Mott insulator state [26] with uniform number occupancy across the lattice sites. This is a manifestation of Heisenberg's uncertainty principle described by the relation

$$\Delta N \cdot \Delta \phi \approx const, \tag{1.10}$$

where $\Delta \phi$ denotes the uncertainty in phase, and $\Delta N$ the uncertainty in atom number per site. In the superfluid state all the atoms are exactly in phase, whilst in the Mott insulating state the phase-correlation is completely lost in favour of number-correlation. By reversing the ramp of well depth, the phase correlation can be recovered completely.

The three-dimensional Hubbard model for fermions has proved impossible to solve, either analytically or numerically, but is believed to contain much of the vital physics for explaining phenomena such as the poorly understood high-$T_c$ superconductivity [27]. This has provoked much interest in using cold atoms as a

Hubbard model quantum simulator, which can unveil the mysteries of these phenomena. Considerable effort within the field is currently being spent on building on the observation of the Mott Insulator transition in fermions [28, 29] in the hope of observing antiferromagnetic ordering [30] and $d$-wave superfluidity [31, 32].

Further experiments demonstrating condensed matter physics with ultracold atoms in optical lattices investigated Anderson localization and the disorder-induced superfluid-insulator transition [33, 34, 35], while there are proposals for observing the integer or fractional quantum Hall effects [36] (the quantization of the Hall conductivity to integer or rational multiples of $\frac{e^2}{\hbar}$) and the quantum spin Hall effect [37] in optical lattices.

In the absence of a general quantum computer (the creation of which is also being investigated within the field [38, 39, 40, 41]), ultracold atoms are currently seen as the prime candidate for modelling more complicated systems due to their sensitivity to electric and magnetic fields demonstrated by the Feshbach resonance and optical lattice experiments.

## 1.3 Laser Cooling

The first atomic BECs were produced from a room-temperature alkali metal vapour, using a two stage approach: an initial trapping and cooling phase in a Magneto-Optical trap (MOT), followed by a second phase of evaporative cooling in a purely magnetic trap [9, 10, 11].

Thorough descriptions of the physics of MOTs are included elsewhere, e.g. in [42, 43], so only a brief summary is included here. An atom moving in the -$z$-direction illuminated by a counter-propagating laser beam can absorb a resonant photon travelling in the $z$-direction with energy close to one of the atomic transitions: conservation of momentum dictates that the atom's momentum must decrease. The atom then emits the photon in a random direction and receives a push opposite to this. Over many absorption-spontaneous emission pairs, the isotropic nature of the emission cancels the effects of this force, and thus the net force opposes the atomic motion [44, 45, 46].

If two counter-propagating and overlapped laser beams of angular frequency $\omega$ (slightly below the resonant value $\omega_0$) are incident on the atom, the Doppler effect causes the frequency of the laser beam travelling against the motion of the atom to be closer to resonance, thus more photons from this beam will be absorbed. This generates a force opposed to the atom's motion, like that in a viscous material. The 3D extension of this (adding two more pairs of beams such that all three pairs are mutually orthogonal) is known as optical molasses [47].

Due to the optical Earnshaw Theorem, which states that there are no global minima in potential due to radiation forces only [48], this setup is not sufficient to trap atoms. The addition of a linear magnetic field gradient [49] across one of the axes of the beams and the use of circularly polarized beams allows the Zeeman effect to provide the required minima, whilst at the same time introducing a positional dependence to the force on the atom. The combination of these ideas produces a MOT.
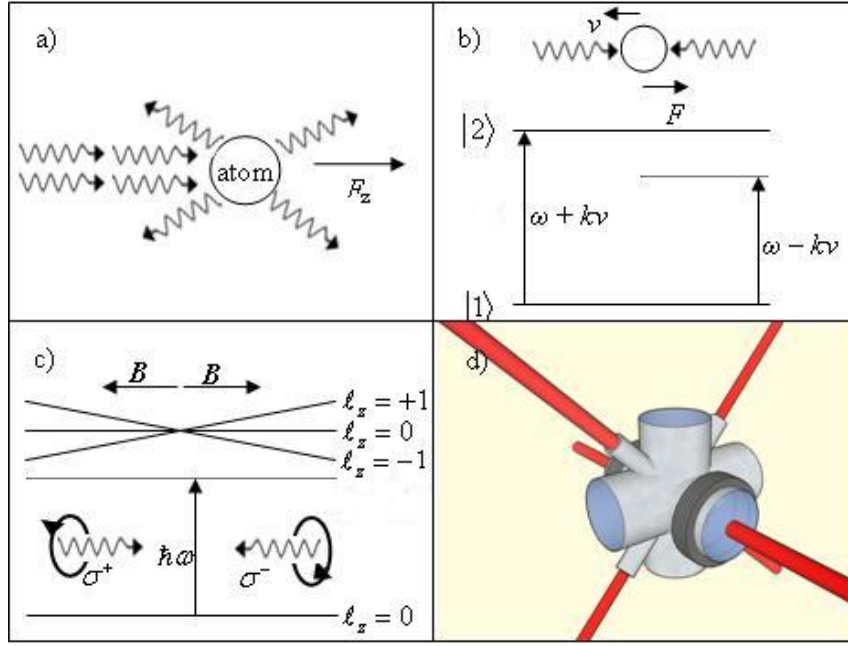
**Figure 1.2:** *Simple laser cooling ideas. (a) Transfer of momentum from radiation to atoms. (b) Preferential absorption of counter-propagating photons due to the Doppler effect. (c) The Zeeman effect introduces a spatial dependence to the photon-scattering force, which allows trapping of atoms. (d) The combined effects are known as a Magneto-Optical Trap.*

The combination of laser cooling and magnetic field gradients allows one to slow and trap atoms, which can be viewed as reducing their temperature, as

$$\frac{1}{2}mv^2 = \frac{1}{2}k_B T, \tag{1.11}$$

if one assumes that the photons supply a thermal bath.

A convenient way to understand the cooling is to consider the energy transfer involved in each absorption / spontaneous emission process. An atom absorbs a photon of energy $\hbar\omega$ which is less than $\hbar\omega_0$, the energy of the emitted photon. Therefore in each process, the atom gives up energy $\hbar(\omega - \omega_0)$ to the photons.

Atoms trapped in this way can only reach a certain minimum temperature [50]. Semi-classical theory (treating the atom as a quantum entity but the light as a classical entity) gives the limit of this cooling as the Doppler limit:

$$T_{Doppler} = \frac{\hbar\Gamma}{2k_B}, \tag{1.12}$$

where $\Gamma$ is the natural width of the atomic transition. This is typically of order $100\mu$K in the atomic samples discussed here.

When initial experiments with MOTs were conducted, it was discovered that the atoms were actually colder than this [51]. A new theory of sub-Doppler cooling [52] which exploits polarization gradients gave more accurate predictions for the minimum temperature:

$$T_{sub-Doppler} = \frac{0.1\hbar\Omega^2}{k_B |\delta|}, \tag{1.13}$$

where $\Omega$ is the Rabi oscillation frequency and $\delta = \omega - \omega_0$ is the detuning of the laser beams. Theoretically, this cooling phase is only limited by the recoil limit - the temperature variation associated with absorption or emission of a single photon:

$$T_{Recoil} = \frac{\hbar^2 k^2}{mk_B}. \tag{1.14}$$

The sub-Doppler cooling is optimized in experiment by initial cooling in a MOT before an optical molasses phase (no magnetic field) at large detunings, allowing the sub-Doppler mechanisms to further cool the cloud.

This minimum temperature (typically around $10\mu$K) is obtained at low number densities limited by Coulomb-like interactions due to photon re-emission [53], and despite some advances [54, 55, 56, 57], MOTs are unable to achieve the required phase-space densities to enter the quantum degenerate regime. In order to achieve colder, denser atomic gases, a further cooling mechanism is required.

## 1.4 Evaporative Cooling

The second stage of production of ultracold gases, known as evaporative cooling [58], requires the atoms to be transferred to a conservative magnetic or optical trap.

### 1.4.1 Magnetic Traps

Magnetic traps use the state-dependent force on an atom's magnetic dipole moment in an inhomogeneous magnetic field. These conservative traps have typical depths of the order of 100mK, and offer smooth trap geometries. They are, however, restricted to specific internal states of atoms, and possible trapping geometries are restricted by the arrangement of coils of wire or permanent magnets. This latter problem has been overcome using so-called atom chips (see Section 1.6), but at the expense of increased roughness in the trapping potential.

The energy of atoms in a magnetic field is governed by the Zeeman effect and given by the component of the atomic magnetic dipole moment $\vec{\mu}$ aligned to the magnetic field $\vec{B}$, i.e. $U = -\vec{\mu} \cdot \vec{B}$. When the magnetic moment of the atoms is aligned to the magnetic field, the atoms are attracted to areas of large magnetic field (so-called high-field seekers). Low-field seekers are atoms where the magnetic moment is anti-aligned to the magnetic field.

As the Maxwell equations in free space do not allow for local maxima of d.c. magnetic fields, in most experiments only low-field seekers are magnetically trapped. The simplest magnetic trap is generated in the centre of a pair of anti-Helmholtz coils (identical coils of radius $r$ separated by $\sqrt{3}r$ with current flowing in opposite directions). As the magnetic field is approximately linear up to the positions of the coils, the anti-Helmholtz condition can normally be relaxed in practice. The

quadrupole magnetic field ($\vec{B} = B'(x, y, -2z)$) generated by the pair gives a constant gradient along both the coil axis and the plane parallel to the coils, and zero magnetic-field at the centre point between the coils.

The zero of magnetic field gives a degeneracy of trapped and anti-trapped states, allowing adiabatic Majorana spin flips from one state to another to occur. There are numerous ways to overcome this problem, including time-averaged magnetic fields [59], Ioffe-Pritchard traps with non-zero bottom [60] and optically plugged quadrupole traps [11].

## 1.4.2 Optical Dipole Traps

Optical trapping techniques in cold atoms have a rich history. A conservative trapping potential for ultracold atoms can be generated with focused laser light far-detuned from an atomic transition. The light interacts with the atom to induce a dipole and create a force via the A.C. Stark effect. Under appropriate conditions the optical dipole force can be modeled classically. An electric field $\vec{E}$ which is incident upon an atom induces an atomic dipole moment

$$\vec{p} = \alpha \vec{E}, \tag{1.15}$$

where $\alpha$ is the complex polarizability.

The interaction potential of the induced dipole moment $\vec{p}$ in a driving field

$$\vec{E}(\vec{r}, t) = \hat{e} E(\vec{r}) \exp(-i\omega t) + c.c., \tag{1.16}$$

(where $\hat{e}$ denotes the polarization of the light and $E$ is the electric field amplitude) is given by

$$U_{dip} = -\frac{1}{2} \left\langle \vec{p} \cdot \vec{E} \right\rangle = -\frac{1}{2\epsilon_0 c} \mathrm{Re}(\alpha) I, \tag{1.17}$$

where the factor $1/2$ is required because the dipole moment is induced rather than permanent, and the angular brackets denote time averages, while the field intensity $I$ is given by

$$I = 2\epsilon_0 c |E|^2. \tag{1.18}$$

The Lorentz model of a classical oscillator considers an atom to consist of an elastically-bound ion core and electron with an oscillator eigenfrequency $\omega_0$ at the optical transition frequency, and can be used to find the polarizability. Damping of the oscillator occurs due to radiative energy loss from the accelerating electron, and takes the form

$$\Gamma_\omega = \frac{e^2 \omega^2}{6\pi \epsilon_0 m_e c^3}, \tag{1.19}$$

where we define the resonant damping rate

$$\Gamma = \Gamma_{\omega_0} = \left(\frac{\omega_0}{\omega}\right)^2 \Gamma_\omega. \tag{1.20}$$

For the alkali atoms of interest in ultracold atom experiments in a low-saturation regime (guaranteed in far off-resonant light fields), this calculated decay rate agrees with the actual value to within a few percent [61]. A semi-classical approach can be found in, e.g., [42].

The equation of motion for the electron oscillation is

$$\ddot{x} + \Gamma_\omega \dot{x} + \omega_0^2 x = -\frac{eE}{m}. \tag{1.21}$$

Substituting $\vec{p} = -e\vec{x}$ and (1.15) and (1.16) into (1.21) allows us to find the polarizability by solving for terms involving $\exp(-i\omega t)$

$$\alpha = \frac{e^2}{m} \frac{1}{\omega_0^2 - \omega^2 - i\omega\Gamma_\omega}. \tag{1.22}$$

Substitution of (1.19) therefore gives

$$\alpha = 6\pi\epsilon_0 c^3 \frac{\Gamma/\omega_0^2}{\omega_0^2 - \omega^2 - i\left(\omega^3/\omega_0^2\right)\Gamma}. \tag{1.23}$$

Combining (1.17) and (1.23) leads to the result

$$U_{dip}\left(\vec{r}\right) = -\frac{3\pi c^2}{2\omega_0^3}\left(\frac{\Gamma}{\omega_0 - \omega} + \frac{\Gamma}{\omega_0 + \omega}\right)I\left(\vec{r}\right). \tag{1.24}$$

In experiments, the laser detuning is small compared to the resonant frequency, so using the rotating wave approximation we can neglect the second term in (1.24) to give

$$U_{dip}\left(\vec{r}\right) = \frac{3\pi c^2}{2\omega_0^3}\frac{\Gamma}{\delta}I\left(\vec{r}\right), \tag{1.25}$$

where $\delta$ is the laser detuning. The force exerted on the atoms by the light is therefore a conservative force given by

$$F_{dip}\left(\vec{r}\right) = -\nabla U_{dip}\left(\vec{r}\right) = -\frac{3\pi c^2}{2\omega_0^3}\frac{\Gamma}{\delta}\nabla I\left(\vec{r}\right). \tag{1.26}$$

This equation contains the essential physics of dipole trapping of atoms using far-off-resonant laser light: for blue-detuned light ($\delta > 0$) the atoms are repelled from the regions of high intensity, while for red-detuned light ($\delta < 0$) the atoms are attracted to the regions of maximum intensity.

Optical dipole traps are typically shallower than either magnetic or radiation-pressure traps, with typical trap depths in the mK range. The optical excitation is kept extremely low, so that the traps are not limited by the light-induced mechanisms present in radiation-pressure traps and are independent of the particular sub-level of the electronic ground state.

### 1.4.3   Evaporative cooling

Magnetic or far-detuned optical traps remove the limitation of single photon scattering but do not directly increase the phase-space density of the atomic sample, meaning an evaporative cooling stage is required. For magnetic traps a radio-frequency source is used to excite the most energetic atoms and spin-flip them, repelling them from the trap region. In optical dipole traps, in which confinement is not spin-state dependent, the hottest atoms are removed by lowering the depth of the potential - i.e. by decreasing the intensity of the laser beams creating the trap. By removing the hottest atoms, a disproportionately large temperature reduction is achieved across the whole sample once the atoms rethermalize by collisions. Collisions in evaporative cooling come in two families: "good" two-body $s$-wave elastic collisions and "bad" inelastic two- and three-body collisions which remove more atoms from the traps. The rate of elastic collisions must dominate the inelastic losses for evaporative cooling to proceed efficiently.

The removal - rethermalization process is iterated until quantum degeneracy is reached. In magnetic traps, if the density of the atoms increases as the temperature is reduced, the evaporation enters a "runaway" regime which is very efficient. In simple optical traps, as the trapping frequency is also reduced when the trap depth is reduced, runaway evaporation is not possible.

To efficiently evaporatively cool fermions, for which $s$-wave collisions are forbidden by the Pauli principle, one must cool sympathetically with a distinguishable atomic ensemble, either another fermionic ensemble [12] or a bosonic ensemble [62].

## 1.5   BEC Theory

### 1.5.1   Ideal Bose Gas in a Power-law Potential

If an ideal Bose gas is confined in a power-law trap given by a potential $U$ of the form

$$U\left(r\right) = A\left(\frac{r}{r_0}\right)^\alpha,  \tag{1.27}$$

where $A$ characterises the trap depth , $r_0$ the size and $\alpha$ the order, then the density of states is given by [63]

$$g_{BE}\left(\epsilon\right) = C_\alpha \epsilon^{\frac{1}{2}+\frac{3}{\alpha}},  \tag{1.28}$$

with $C_\alpha$ a constant which depends on the power-law. The number of atoms in the excited states $N_{ex}$ of the Bose gas is

$$N_{ex} = \int_0^\infty \frac{\mathrm{d}\epsilon\, g_{BE}\left(\epsilon\right)}{\exp[\frac{(\epsilon-\mu)}{k_B T}] - 1},  \tag{1.29}$$

and the total number of atoms $N = N_{ex} + N_0$, where $N_0$ is the number of Bose condensed atoms ($N_0 = 0$ at and above the transition temperature the Bose-Einstein Condensation critical temperature $T_{BE}$, at which point $\mu = 0$). In calculating $N_{ex}$ we use the substitutions

$$x = \frac{\epsilon}{k_B T}, \tag{1.30}$$

and

$$z = \exp\left[\frac{\mu}{k_B T}\right]. \tag{1.31}$$

($z$ is known as the fugacity) with the standard integral

$$\int_0^\infty \frac{\mathrm{d}x\, x^{\kappa-1}}{(z \exp(x) - 1)} = \Gamma(\kappa) g_\kappa(z). \tag{1.32}$$

$\Gamma(\kappa)$ is the gamma function and

$$g_\kappa(z) = \sum_{j=1}^\infty z^j j^{-\kappa}, \tag{1.33}$$

is the Polylogarithmic function. We find the number of atoms above the critical temperature to be

$$
\begin{aligned}
N = N_{ex} &= C_\alpha \left(k_B T\right)^{(3/2+3/\alpha)} \int_0^\infty \mathrm{d}x \frac{x^{1/2+3/\alpha}}{z^{-1} \exp(x) - 1}, \tag{1.34}\\
&= C_\alpha \left(k_B T\right)^{(3/2+3/\alpha)} \Gamma\left(3/2 + 3/\alpha\right) g_{\frac{3}{2}+\frac{3}{\alpha}}(z), \tag{1.35}
\end{aligned}
$$

The critical temperature can be found by simply rearranging (1.35):

$$k_B T_{BE} = \left[\frac{N}{C_\alpha \Gamma\left(3/2 + 3/\alpha\right) g_{\frac{3}{2}+\frac{3}{\alpha}}(1)}\right]^{\frac{1}{\frac{3}{2}+\frac{3}{\alpha}}} \tag{1.36}$$

Below $T_{BE}$, $\mu = 0$ and therefore $z = 1$. By solving (1.35) simultaneously at and above $T_{BE}$, we find

$$g_{\frac{3}{2}+\frac{3}{\alpha}}(z) = g_{\frac{3}{2}+\frac{3}{\alpha}}(1) \left(\frac{T_{BE}}{T}\right)^{\frac{3}{2}+\frac{3}{\alpha}}, \tag{1.37}$$

which allows one to calculate $z$ numerically above $T_{BE}$. The fraction of atoms occupying the ground state below $T_{BE}$ is found from (1.35) to be

$$\frac{N_{BEC}}{N} = 1 - \frac{N_{ex}}{N} = 1 - \left(\frac{T}{T_{BE}}\right)^{\frac{3}{2}+\frac{3}{\alpha}}. \tag{1.38}$$

The internal energy of the Bose gas

$$E = \int_0^\infty \frac{\mathrm{d}\epsilon\, \epsilon g_{BE}(\epsilon)}{\exp\left[\frac{(\epsilon-\mu)}{k_B T}\right] - 1}, \tag{1.39}$$

is thus

$$\frac{E}{Nk_B} = 3T\left(\frac{1}{2} + \frac{1}{\alpha}\right)\begin{cases}\frac{g_{\frac{5}{2}+\frac{3}{\alpha}}(z)}{g_{\frac{3}{2}+\frac{3}{\alpha}}(z)}, & T \geq T_{BE}, \\ \frac{g_{\frac{5}{2}+\frac{3}{\alpha}}(1)}{g_{\frac{3}{2}+\frac{3}{\alpha}}(1)}\left(\frac{T}{T_{BE}}\right)^{\frac{3}{2}+\frac{3}{\alpha}}, & T \leq T_{BE},\end{cases} \tag{1.40}$$

while the entropy $S$ is given by

$$\frac{dS}{dT} = \frac{1}{T}\frac{dE}{dT}, \tag{1.41}$$

as

$$\frac{S}{Nk_B} = \begin{cases}\left(\frac{5}{2} + \frac{3}{\alpha}\right)\frac{g_{\frac{5}{2}+\frac{3}{\alpha}}(z)}{g_{\frac{3}{2}+\frac{3}{\alpha}}(z)} - \ln(z), & T \geq T_{BE}, \\ \left(\frac{5}{2} + \frac{3}{\alpha}\right)\frac{g_{\frac{5}{2}+\frac{3}{\alpha}}(1)}{g_{\frac{3}{2}+\frac{3}{\alpha}}(1)}\left(\frac{T}{T_{BE}}\right)^{\frac{3}{2}+\frac{3}{\alpha}}, & T \leq T_{BE}.\end{cases} \tag{1.42}$$

We will use the equations derived above to propose a new method for the production of BECs in Section 4.14.

## 1.5.2   The Weakly-Interacting Bose Gas

A weakly-interacting Bose gas at $T << T_{BE}$ is accurately described by a mean-field variant of the Schrödinger equation known as the Gross-Pitaevskii equation. In second quantization notation, the Hamiltonian for a system of interacting particles is

$$\hat{H} = \int d^3 r \hat{\Psi}^\dagger(\vec{r})\left[-\frac{\hbar^2}{2m}\nabla^2 + U_{ext}(\vec{r}) + \frac{1}{2}\hat{\Psi}^\dagger\left(\vec{r'}\right)U_{int}\left(\vec{r} - \vec{r'}\right)\hat{\Psi}\left(\vec{r'}\right)\right]\hat{\Psi}(\vec{r}), \tag{1.43}$$

where $\hat{\Psi}^\dagger(\vec{r})$ and $\hat{\Psi}(\vec{r})$ are the bosonic field creation and annihilation operators and

$$U_{int}\left(\vec{r} - \vec{r'}\right) = \frac{4\pi\hbar^2 a_s}{m}\delta\left(\vec{r} - \vec{r'}\right), \tag{1.44}$$

is the two-body interatomic potential in a dilute, low-temperature gas for which one needs only consider binary s-wave collisions as characterized by the s-wave scattering length $a_s$ and $\delta\left(\vec{r} - \vec{r'}\right)$ is the Dirac delta function.

Time evolution of the bosonic field can be found via the Heisenberg equation

$$i\hbar\frac{\partial\hat{\Psi}(\vec{r},t)}{\partial t} = \left[\hat{\Psi}(\vec{r},t), \hat{H}\right]. \tag{1.45}$$

For macroscopic occupation of the ground state, one can apply the Bogoliubov approximation to decompose the field into the condensate wavefunction $\Phi(\vec{r},t) = \left\langle\hat{\Psi}(\vec{r},t)\right\rangle$ and a perturbation field $\delta(\vec{r},t)$ encompassing all other modes:

$$\hat{\Psi}(\vec{r},t) = \Phi(\vec{r},t) + \hat{\delta}(\vec{r},t), \tag{1.46}$$

The density $\rho(\vec{r},t)$ of the BEC is now given by $|\Phi(\vec{r},t)|^2$. In the limit $T \to 0$, $\hat{\delta}(\vec{r},t) \to 0$. Thus (1.45) becomes:

$$i\hbar \frac{\partial \hat{\Phi}(\vec{r}, t)}{\partial t} = \left[ -\frac{\hbar^2}{2m} \nabla^2 + U(\vec{r}) + \frac{4\pi\hbar^2 a_s}{m} N_0 |\Phi(\vec{r}, t)|^2 \right] \Phi(\vec{r}, t). \qquad (1.47)$$

The time-independent Gross-Pitaevskii equation can be obtained by assuming the BEC wavefunction has the form $\Phi(\vec{r}, t) = \Phi_0(\vec{r}) \exp(i\mu t/\hbar)$, giving

$$\left[ -\frac{\hbar^2}{2m} \nabla^2 + U(\vec{r}) + \frac{4\pi\hbar^2 a_s}{m} N_0 |\Phi_0(\vec{r})|^2 \right] \Phi_0(\vec{r}) = \mu \Phi_0(\vec{r}). \qquad (1.48)$$

The Thomas-Fermi approximation assumes that the kinetic energy of the BEC is much smaller than interaction or potential energies, which is the case for harmonically trapped BECs. The density of the interacting gas is then parabolic:

$$N_0 |\Phi_0(\vec{r})|^2 = \frac{m\mu}{4\pi\hbar^2 a_s} \left( 1 - \frac{x^2}{R_{TFx}^2} - \frac{y^2}{R_{TFy}^2} - \frac{z^2}{R_{TFz}^2} \right), \qquad (1.49)$$

where $R_{TFi}$ is the Thomas-Fermi radius, which is defined as the point at which $\mu = U(R_{TF})$, giving

$$R_{TFi} = \sqrt{\frac{2\mu}{m\omega_i^2}}, \qquad (1.50)$$

for a harmonic trap.

The normalization condition $\int |\Phi_0(\vec{r})|^2 \, d\vec{r} = 1$ allows one to calculate the chemical potential of the gas. Further details on the derivation here can be found in [64]. We will use this method to calculate the chemical potential of a Bose gas in a ring trap in Section 4.15.

## 1.6  Alternative Methods to Produce Cold Atoms

Evaporative cooling is necessarily a "lossy" process, so in order to counteract the effect of these losses, one looks to maximise the number of atoms trapped in the MOT. To do this a sensible strategy would seem to be to increase the density of atoms within the cell.

However, not all of the atoms emitted by the atom source are captured by the MOT. Atoms with velocities higher than the MOT capture velocity $v_c$ are not trapped, nor are atoms which do not pass through the beam intersection. In addition, regardless of how carefully one prepares one's system there will always be excess background debris. Any collision between background atoms and trapped atoms will remove atoms from the MOT or the magnetic or optical dipole trap. The only way to minimise this loss is to seek lower densities in the vacuum chamber.

This leaves us in the rather frustrating position of having two constraints on our system that seem to directly oppose each other. Clearly, optimised evaporative cooling requires a compromise solution.

The first BECs were achieved by loading the MOT in one of two ways: atoms were collected from a hot gas in a vapour cell [65]; or they were loaded into the

MOT from a pre-cooled atom source. The atoms can be pre-cooled using a number of different techniques: a Zeeman slower [66]; a Stark slower [67]; a diffuse slowing source [68]; a broadband slowing source [69]; or chirped frequency slower [70].

The disadvantage of simple vapour cells is that there are a high proportion of hotter atoms in the chamber, thus increasing the background pressure in the cell and reducing coherence times for ultracold gases. The other methods are all designed to overcome the problem of varying Doppler shift as an atomic beam is slowed, but add bulk to the apparatus.

The standard method to improve the simple vapour cell setup without a bulky slower is to add a second chamber connected by a thin tube [71], so that the new cell can be held at a lower pressure than the first. A MOT is loaded in the high pressure cell, before being transferred to the second cell using a "push" laser beam, acceleration due to gravity or a moving magnetic trap. This, again, involves increasing the overall size of the apparatus compared to a single-cell setup.

Another possible implementation within a single chamber uses magnetic microtrap geometries, which can be created within a few microns of "atom-chips" comprising current-carrying wires or permanent magnets, giving much tighter and higher spatially resolved traps than possible using macroscopic magnetic traps [72].

The use of atom chips greatly simplifies the apparatus required to produce ultracold atoms, needing relatively little current ($< 10A$) to create large magnetic-field gradients and tightly-confining magnetic traps. The tight traps give a high collision rate, meaning evaporative cooling proceeds very quickly and therefore the requirements of low background pressure are somewhat relaxed, allowing compact vacuum apparatus.

MOTs have been demonstrated using the chip wires to create the requisite magnetic field gradient and the surface of the chip to reflect at least one of the MOT beams [73]. This tends to suffer from limited optical access, but work to incorporate the MOT phase using a single laser beam and diffractive surfaces above an atom-chip is ongoing [74]. Absorption imaging of the atoms has also been demonstrated [75], meaning cooling, manipulation and imaging can all take place on a single atom-chip. One drawback to atom chips is that they suffer from effects of fluctuating surface currents due to defects introducing noise into the trap potential, which has been seen to fragment the atom cloud [76].

The replacement of the standard atom-oven as a source (a heated section of the vacuum chamber containing a solid sample of the species of interest) by a thermal dispenser or getter [77] can cut down on the size of the apparatus. These strips of metal typically contain an alkali salt and a chemical reaction is activated by heating the strip, usually by passing a current through them. It has been shown that pulsing the current on and off can efficiently load a MOT whilst keeping the background pressure low [78]. Griffin, *et al.* also showed that these dispensers can be activated using a high power laser source to heat the dispenser, and this has an advantage of faster switch-off compared to the method of heating via current, as the heating can be restricted to a small area of the dispenser [79]. This means that the background pressure can fall more quickly for light-activated dispensers as opposed to the current driven case. However, in [79] the authors note that advantage of instantaneous cessation of emission of atoms is lost if one seeks to maximise the

number of atoms in the MOT.

Another type of dispenser for alkali atoms has been proposed: the light-controlled atom dispenser or LICAD [80]. This dispenser would not require high-powered laser light to emit atoms, but rather uses a non-thermal effect known as Light-Induced Atomic Desorption (LIAD). These dispensers are not yet commercially produced, but the LIAD effect can be used to enhance low pressure MOT loading, by temporarily increasing the atom vapour density. The disadvantage of using LIAD is that it requires ultra-violet light sources, which can be expensive at low wavelengths, and obviously introduce a health hazard.

In the early 1990s, it was discovered that Na atoms could be removed from certain organic coatings when illuminated with weak, non-resonant radiation [81]. In fact, the effect was even noted when the cell containing the atoms and the coating was illuminated by an ordinary lamp. This LIAD effect was investigated initially using polydimethylsiloxane (PDMS) [82] coatings and has since been demonstrated in other organic coatings [83, 84, 85]. This line of research has lead to the proposition of a specific model for the behaviour as a combined effect of atoms desorbing from the surface of the coating and of enhanced diffusion within the bulk of the coating [86]. Adding a coating to an ultra-high vacuum cell increases the possibility of contamination of the vacuum and is therefore not appealing for ultracold atom experiments, but LIAD has also been demonstrated from porous glass [87] with equal efficiency to the organic coatings, as well as from uncoated glass [88] and from stainless steel [89, 90].

The LIAD effect has been found to be dependent on a number of parameters. The number of atoms released from the surface (or coatings) has been found to depend on the square-root of the light intensity [89], the temperature of the cell [91], the ratio of surface area to volume (explaining the higher efficiency of porous glass compared to "normal" glass) [84] and on the frequency of the incoming light [90]. There is a threshold wavelength above which no LIAD is observed, which varies from experiment to experiment. Generally however, no LIAD effect is produced with infrared or red light, and the number of atoms released increases with the frequency of the light. This has drawn analogy between LIAD and the photoelectric effect. Despite the extensive analysis that has taken place to produce the trends detailed above, no definitive theory of the LIAD effect has been developed. LIAD has been used to load MOTs [89, 90], and was used to aid the production of BECs on an atom chip [88].

While the LIAD and dispenser techniques can be used to improve the MOT loading and the conditions for evaporative cooling, there are also a number of interesting alternative methods for evaporative cooling. To allow runaway evaporative cooling, the authors of [92] created their optical dipole trap using a lens on a translation stage. The position of the lens is dynamically varied to tighten the focus (trap frequency) during the evaporative cooling process, which improves the efficiency of the evaporation. Clément, *et al* demonstrated an efficient all-optical technique relying on a repellent laser beam on top of a conservative trap [93] which decouples trap frequency from trap depth, which is a barrier to runaway evaporation in optical traps. By using a weak quadrupole magnetic field like the one used in the MOT phase, the density of atoms in an optical dipole trap can be increased to enhance

the collision rate in evaporative cooling [94], while two-stage evaporations in first a magnetic then an optical trap have also been demonstrated [95]. Adiabatic and reversible crossings of the BEC transition can also be achieved by superimposing a "dimple" onto an existing trap [96, 97, 98], which can push a cold Bose gas across the BEC transition without the need for further cooling of the gas.

While there are numerous alternative techniques for the production of ultracold gases, we will characterize the pulsed dispensers and the LIAD effect to negate the need for the bulky methods discussed above. We will also use the magnetic field coils used in the MOT as an initial magnetic trap, but would like to supplement this with another highly controllable additional trap to give us a flexible and compact apparatus.

## 1.7 Flexible Traps for Cold Atoms

Attention in recent years within the field of ultracold atoms has been turning to flexible, nontrivial trapping geometries based on both magnetic and optical trapping.

A variety of magnetic trap geometries have been created using atom-chips such as 1D linear traps [99], quadrupole traps using Z- or U-shaped wires [99], X- or Y-shaped beamsplitters [100, 101], atom transport [102] and lattices of microtraps [103]. The flexibility of atom chips may be limited by pre-existing knowledge of the trap geometry of interest and the time taken to lithographically create a new chip should the existing one prove to be unsuitable.

State-dependent traps have also been created using microwave fields [104], while superpositions of rf-oscillating and static magnetic fields have been used to make rf-dressed adiabatic potentials [105]. This type of dressed state trap has also been realized in macroscopic magnetic traps using the Time-Averaged Adiabatic Potential [106]. Another alternative proposal for tailoring magnetic fields on a larger scale is to use inductively-coupled AC conductors [107].

One of the most exciting applications of ultracold atomic physics is the investigation of their behaviour in optical lattices, generated by standing waves of laser light (see Section 1.2). Although these structures allow significant freedom to control quantum degenerate gases, an increased degree of flexibility and dynamism is desirable. In standard optical lattices, as were discussed in Section 1.2, the depth of potential well can be varied by tuning the laser intensity. The separation of these wells, $d$, is given by

$$d = \lambda / \left( 2 \sin \left( \theta / 2 \right) \right), \tag{1.51}$$

where $\lambda$ is the wavelength of the laser beam, and $\theta$ is the angle of beam intersection. Variation of $d$ is thus achieved either by varying the laser wavelength or by varying the angle of intersection of the laser beams, which can be achieved using acousto-optical deflectors. Clearly, the minimum lattice constant is $\lambda/2$, which is typically of the order of 500nm.

To create a more complicated structure, it is possible to overlap additional standing waves: the overlap of three mutually-orthogonal standing waves creates a simple cubic lattice, whilst varying the relative angle of the standing waves can create,

e.g., triangular or Kagome lattices [108].  Superlattice structures can be achieved by superimposing an additional standing wave which is commensurate with the existing standing wave [109], while recent developments include dynamic rotating or expanding optical lattices [110].

One major field of interest is the effects of disordered optical lattices on quantum degenerate gases [33, 34], and quasi-disorder can be achieved by the superposition of two non-commensurate lattices, or by addition of an external magnetic field or a speckled laser beam. Optical lattices which employ Raman transitions have been shown to have a basic lattice period less than standard optical lattices [111].  The addition of a radiofrequency dressing to an optical lattice can also allow engineering of complicated and smaller lattice structures [112].  Patterning of atoms within an optical lattice has also been demonstrated using microwave radiation in a magnetic field gradient [113] and using a focused electron beam to forcibly remove atoms [114].

There are currently two competing alternative technologies to traditional optical lattices under investigation with the aim of producing arbitrary optical trapping potentials: acousto-optic atom traps and holographic atom traps.

Time-averaged trapping structures can be created by scanning a laser-beam at high frequency with an Acousto-Optic Deflector [115, 116, 117]; additional confinement in the direction of beam propagation can be added in the form of a light sheet. This method produces good results, as shown in Figure 1.3, and the only possible limitation of this scheme is scalability: the laser is scanned over the pattern and back to the same location faster than the atoms can propagate away from their trapped location. The transit time must obviously increase with trap pattern complexity, and this may become too long for the atoms not to notice the absence of the laser light.
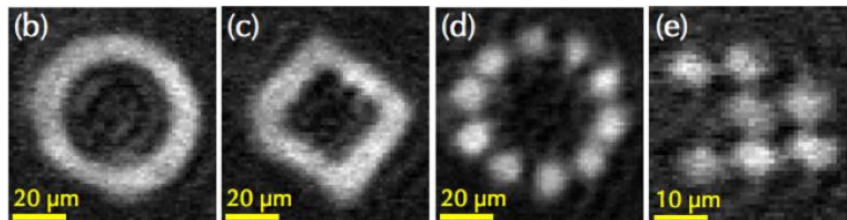


**Figure 1.3:** *Cold atoms in optical traps painted with an Acousto-Optical Deflector [116].*

Classic holography, as can be seen in everyday applications such as security features on credit cards, allows one to create images of absent objects.  The same principles can be used to construct optical wavefronts using interference and diffraction. These techniques have become widely used in colloidal and biological physics [118].

Computer generated holography uses computers to calculate a holographic phase pattern which can be imparted onto a light beam by static, lithographically recorded masks, or a dynamic Diffractive Optical Element (DOE) such as a Spatial Light Modulator (SLM) or a Digital Micromirror Device (DMD).

Using a large Numerical Aperture (NA) aspheric lens to focus light from an SLM, arbitrary light fields can be sculpted in the focal plane of the lens. Once the beam
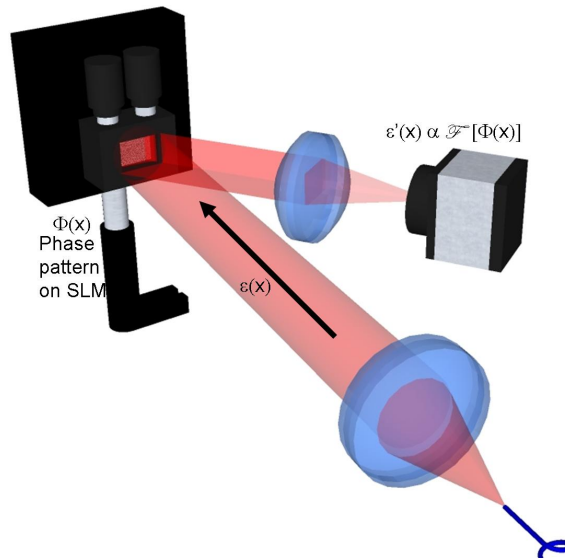
**Figure 1.4:** *A Spatial Light Modulator is illuminated by polarized and collimated laser light, and diffracts the light by imprinting a phase pattern $\Phi(x)$ onto the beam. The phase pattern on the SLM is calculated such that in the far-field (or once the light is focused by a lens), it forms an intensity pattern of interest $\epsilon'(x)$. This can be recorded on a CCD camera, or used to trap cold atoms.*

of light is focussed by a lens, the intensity distribution in the focal plane of the lens corresponds to the Fourier transform of the phase on the SLM, allowing freedom to create arbitrary light patterns. By displaying a sequence of patterns on the SLM, dynamic patterns can also be generated.

The use of holographic optical traps for cold atoms was first proposed in 2003 [119], but their use in cold atoms has been limited to either arrays of dipole potentials or patterns for which the phase is well known, e.g. Laguerre-Gauss beams (Figure 1.5). Applications such as atom interferometers [119] and ring lattices [120] have been proposed, while the manipulation of single atoms [121], clouds of cold atoms from a MOT [122] and a BEC [123] have all been demonstrated.

Using holographic methods to generate an intensity pattern can increase control over the optical traps. One potential application for holographic atom traps is to realise Hubbard-regime lattices in which the inter-site energy difference $\epsilon_i - \epsilon_{i+1}$ can be set to zero for all $i$., which may allow interesting effects to be observed (see Section 1.2). In a holographic optical lattice, variation of the lattice constant is straightforward, plus individual lattice sites are addressable. While increased lattice complexity involves the addition of more laser beams, holographic traps can be generated with a single trapping beam.

By using a dynamic diffractive optical device such as a Spatial Light Modulator one could create the optical dipole trap used for evaporative cooling, perform the evaporative cooling process, and then change the trap shape to that required for the subsequent investigation of the ultracold gas (as demonstrated in Section 4.14). Clearly such a development would greatly reduce the apparatus required in the entire experimental cycle. Directing the light through a one lens system makes it much
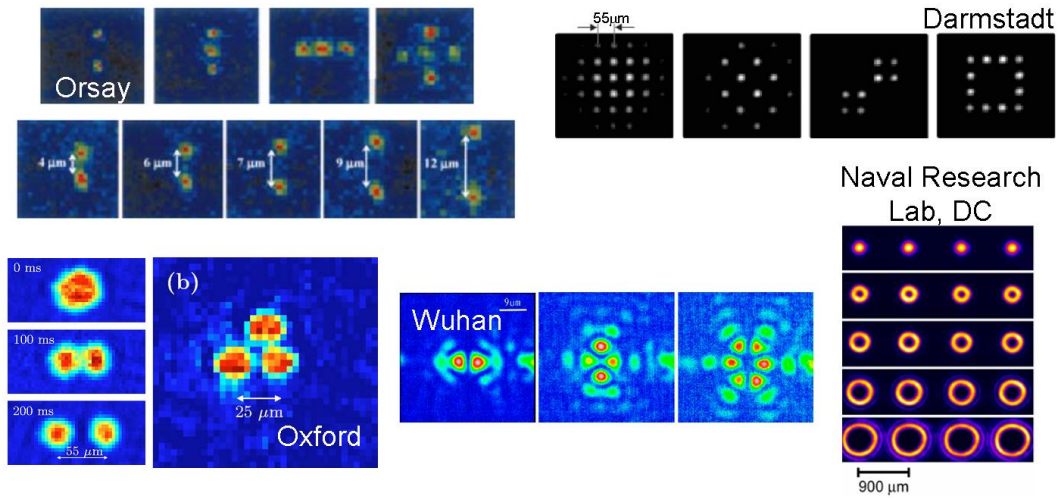
**Figure 1.5:** *Holographically generated atom traps to date. Clockwise from top left: arrays of dipole traps for single atoms [121] and for tens of atoms (in conjunction with a microlens array) [124]. Arrays of blue-detuned Laguerre-Gauss traps [125] and interfering red-detuned Laguerre-Gauss beams for single atoms [126]. Splitting and transport of BEC in up to three components [123].*

easier to change the configuration of the trap compared to counter-propagating laser beams.

Holographic atom traps have a number of limitations: in addition to the expensive nature of dynamic devices, the minimum spacing between wells is about twice that for multiple-beam interference, as the smallest possible feature that can be programmed holographically is the diffraction limit of the focussing optics. Recent progress in single-atom imaging [127, 128] may, however, present an opportunity in which the sub-micron resolution of the quantum gas microscopes can be used as the diffraction limit of a holographic optical trap. Although 3D holography is possible, the complexity of the possible intensity patterns is reduced [129]. The limited resolution of the devices will always present a limitation to the spatial frequencies obtainable in the intensity patterns, and the dynamic control of the devices may be too slow for some applications.

## 1.8 Scope of the Report

The main goal of the cold atoms group in St Andrews is to cool a Bose-Fermi mixture of $^{87}$Rb and $^6$Li to quantum degeneracy for investigations of condensed matter phenomena with cold atoms. This quantum degenerate mixture will be produced in a compact apparatus with the long-term view of creating highly-flexible quantum simulators.

To reduce the experiment size, we have investigated the use of the pulsed dispensers and the LIAD techniques to allow the whole cooling and experimental pro-

cess to take place in a single vacuum chamber. The flexibility of the apparatus will be provided by use of a Spatial Light Modulator to generate dynamic, arbitrary optical potentials.

This thesis is devoted only to the work done with $^{87}$Rb, but some discussion of the dual-species apparatus will be presented in Chapter 2. In this apparatus, we studied both methods for pulsed loading of the Magneto-Optical Trap and learned lessons which were crucial to the development of a second compact apparatus for Rb alone. This second apparatus used the LIAD effect to control the Rb vapour pressure, and is discussed in Chapter 3.

In Chapter 4, I will outline our investigations of holographic atom traps generated using Spatial Light Modulators. I will show our results in creating the first arbitrary and dynamic holographic traps which are suitable for the manipulation of ultracold gases, which rely on an adaptive-optics approach. I will also present our proposal of an efficient alternative approach achieving Bose-Einstein Condensation in a power-law trap and highlight a holographic ring trap to enable the investigation of superfluidity in cold atoms.

The possible combination of pulsed MOT loading and a fast, efficient evaporative cooling strategy in a flexible trap will allow for compact production and highly-controlled manipulation of ultracold gases.

# Chapter 2

# Pulsed Loading of a Rubidium Magneto-Optical Trap in a Stainless Steel Vacuum System

## 2.1   Introduction

Our original experimental apparatus was designed for simultaneous trapping and cooling of $^{87}$Rb and $^6$Li with a view to reaching quantum degeneracy of both. This chapter will outline the experimental setup for single-species trapping of Rubidium, and the investigation of pulsed techniques for the loading of this MOT. The results of these measurements are reported, and a second experimental setup is motivated. As motivated in Chapter 1, we design a compact cold atom apparatus around a single vacuum chamber and use pulsed dispensers and LIAD to vary the background pressure with the aim of loading large MOTs while reducing the background pressure in the chamber during later stages of the experiment.

Atomic rubidium is commonly used in cold atom experiments, due to the ready availability of cheap diode lasers at a wavelength appropriate for laser cooling. Although $^{85}$Rb is the more abundant isotope (72% of natural abundance), $^{87}$Rb is a common choice for experiments directed towards Bose-Einstein Condensation due to favourable collisional properties at a wide range of magnetic fields, which enables straightforward evaporative cooling.

Sections 2.3.1 - 2.3.8 outline the techniques we have used and show the exact layout of our experiment. Although the trapping of Lithium is also investigated in this apparatus and areas of the setup which are common to both will be laid out, the independent parts of the Lithium setup will not be detailed here, and can instead be found in [130].

## 2.2   Ultra-High Vacuum Setup

Investigations of atomic gases at sub-Kelvin temperatures can only be undertaken if the gas is thermally isolated from all sources of heating. This is accomplished by trapping the atoms in magnetic or optical fields within vacuum, in order to reduce

conductive heating. In order to minimise collisions between trapped and untrapped atoms and prolong the lifetime of the trapped cloud, ultra-high vacuum (UHV) conditions must be maintained.

To achieve these UHV conditions, we built a vacuum system based around a 10-way stainless steel cross, as shown in Figure 2.1, with the ConFlat connection standard. All ConFlat vacuum pieces terminate in a sharp knife-edge, and a seal is accomplished by placing a copper gasket between two of these terminations and tightening mechanically until the knives have cut into the soft copper of the gasket. This tightening must be performed evenly around the flange by alternately tightening the screws, in order to avoid having the knife-edge enter the copper at one angle when the first screw is tightened only to be moved to another angle when another screw is tightened, which would reduce the quality of the seal. The six mutually-orthogonal flanges of the cross are 70mm in diameter, whilst the other four have a smaller diameter of around 2.5cm. The four smaller flanges and two of the larger ones are used for optical access for the MOT beams, while three more of the larger flanges also accommodate viewports to allow increased optical access.
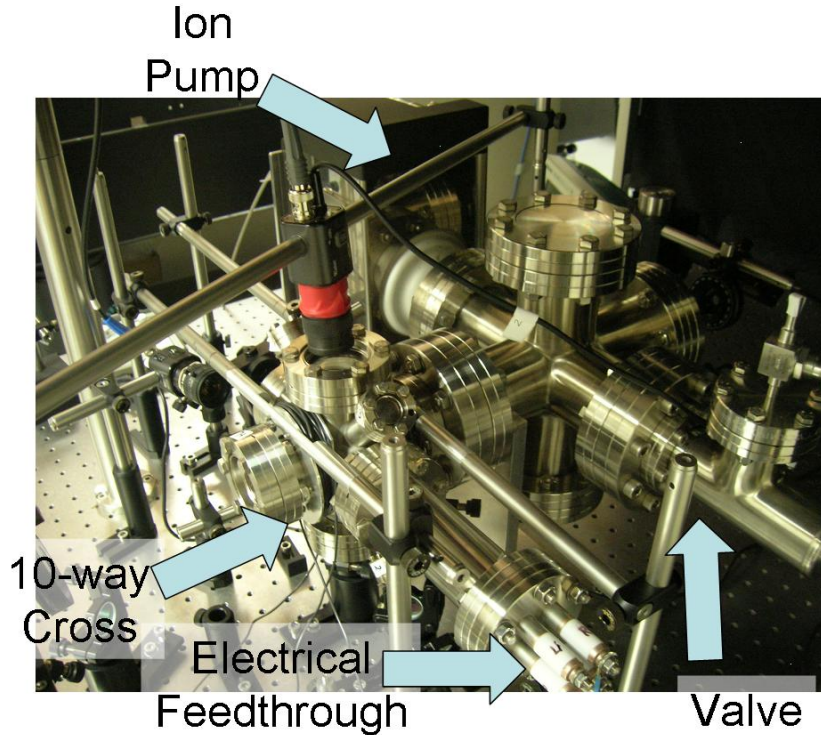


**Figure 2.1:** *The assembled vacuum system, showing all major components.*

One of the remaining flanges is sealed by an electrical feedthrough (VacGen Part Number ZEFT34A). Four 125mm long, 5mm diameter stainless steel rods protrude into the vacuum chamber and the ends are tapped to provide screw terminals. The rods are insulated at the point where they are connected to the flange and exit the vacuum chamber. Inside the vacuum, pairs of these rods are connected by two alkali metal dispensers (SAES RB/NF/7/25 FT10+10 and LI/NF/7/25 FT10+10), in order that a current may be passed through them. The dispensers are steel

$12 \times 1.12 \times 1.35$ mm containers (Figure 2.2) of a few mg of alkali-metal chromate ($Rb_2CrO_4$ or $Li_2CrO_4$) and a reducing agent (ST101 - a mixture of Zr and Al). These containers have a slit in the long side and emit atoms via a reduction reaction when the dispenser is heated, e.g. resistively. The reducing agent absorbs all other chemicals produced in the reaction, ensuring that the alkali metal alone is propelled out of the slit. The dispensers are installed 13cm from the trapping region, and exhibit a current threshold below which no atoms are emitted. Rubidium dispensers contain enough rubidium for us to run our experiment without changing dispenser for at least two years. When we have replaced them we have noted that the current threshold varies from one dispenser to the next: typical values range from 2.5A to 3A.
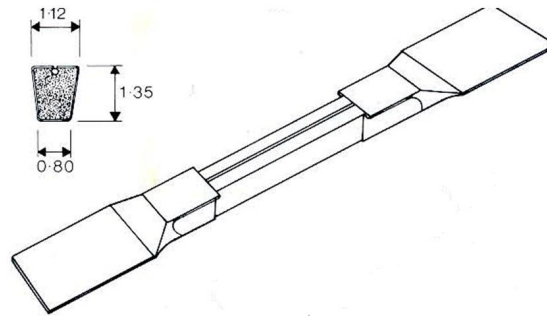


**Figure 2.2:** *Schematic of a SAES alkali-metal dispenser.*

The 10-way cross is connected via a 6-way cross to a 55l/s Varian Starcell ion pump and, during evacuation, a mechanical turbo pump (Varian Turbo - V70D).

The ion pump consists of two electrodes operated at high voltage. Free electrons travel between the electrodes and ionize gas particles in the vicinity, which are then attracted to the cathode where they remain. As this does not remove particles from the vacuum system, but merely captures them electrostatically, the ion pump has a long but finite lifetime. To avoid shortening the lifetime, the vacuum is initially achieved using the turbo pump which does actively remove particles from the system. The ion pump is then switched on to improve and maintain the UHV conditions.

To ensure a high-quality vacuum all components except the dispensers are firstly cleaned with methanol and de-ionised water in an ultrasonic bath, before being heated to a high temperature to release any contaminants from the surfaces of the components. (We note that components with glass-to-metal transitions, such as viewports, occasionally display some discolouring when cleaned with methanol or acetone. If this occurs, these viewports are not trusted to maintain UHV conditions anymore. In subsequent iterations we have used isopropanol to clean viewports.) High-temperature cleaning, also known as baking or bakeout, is achieved by wrapping the vacuum apparatus in resistive heating tapes and aluminium foil. Heating is performed by gradually increasing the current to the tapes by means of a variable transformer and monitored by attaching thermocouples to various parts of the apparatus. In order to avoid damaging any vacuum components, particularly glass, it is important to minimise both spatial and temporal gradients of temperature. Baking is performed with the turbo pump connected and switched on, while the ion pump is left off in order to preserve the lifetime of the pump.

While the temperature is high, the dispensers are activated and decontaminated (degassed) by passing a high current through them. We typically pass 5A through the dispensers, and watch the pressure rise on an ion gauge connected to the turbo pump. During degassing, the pressure rises quickly and then decays back toward the pre-degas pressure. Degassing is said to be complete when a much slower increase in the pressure, which is indicative of the emission of some of the dispenser's atomic content, is observed. We heat the chamber to 250°C for 14 days until the pressure, which rises upon heating, decays back below the pre-bakeout pressure. At this point the system is gradually cooled down to room temperature, before the ion pump is switched on to lower the pressure further. The turbo pump remains on until after the ion pump is switched on, as we have observed that the ion pump tends to emit some gas into the chamber when it is first switched on. Once this small pressure increase has disappeared, we close the valve and switch off the turbo-pump. After baking the whole vacuum at 250°C for around a week, we obtain a base pressure of $10^{-10}$ mbar.

## 2.3 Rubidium Laser System

Cooling of Rubidium-87 is performed by cycling atoms on the D2-line (as shown in Figure 2.3), specifically the F= 2 $\longrightarrow$ F$'$ = 3 hyperfine transitions, where F denotes the state within the $5^2S_{\frac{1}{2}}$ energy level, and F$'$ denotes the state within the $5^2P_{\frac{3}{2}}$ level. The presence of the detuning $\delta$ required for laser cooling means that there is an increased probability of exciting atoms from the F = 2 to the F$'$ = 2 level, from which they can emit a photon and enter the F = 1 state. As the energy separation between the F = 1 and F = 2 states is almost 7GHz the cooling laser no longer excites these atoms to the upper manifold, and they would be lost to the cooling cycle. To avoid this, a second laser known as the repumper is used to bring the atoms back to the F$'$ = 2 hyperfine state, from which they may return to the cooling cycle. This laser has relatively low power as it is not required to perform any cooling directly, merely to increase the efficiency of the cooling cycle.

In order to successfully trap the atoms, the laser light must be locked to the correct frequencies for the repumper and cooling transitions, then split into the appropriate beams to form the optical molasses.

### 2.3.1 Lasers

To generate the light used for laser cooling, we use two External Cavity Diode Lasers (ECDLs): a Toptica Model DL100 mount with a Toptica LD$-$0785$-$P220-1 laser diode for the light which is used for the cooling transition in Figure 2.3, and a homemade cavity and Sanyo DL7140-201S diode for the repumper light. The cooling laser gives around 80mW of output power, while the repumper gives about 15mW. The frequency of a diode laser can be varied by any of three controls: the diode temperature, the diode driving current, and optical feedback using an external cavity.

Control circuits are used to stabilise the temperature of the diode mount and of the diode independently by means of thermistors and Peltier cooling elements
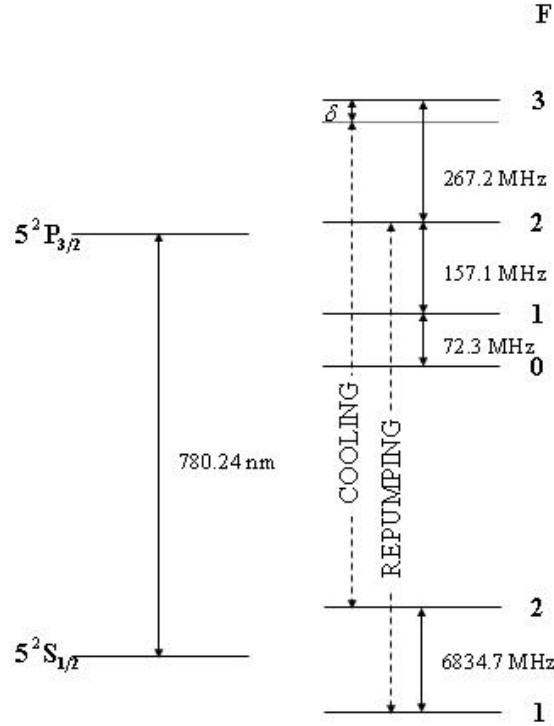
**Figure 2.3:** *The D2 Line of $^{87}Rb$, showing cooling and repumping transitions and the detuning $\delta$ required for laser cooling.*

(LairdTech CP14-71-045C) to 20.5°C and 21.0°C for cooling and repumper laser respectively, giving a wavelength around 780nm.

The current and the grating angle and cavity length can be controlled electronically by a lock-in amplifier which keeps the laser frequency locked to an external resonance signal (see Section 2.3.2) by applying small modulations (dither) to the laser current and monitoring the frequency response. Feedback is provided by setting up the ECDL in the Littrow configuration, where the first diffracted order of a 1200 lines mm$^{-1}$, 500nm blazed aluminium diffraction grating is incident upon the diode and the zeroth diffracted order forms the laser output. The grating used in our experiment returns 33% of the light to the diode, while the remaining power is used to form the output. The feedback narrows the linewidth, which also allows the frequency to be controlled. A piezoelectric transducer placed behind the grating allows for fine adjustments of the angle of the grating. A slower triangular waveform modulation (sweep) is applied to this piezoelectric transducer to allow one to perform spectroscopy by scanning over a range of frequencies. During experimental operation this sweep range is set to zero to keep the lasers locked to an atomic transition. During typical use we drive the diodes at 125mA for the cooling laser and 61mA for the repumper.

As the output beam from the ECDLs has an elliptical profile, we use anamorphic prisms to change the size of the beam along one axis only, in order to give a circular beam profile. We also use optical isolators to prevent unwanted optical feedback into the laser diodes, which can cause problems when frequency-locking is attempted.

In our setup, both beams are locked to an appropriate atomic transition by means

of Doppler-free Saturated Absorption Spectroscopy, by splitting a small amount of power from the main beam path using a $\frac{\lambda}{2}$ waveplate and a polarising beam splitter.

## 2.3.2 Locking the Laser Frequency with Doppler-Free Saturated Absorption Spectroscopy

If an atom is illuminated by a laser beam with frequency close to one of the atomic transitions, it will absorb a photon and enter an excited state. The atom returns to a non-excited state by spontaneous emission of a photon in a random direction and the intensity of the laser beam will decrease slightly. If the laser beam passes through many such atoms, its intensity can be considerably reduced. If we scan the laser frequency using the piezoelectric transducer, the absorption for different frequencies can be measured using a photodiode and plotted on an oscilloscope - this process is known as optical spectroscopy.

The Doppler effect causes the peaks in the absorption spectrum to be broad and individual transitions cannot be identified, so this method is not ideal for frequency stabilization of the laser beam to an individual transition for laser cooling. However, if two counter-propagating laser beams are used - a strong pump beam with $I >> I_{sat}$ to saturate the transition ($I_{sat} = \pi h c \Gamma / 3\lambda^2$ is the saturation intensity of a transition) and a weak probe beam - new peaks appear across the Doppler profile in the absorption spectrum of the probe beam. This technique is known as Doppler-free Saturated Absorption Spectroscopy and the lasers can be reliably locked to an atomic transition using this technique, which is outlined in Figure 2.4d)-f) for an atomic species with well-resolved hyperfine levels in both manifolds, such as $^{87}$Rb.

In Figure 2.4d), the atoms are illuminated by a probe beam resonant with one of the transitions and a far-off-resonant pump beam. The absorption is Doppler-broadened as only one beam interacts with the atoms, giving a Gaussian profile centred around the resonant frequency, which is the underlying "Doppler profile" in Figure 2.4c).

The case of both Doppler-shifted beams resonating with the same transition is shown in Figure 2.4e). The pump beam excites most of the atoms into the upper state, meaning that the probe beam absorption is lower. This saturation of the absorption leads to a narrow peak, or Lamb dip, in the probe transmission about the resonant frequency, such as the leftmost peak in Figure 2.4c) (the $^{87}$Rb cooling transition).

If the beams are resonant with different transitions, as in Figure 2.4f), the pump beam once again depletes the number of atoms available for excitation by the probe beam, again giving a local peak in the transmission signal. This peak is not representative of a true transition; rather it depicts the "crossover" between the two transitions, such as the rightmost peak in Figure 2.4c), which is the crossover between the F = 2 $\longrightarrow$ F′ = 1 and F = 2 $\longrightarrow$ F′ = 3 transitions shown in Figure 2.3.

We employ identical configurations for Saturated Absorption Spectroscopy of both the cooling and repumper lasers. Our pump beam is directed through a glass cell containing room temperature rubidium vapour, before being retroreflected and attenuated to form the probe beam, as shown in Figure 2.4a). We also alter the
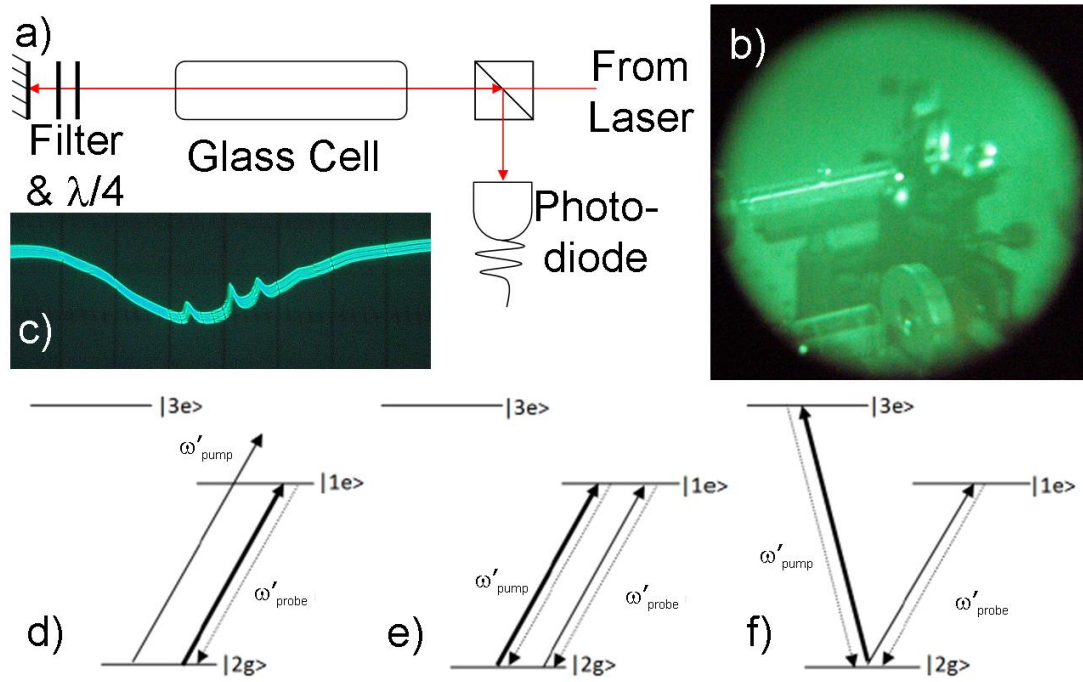
**Figure 2.4:** *Saturated Absorption Spectroscopy. a) Schematic of the experimental setup. b) The rubidium atoms in the glass cell can be seen fluorescing when the lasers are tuned close to resonance. c) The transmission spectrum of the probe beam showing the $^{87}Rb$ $5^2S_{1/2}$ $F = 2 \to 5^2P_{3/2}$ transitions and crossovers. d) The underlying Gaussian profile in c) is due to absorption of one beam only. e) The leftmost peak in c) is a Lamb dip corresponding to a transition, which occurs when both Doppler-shifted pump and probe are resonant with the same transition. f) The rightmost peak in c) is a crossover, which occurs when Doppler-shifted pump and probe are both resonant, but with different transitions.*

polarization of the retroreflected beam by 90° using a waveplate so that the returning light is separated from the incoming beam using a polarising beam splitter (PBS). This means that pump and probe beams have the same frequency, but as they are counter-propagating they can interact with different velocity classes of atoms via the Doppler effect. Around $100\mu$W are used for the spectroscopy, allowing most of the power to be used for other purposes (see Sections 2.3.3 - 2.3.8).

The saturated absorption spectrum is detected by a photodiode and sent to the lock-in amplifier, which differentiates the photodiode signal to give an error signal. This signal controls the laser diode current and the piezoelectric transducer (ECDL grating) to keep the frequency tuned to the local zero of the error signal, i.e. the local peak in the transmission profile.

For the repumper laser, we lock directly to the F $= 1 \longrightarrow$ F $' = 2$ transition. However, as the crossover peak shown in Figure 2.4c) is very visible and is 212 MHz below the F $= 2 \longrightarrow$ F$' = 3$ cooling transition, we choose to lock to this feature rather than the actual transition. The laser frequency can easily be shifted using an Acousto-Optic Modulator (AOM, see Section 2.3.3), which are typically provided at an optimal tuning frequency of 110MHz or 200MHz with a bandwidth of around $\pm30$MHz. The 212MHz detuning that we achieve by locking to the crossover can therefore easily be tuned to experimental values of $5 - 50$MHz. If we were to lock directly to the transition, it is harder to detune the laser by the few MHz required.

### 2.3.3   Detuning the Cooling Laser

As indicated in Section 2.3.2, the cooling light is next sent to an Acousto-Optic Modulator (AOM) in cat-eye configuration to achieve the detuning necessary for Doppler cooling.

An AOM shifts the frequency of an incident light beam by Bragg-like diffraction from an oscillating piezoelectric crystal. An a.c. radio-frequency electrical signal is sent to the crystal by a Voltage Controlled Oscillator (VCO), generating a travelling acoustic wave in the crystal. These moving periodic planes of compression and expansion produce a periodic variation in the refractive index. As the planes are moving in this grating, the diffracted orders are frequency-shifted by an integer multiple of the oscillation frequency and each order is diffracted at a different angle. By changing the angle of the incident beam relative to the crystal, biased diffraction can be achieved, so that up to 80% of the power can be diffracted into either first order.

An AOM used in double-pass can be arranged in the so-called cat-eye configuration (Figure 2.5): the diffracted orders are collimated using a lens and retro-reflected by a mirror, while an iris blocks any diffracted orders which are not required by the experiment. A $\lambda/4$ waveplate is used to change the polarisation of the beam so that it can be separated from the incoming beam with a PBS. This configuration allows changes to the oscillation frequency whilst ensuring the retro-reflected beams still pass through the AOM. AOMs also benefit from fast switching, so when used in cat-eye configuration they also make excellent shutters: a feature we have used for taking absorption images of our atoms (see Section 3.7).

Our VCO signal is determined by two input voltages - which may be controlled
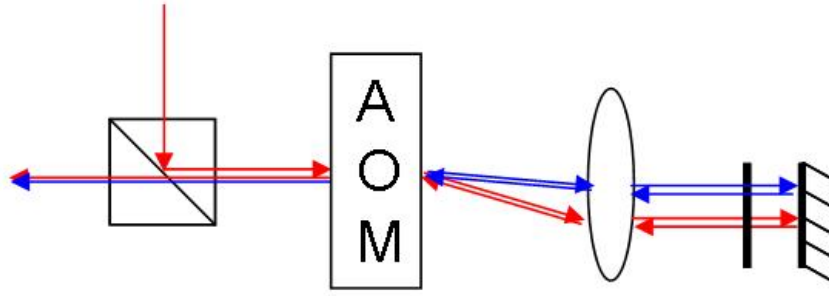
**Figure 2.5:** *By operating an AOM in double-pass cat-eye configuration, the detuning frequency can be varied without loss of alignment.*

using an internal potentiometer or an external voltage. The first of these, the attenuation, controls the amplitude of the sinusoidal signal, whilst the second controls the frequency of the signal.

As this signal tends to be quite weak, our VCO is attached to a radio-frequency amplifier (MiniCircuits ZHL-5W-1), which is then connected to our AOM (Crystal Technology Model 3110-120). Firstly, we connect the VCO to a radio-frequency power-meter and set the attenuation voltage such that the power is below the zero damage threshold for the amplifier.

Armed with this limit for the attenuation, we connect the amplifier to the VCO and the AOM, and optimise the first-order diffraction efficiency in the first pass using alignment and by varying the attenuator input. As we have locked the laser 212 MHz below the transition we want, we drive the AOM at $106 - \delta/2$ MHz, where $\delta$ is the desired detuning.

The VCO also has an external TTL control, which acts as an on / off switch for the signal. When this TTL receives 0V, the signal is not sent to the amplifier, and therefore the AOM diffraction is stopped, leaving us with only the zeroth-order beam (which is blocked), allowing us to turn off the beam if we wish. Even when the beam injects the AOM at the appropriate Bragg angle, power losses due to the optical isolator and the double-pass of the AOM leaves us only 40% of the cooling power. In order to maximise the power available for laser cooling, we decide to use another diode laser in a master-slave configuration.

## 2.3.4 Increasing the Cooling Power: Slave Laser

As we are now limited to around 35mW for the cooling beam, we decide to use an additional free-running diode laser in a master-slave configuration to increase the power available for cooling. By splitting the output from the double pass on a PBS, we send around 2mW to the slave laser and the rest can be used to generate additional laser beams required in different stages of the experiment (e.g. in Section 2.3.5). We operate this slave laser at the frequency required for MOT cooling by "seeding" the diode with a small portion (around 1mW) of the light after the double pass of the AOM: stimulated emission causes the slave output to match the input from the master beam. This "injection locking" is performed by carefully overlapping the light coming from the slave diode with the seeding light beam. The

frequency of the slave beam is monitored by using a flip mirror to optionally send the beam through a Rb vapour cell and viewing the signal on an oscilloscope, where we see the Doppler profile for the $^{87}$Rb transition, without the Lamb dips associated with saturated absorption spectroscopy (see Section 2.3.2). This signal is compared to the absorption profile obtained for the master beam to ensure the laser output modes match. The offset seen in Figure 2.6 is due to the approximately 200MHz frequency shift applied by the AOM after the original spectroscopy (Section 2.3.3).
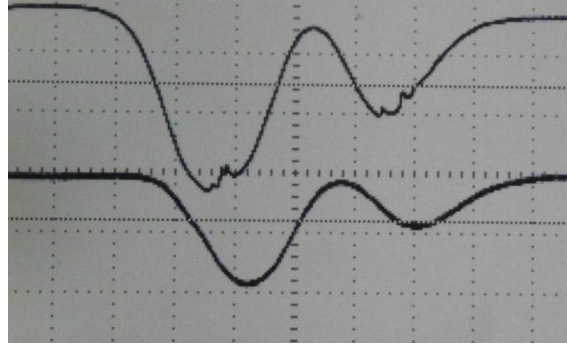


**Figure 2.6:** *An absorption profile for the slave laser output is shown below the saturated absorption signal for the master laser. The signal from the slave lacks Lamb dips as we only pass the beam through the Rb cell once, and is frequency shifted from the saturated absorption profile as the slave seeding beam is frequency shifted by a double pass AOM.*

In order to seed the slave diode whilst preventing unwanted feedback into the diode, we built our own optical isolator (see Figure 2.7), comprising two PBSs and one Faraday Rotator, where one PBS is mounted such that the p-polarization transmission axis is at 45° to the vertical. The seed beam is reflected from PBS B and passed through the Faraday rotator where its polarization is rotated by 45°. PBS A is aligned to transmit light with this polarization. As a result of this, any beams which are transmitted by PBS B toward the laser will be reflected by PBS A. The beam emitted by the slave has its polarization optimized for transmission through the isolator by rotation of a $\frac{\lambda}{2}$ waveplate.

The slave diode (Sanyo DL7140-201S) outputs a maximum of 85mW at a typical current of 108mA, and its temperature is stabilised to 21.6°C in the same way as the two ECDLs. The output profile is also improved using anamorphic prisms as in Section 2.3.1. As the output of the slave laser does not require any further manipulation in terms of frequency or shape, we have around 70mW to send to the MOT.

## 2.3.5   Imaging Beam and Optical Pumping

The remaining power from the master laser is used to generate two laser beams which will be used for imaging the cold atomic cloud and to aid in loading the atoms into a magnetic trap. To generate the two beams, we use another AOM to diffract the beam and use the zeroth and first orders.
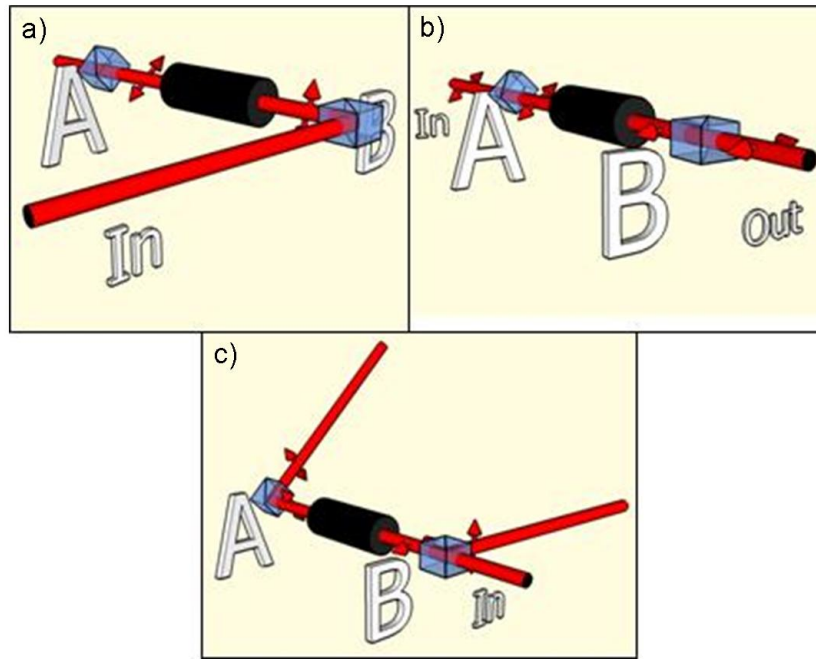
**Figure 2.7:** *The isolator on the slave path is constructed from two Polarizing Beam-splitter Cubes with their transmission axes differing by 45°, separated by a Faraday rotator. Beams are shown in red, with polarization indicated by the arrows. a) The slave laser is "seeded" by reflecting a beam at the desired frequency on PBS B which ensures the correct polarization for transmission by the isolator; b) ensuring the correct polarization of the slave laser beam before PBS A by rotation of a $\frac{\lambda}{2}$-plate, the output of the slave laser can be transmitted by the isolator; c) all polarizations of back-reflected light are reflected by the PBSs, ensuring no light reaches the diode.*

The zeroth order is not frequency-shifted by this AOM, and will be used in absorption imaging of the atomic cloud. By quickly varying the frequency of the detuning AOM in Section 2.3.3, we can bring this beam into resonance with the cooling transition: the cat-eye configuration of the first AOM ensures that we do not lose alignment in this change.

The first order beam is retroreflected so that it undergoes a double-pass in cat-eye configuration, so that we can change this frequency. This frequency shift can be used to bring the beam into resonance with a chosen hyperfine transition in order to force the atoms into magnetically trappable states via the method of optical pumping.

These two beams are recombined on a PBS, and sent to a single-mode, polarization maintaining optical fibre which will transport them to a second optical table housing the vacuum apparatus.

### 2.3.6  Switching of the MOT Beams

We have included a number of mechanical shutters in our setup in order to extinguish light within experimental sequences. These mechanical shutters are based around a simple relay (Omron G2R-1-E RDC) and a razor blade, and are placed in the focus of a telescope in order to quickly extinguish the light (switching time around 2ms). We have included one each on the repumper path and the slave path, as well as one which will block both beams simultaneously. The way in which we generate the imaging and pumping beams requires an additional shutter to be placed on the imaging beam path so that it is blocked during the MOT and optical pumping phases. We can also use the AOM of the master beam to quickly switch off the imaging beam, while we use the second AOM in section 2.3.5 as a fast shutter (a few $\mu$s switching time) for the optical pumping beam.

### 2.3.7  Complete Setup for Cooling $^{87}$Rb

The full optical setup is shown in Figure 2.8. For each beam splitting operation, we use $\frac{\lambda}{2}$ waveplates to control the power reflected and transmitted by the PBS. We combine the cooling and repumper beams using a PBS and send this combined beam and the imaging beam to two separate single-mode, polarization maintaining optical fibres. The last component before each fibre is a $\frac{\lambda}{2}$ waveplate, in order to match the polarization of the beams to the fast- or slow-axis of the fibre. This helps to minimise fluctuations in both power and polarization of the beam which exits the other end of the fibre. The fibre safely transports the light to the second optical table where the vacuum chambers are mounted and offers a security of alignment to the system: any changes which are made to the optical setup on the first table do not change the alignment on the second table. An added benefit is that the fibre acts as a spatial filter and provides a Gaussian laser beam intensity profile at the output, which is beneficial for magneto-optical trapping. Our optical fibre typically transmits 75% of the cooling power and 55% of the repumper power to the second optical table.
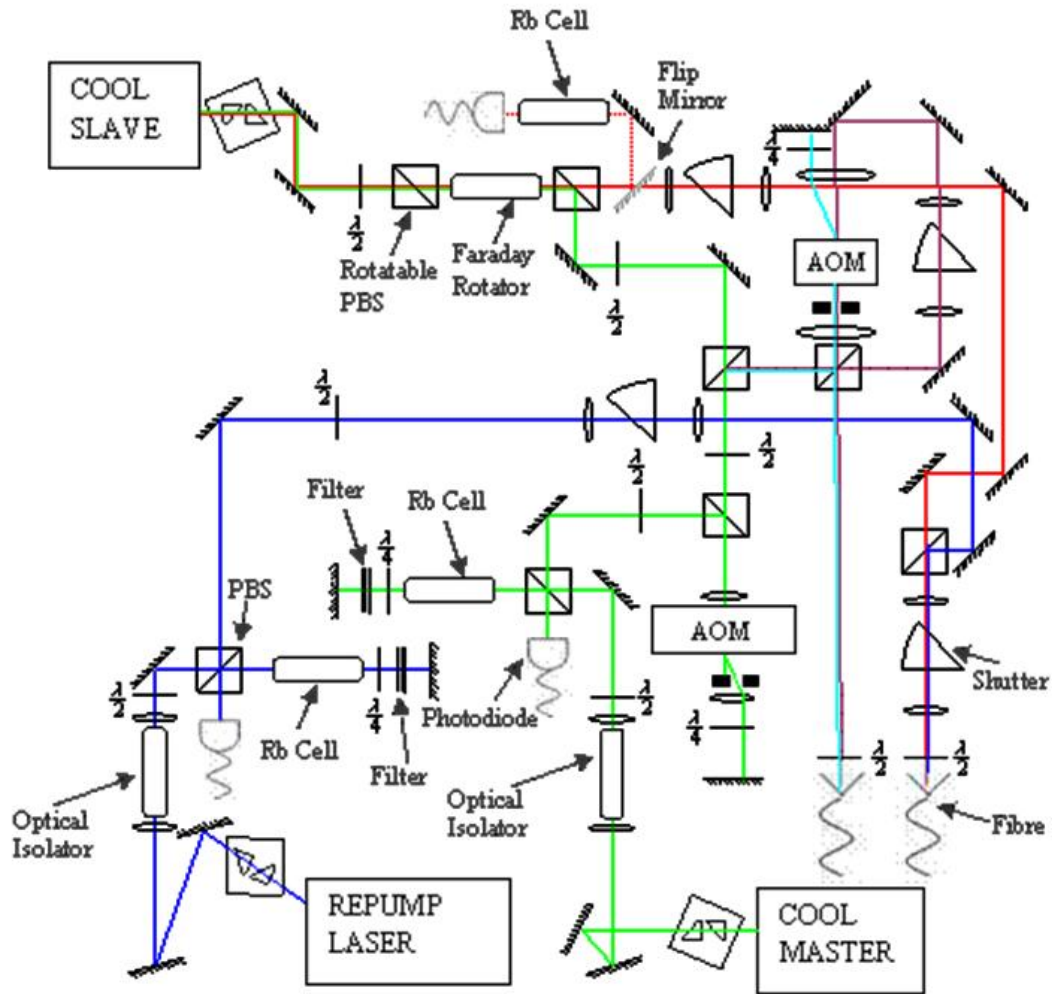
**Figure 2.8:** *The optical arrangement that produces cooling master (green), slave (red), repumping (blue), optical pumping (cyan) and imaging (purple) beams for* $^{87}Rb$.

### 2.3.8   MOT Beams

The fibre output is collimated to a $\frac{1}{e^2}$ beam waist of 7mm $\pm 2.8\%$ using an achromatic doublet lens with $f = 70$mm, providing a nearly-perfect Gaussian profile. We also have two optical fibre outputs delivering 670nm light to this table for the laser cooling of lithium, and the two wavelengths are combined into a single beam using a dichroic mirror and broadband PBSs.

The combined bichromatic beam is then divided into six individual beams using PBSs and $\frac{\lambda}{2}$ waveplates, and directed into the stainless steel vacuum system detailed in Section 2.2. One pair of beams counter-propagate in the horizontal plane, while the other two pairs are in the vertical plane and orthogonal both to each other and to the horizontal beams. The power in all the beams is balanced by rotating the $\frac{\lambda}{2}$ waveplates before the splitting PBSs. The beams are given the appropriate circular polarisations for efficient magneto-optical trapping by means of $\frac{\lambda}{4}$ waveplates after the last mirror on each path. The power available for laser cooling is 4.0mW per cooling beam, with a total power of around 1.5mW for the repumper. The full paths are shown in Figure 2.9.
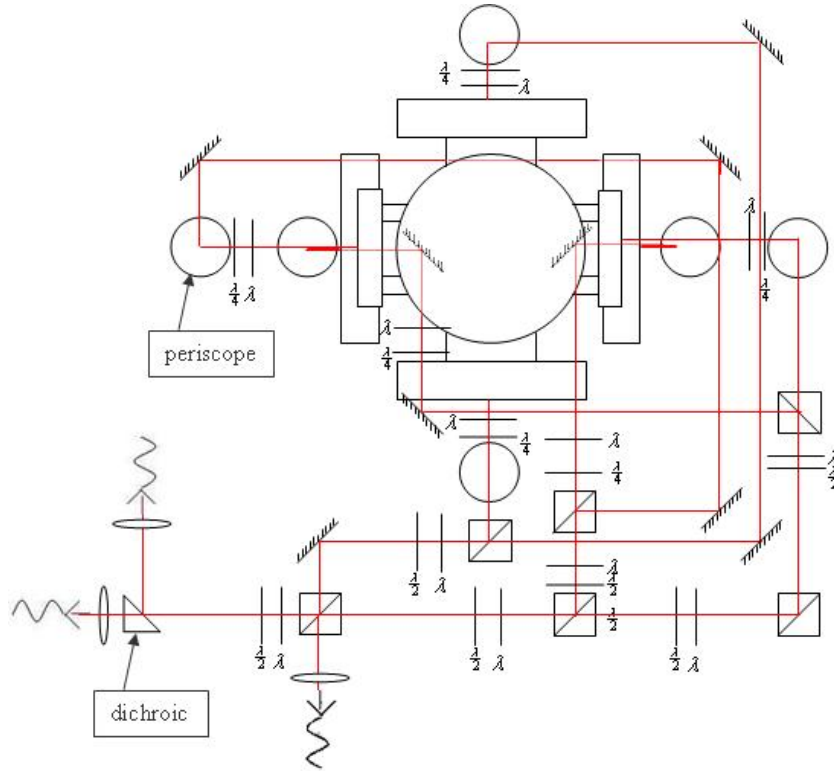


**Figure 2.9:** *The beam combination and splitting setup for the MOT.*

Whilst we use broadband PBSs, we could find no single waveplate which gave us the correct polarizations for both wavelengths. We have decided to use a $\frac{\lambda}{2}$ $\left(\frac{\lambda}{4}\right)$ waveplate (as appropriate) at 780nm, followed by a $\lambda$ waveplate at 780nm. The full-wave plate does not affect the 780nm beam polarization, but the combination of waveplates acts as a $\frac{\lambda}{2}(\frac{\lambda}{4})$ waveplate for the 670nm beam. This effect was previously demonstrated in an experiment to simultaneously trap three atomic species [131].

## 2.4 Magnetic Field Generation

### 2.4.1 MOT Magnetic Field

The magnetic field produced along the symmetry axis $z$ of a circular current loop is:

$$B\left(z\right) = \frac{\mu_0 a^2 I N}{2\left(a^2 + z^2\right)^{\frac{3}{2}}}, \tag{2.1}$$

where $N$ is the number of turns, $I$ is the current and $a$ is the coil radius

If we have two concentric coils with currents in opposite directions separated by $d$ the magnetic field along the z axis is:

$$B\left(z\right) = \mu_0 a^2 I N \left(\frac{1}{2\left(a^2 + \left(\left(z - \frac{d}{2}\right)^2\right)^{\frac{3}{2}}\right)} - \frac{1}{2\left(a^2 + \left(\left(z + \frac{d}{2}\right)^2\right)^{\frac{3}{2}}\right)}\right), \tag{2.2}$$

which satisfies the condition that $B\left(0\right) = 0$, where $z = 0$ is the midpoint between the coils. As discussed in Section 1.3, a MOT requires a constant field gradient between the coils: which is only necessarily the case for values near $z = 0$. However, if we set higher derivatives of the magnetic field to zero, we have a pure linear gradient between the coils. The second order derivative is necessarily zero (by symmetry), as are all higher-order even derivatives. The third derivative can be set to zero by setting $d = \sqrt{3}a$ - this is the anti-Helmholtz condition. The geometry of our vacuum system dictates $a$ and $d$, which are 34.5mm and 60mm respectively.

Typical MOT experiments use a magnetic field gradient of around 15 G cm$^{-1}$ at $z = 0$. To achieve this at modest current, we chose $I \approx 5$A and $N = 45$. We connected the coils in series to allow us to switch them on or off simultaneously.

The MOT coils are mounted on an aluminium support around the horizontal flanges of the vacuum system. The design of the supports also gives us scope for small movements of the coils both along their axis, and in the plane perpendicular to it by keeping an air gap between the mount and the flange. This also helps us to avoid heating the chamber when the coils are warm.

### 2.4.2 Compensating Stray Fields: Shim Coils

Ideally, the zero-field would be at the intersection point of the three pairs of counter-propagating beams. However, due to the restrictive geometry of our system and some external magnetic fields such as the Earth's magnetic field (0.6G) or stray magnetic field from the ion pump, this is not the case. These effects can be limited by the addition of individually controlled shim coils along each Cartesian axis.

We measure the stray fields to be less than 1G, and want to run the coils at a low current ($I < 2$A) with only a moderate number of turns ($N \approx 90$). The size of the coil is limited by the MOT beams, and so we choose to use 10cm radius coils placed 6cm from the MOT.

For simplicity of construction we use square coils rather than the usual circular coils. The magnetic field strength along the axis of a square coil of side length $L$ is given by

$$B\left(z\right) = \frac{2\mu_0}{\pi} \frac{L^2}{2} \frac{IN}{\left(\left(\frac{L}{2}^2 + z^2\right)\left(2L^2 + z^2\right)^{\frac{1}{2}}\right)}. \tag{2.3}$$

For the same values of $z$ and $N$, and $L = 2a$, these coils generate a magnetic field strength of around 2.2 G A$^{-1}$, which does reduce the offset between the magnetic field zero and the laser beam intersection.

This setup is sufficient for successful observation of and experimentation with a MOT, but for future cooling steps the shim coils would ideally be used not to offset the MOT position but to ensure homogeneous expansion of the MOT when the trapping gradient is switched off. In this system, the MOT always moves toward the ion pump as it expands, which would not allow for an efficient optical molasses cooling stage.

## 2.5 Computer Control of the Experiment

A complete computer control program has been built for the experiment using Lab-View v8.5 and National Instruments PCI cards (PCI-6723 and PCI-6229). This can be used to send analogue or digital signals to control most of the devices used in the experiments. The reading from the photodiode in Section 2.6.1 is acquired, and the number of atoms is calculated using (2.4) and displayed in real-time. We also directly control the current passing to dispensers, magnetic coils and LEDs, as well as VCO attenuations, AOM TTLs, shutters and camera TTLs. All experimental sequences (even those taking place over a long timescale) are preprogrammed in LabView for accuracy. The LabView front panel is shown in Figure 2.10.

The PCI-6723 offers us 32 Analogue Outputs in the range $\pm$ 10V with an accuracy of 11mV with up to 800kSamples s$^{-1}$ and 8 5V Digital Outputs, while the PCI-6229 card we have chosen offers us 32 Analogue Inputs and 4 Analogue Outputs at 50ns resolution, over a range of $\pm$10V at 3mV resolution. Additionally we can make use of up to 48 Digital Outputs (0 or 5V) which can be refreshed at up to 1MHz. The timing of these channels can also be set by one of two gated counter outputs, which have a maximum clock rate of 20MHz. The two cards can be synchronised by means of an RTSI connection, or by using a Counter output from one card as an input trigger on the other. The PCI-6229 card is thus used to trigger the analogue channels on the PCI-6723 card.

## 2.6 Observation and Characterisation of a MOT

The alignment of the MOT beams is initially set by ensuring each beam passes completely through both viewports on its path. We then superimpose the pairs of beams by ensuring that they overlap on the last two mirrors of each optical path. In order to continuously monitor the MOT during alignment or laser locking,

**Figure 2.10:** *The LabView Experimental Control and Parameters programs, showing some of the experiment options.*

we collect the MOT fluorescence using a simple CCD video camera (Watec WAT 902 DM-2S). This also allows us to observe fluorescence of the laser beams alone, which is a useful method for further aligning and overlapping the beams within the chamber. By this means, we achieve a rough optimization of the beam alignment and polarization, before further optimization can take place. Final alignment is carried out by maximising the fluorescence collected by a photodiode, which gives us an indication of the atom number in the MOT.

### 2.6.1 Counting the Number of Atoms in the MOT

In order to further characterize and optimize the MOT, a quantitive value for the number of atoms trapped is required. To do this, we image the fluorescence from the MOT onto a photodiode (Thorlabs DET100A/M). The photodiode has been mounted above the MOT outside one of the viewports that is not used for the MOT laser beams. Scattered laser beams, fluorescence from atoms which are slowed but not trapped, blackbody radiation from the dispensers, and ambient light can all be collected by the photodiode. To take account of all of these, we record the photodiode reading with the MOT coils switched off, and subtract this background value from the signal obtained during the experiment. This difference is then entered in the formula

$$N = \frac{4\pi}{0.96^\kappa} \frac{\text{(photodiode current)}}{\Omega(\text{responsivity})(\text{photon energy})R}, \tag{2.4}$$

where $\Omega$ is the solid angle subtended by the photodiode collection lens with the MOT, $\kappa$ is the number of uncoated glass surfaces between MOT and photodiode (0.96 is the transmission of one of these), and $R$ is the photon scattering rate, which is given by

$$R = \frac{\Gamma}{2} \frac{\frac{I}{I_{sat}}}{1 + \frac{I}{I_{sat}} + 4\frac{\delta^2}{\Gamma^2}}, \tag{2.5}$$

with natural linewidth $\Gamma = 2\pi \times 6.07$ MHz, total incident intensity of all six beams $I$, saturation intensity $I_{sat} = 1.67$ mW cm$^{-2}$ and frequency detuning from resonance $\delta$.

### 2.6.2 Measuring the Pressure in the MOT region

In initial work with our experimental setup, we have used the driving current of the ion pump as an indicator of pressure within the vacuum system: as the pressure rises, the ion pump draws more current. However, after receiving a large shock due to an exploded rubidium dispenser, this current became unreliable as a reading of pressure. The standard method for measuring the pressure in the vicinity of trapped atoms is to fit the decay of atom number in a magnetic trap: using this method it is unfortunately difficult to measure rapid changes in the pressure as the decay curves typically last several seconds. Therefore, we have developed a novel technique for measuring rapid changes to the partial pressure of Rubidium in the MOT region.

The time dependence of the number of atoms in the MOT $N(t)$ can be expressed as the following differential equation:

$$\frac{\mathrm{d}N}{\mathrm{d}t} = \alpha\phi - (\beta\phi + \gamma)\, N, \tag{2.6}$$

where $\alpha$ denotes the trapping cross-section, which remains constant provided the MOT parameters are not changed, $\beta$ is losses due to collisions with untrapped Rb atoms, $\gamma$ is losses with other background atoms and $\phi$ is the Rb flux in the MOT region. The solution to this equation, which describes the evolution of the number of trapped atoms at constant atom flux from the dispenser, is

$$N(t) = N_{eq}\left(1 - \exp\left(-\left(\beta\phi + \gamma\right)t\right)\right), \tag{2.7}$$

where $N_{eq} = \frac{\alpha\phi}{\beta\phi+\gamma}$ is the maximum number of trapped atoms in the MOT. In the limit $\gamma \to 0$ (very clean vacuum) the equilibrium number of atoms trapped in the MOT is thus independent of the rubidium pressure.

At the beginning of a loading curve, $N = 0$ and $\frac{\mathrm{d}N}{\mathrm{d}t}|_{t=0} = \alpha\phi$, which is proportional only to the Rb background pressure. Thus in order to monitor the pressure, we take repeated partial MOT loading curves by pulsing the current to the MOT coils off and on with a period of 4s and an on-duration of 1s. The MOT loading in this regime is almost linear, so it is straightforward to extract the gradient. Although this measurement does not directly give a numerical value for the pressure, it is proportional to the pressure in the MOT region. We find this to be a more reliable indicator of the pressure than the ion pump current.

### 2.6.3  MOT Optimisation

The MOT is characterised by its loading curve, as measured using the photodiode. We optimize the number of trapped atoms in the MOT and the MOT loading time initially with beam alignment, power balance and polarization. Once the alignment is completed, we optimize further using the detuning and the magnetic field gradient.

A typical MOT loading curve is shown in Figure 2.11. By fitting this curve with an equation of the form

$$N(t) = N_{eq}\left(1 - \exp\left(\frac{-t}{\tau}\right)\right), \tag{2.8}$$

we can extract the equilibrium atom number $N_{eq}$ and the loading time $\tau$.

In the first version of the MOT in our apparatus, we did not use the slave laser. However, we found that by increasing the cooling power available, we were able to increase the size of the MOT (Figure 2.12). This was not the case for the repumper, however: the number of atoms in the MOT does not increase beyond with repumper power provided more than 0.5mW is available.

By varying the detuning and magnetic field gradient separately we optimize $N_{eq}$, as shown in Figure 2.13 at typical values of 18 G cm$^{-1}$ magnetic field gradient and $-13$MHz detuning.
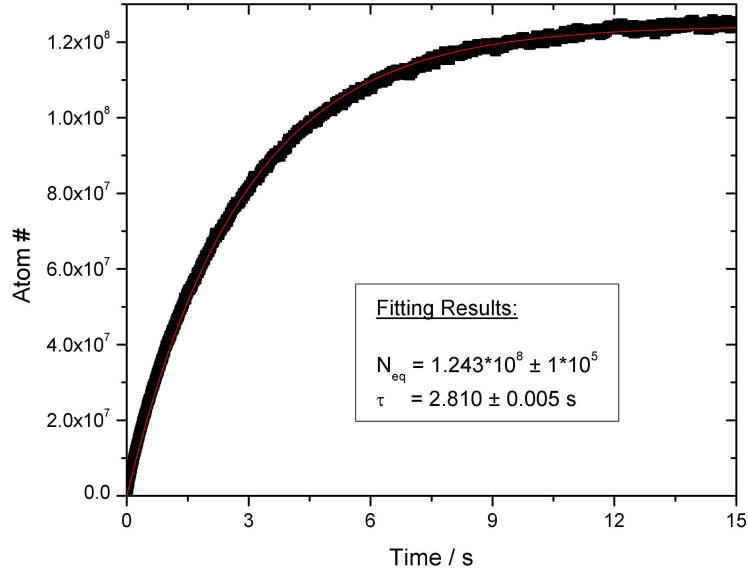
**Figure 2.11:** *Typical MOT loading curve when pressure is constant and dispenser is operating at 3.2A. Data is denoted by black points, while the fit given by (2.8) is the red line. Also shown are the extracted fit parameters for $N_{eq}$ and $\tau$.*
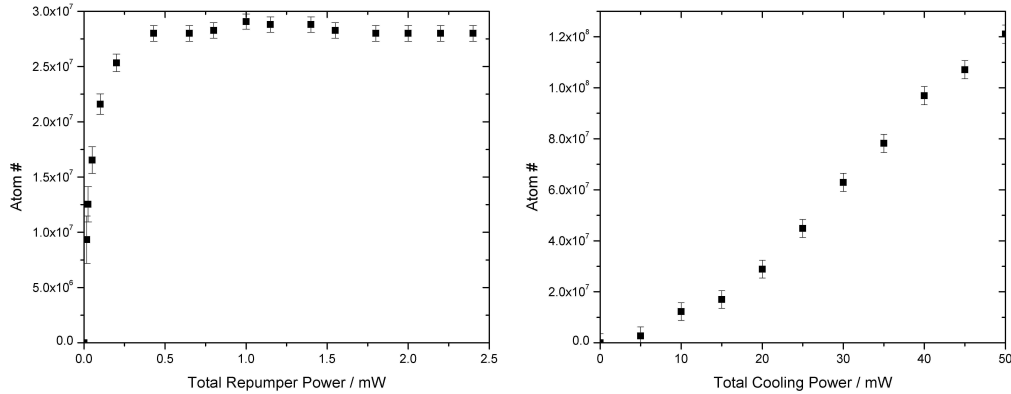


**Figure 2.12:** *(left) When the cooling laser power is kept constant and the repumper power varied, we find that the MOT size is independent of the repumper power above 0.5mW. (right) The number of atoms in the MOT does increase as we increase the cooling power, proving that the installation of the slave laser was beneficial.*
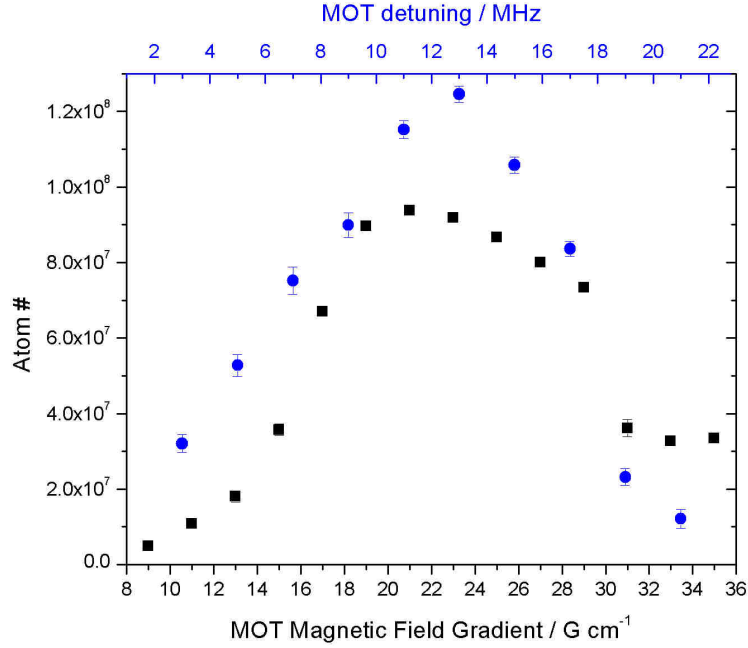
**Figure 2.13:** *Equilibrium number of atoms in the MOT versus magnetic field gradient (black) and cooling beam detuning (blue).*

## 2.7 Pulsing the Dispensers

### 2.7.1 Continuous Operation of the Dispenser

The pressure in the vacuum chamber is characterised by observing the increase from the base pressure for a variety of dispenser currents. We measure the build up of pressure as displayed on the ion pump controller against time (see Figure 2.14), and find that as we increase the dispenser current, the pressure in the chamber increases more quickly, and that a higher maximum pressure is reached. When the dispensers have been left off for a long time (e.g. overnight), the background pressure in our system loads $2 \times 10^7$ atoms in about 35s (loading time constant $\sim$ 10s), with an initial loading rate $2 \times 10^6$ atom s$^{-1}$.

By turning on the dispenser at 3.7A for 450s we can watch the MOT grow to $6 \times 10^7$ atoms, while the pressure (measured by MOT loading rate as in Section 2.6.2) also increases by a factor of 4 (Figure 2.15). We note a two-stage growth of the MOT and the pressure, similar to the unexplained findings in Reference [132]. The number of atoms in the MOT increases with time, obeying an exponential decay relationship for around 2 minutes before entering a regime where the number of trapped atoms increases linearly with time. If the dispenser remains at this current for a few hours, we load MOTs of $1.2 \times 10^8$ atoms with a lifetime of 4.2s.

We interpret the first regime as the flux of atoms emitted by the dispensers increasing with time. In the second regime the dominant increase is due to an increase in the temperature of the vacuum chamber due to thermal conduction and
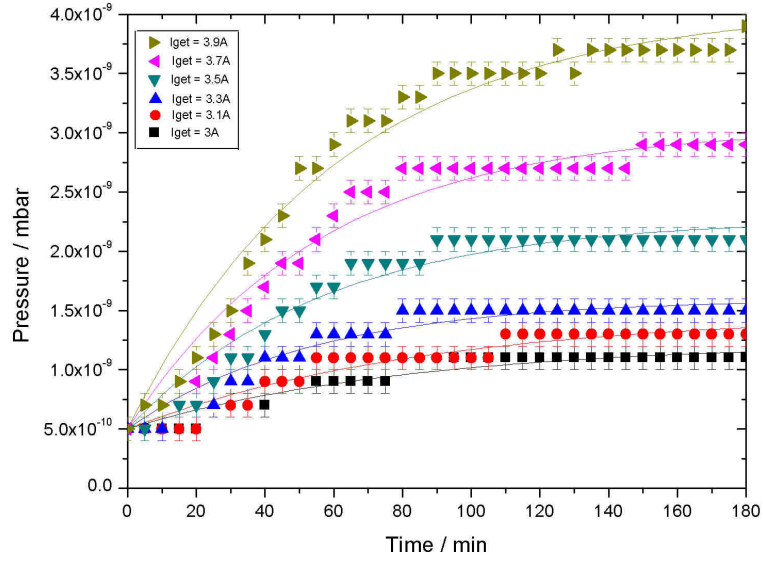
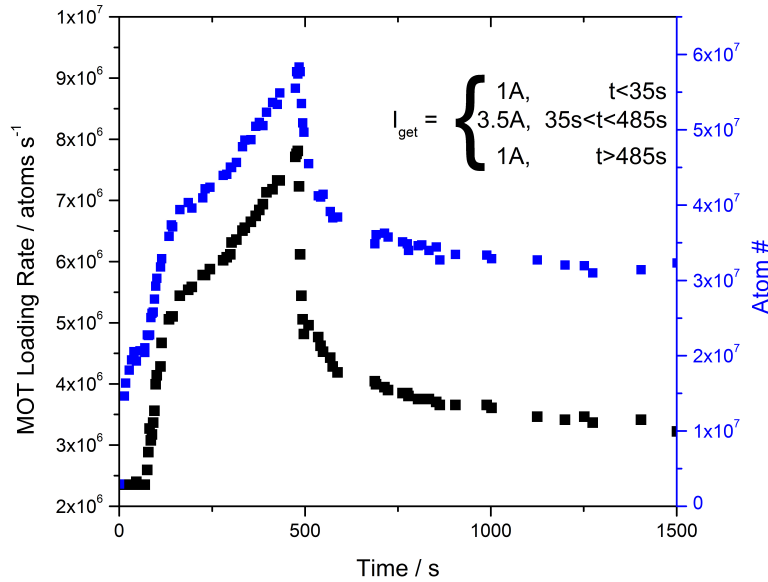**Figure 2.14:** *By increasing the dispenser current, the pressure increases more rapidly.*



**Figure 2.15:** *Pressure and number of atoms versus time for a 3.7A dispenser current. The number of atoms and the pressure increase with time in two ways: an initial exponentially decaying growth due to the dispenser flux and a linear growth due to temperature increase releasing rubidium from the chamber walls.*
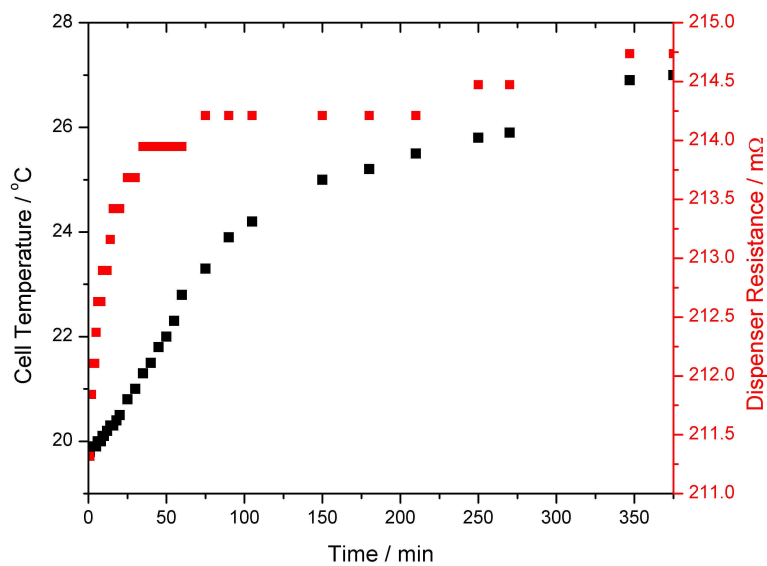
**Figure 2.16:** *The temperature of the dispenser, which is proportional to its resistance, increases over a shorter period of time than the chamber, which also increases in temperature.*
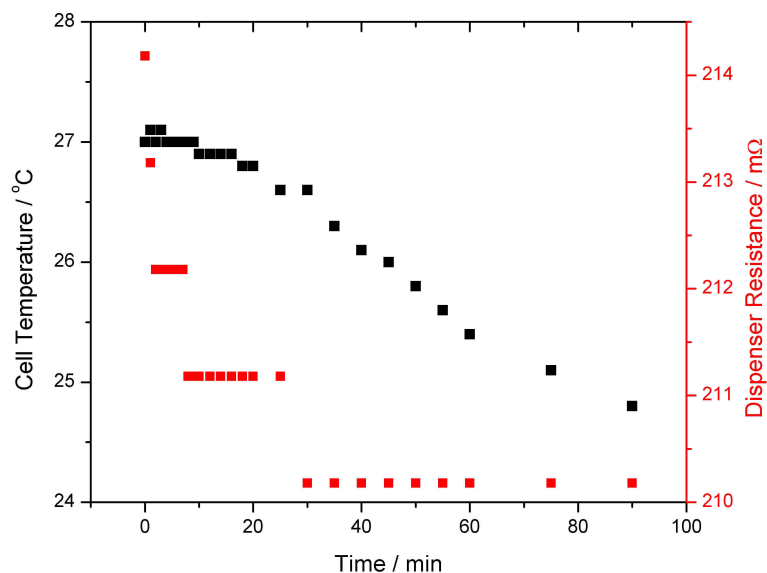


**Figure 2.17:** *The dispenser temperature decays rapidly to the original value, but the chamber temperature decays much more slowly.*

radiation from the dispenser, resulting in an increase of the atom flux from the walls. The pressure follows a similar trend to the number of trapped atoms when the dispenser is left on. We have measured the resistance of the dispenser as an indicator of temperature and also the temperature of the vacuum chamber, and see that the dispenser temperature (resistance) does indeed increase more quickly than the chamber (Figure 2.16).

Once the dispenser is switched off, the pressure and number of trapped atoms decay following a double-exponential. The first exponential has a time constant of approximately 7s, which corresponds to the fast switch off of the dispensers and the ion pump doing its job, whilst the second exponential has a much longer time constant around 400s, which we interpret as the walls of the vacuum chamber cooling down. The result is that even after an hour the pressure in the cell is higher than the initial pressure by about 50%. The temperature of the dispenser does indeed return to its original value rapidly (Figure 2.17), while the chamber temperature takes a much longer time to decay. The fast switch-off and the increased response with higher currents are the features of the dispenser that could make them useful as a pulsed atom source: if the dispenser can emit a large flux in a short time such that the walls of the chamber do not heat up, the dispenser could be used as a reliable pulsed atom source.

We now begin to characterise pulses at higher currents for shorter times to test the suitability of the technique for pre-loading an atom trap before evaporative cooling in a single chamber.

## 2.7.2 Individual Pulses of the Dispenser

When current is sent to the dispenser, there is an initial delay before any response is detected. We believe this is an initial heating of the dispenser to threshold. Once threshold has been achieved, the number of atoms in the MOT and the pressure increase rapidly, as shown in Figure 2.18, for a single 8A pulse from $t = 35 - 43.5$s. After the pulse, the number of trapped atoms and the pressure both decay back to the initial level, with the pressure decaying more quickly than the atom number. This appears promising for running a cold atom experiment: some of the trapped atoms could be held until the pressure decays to an acceptable level, before evaporative cooling begins.

We characterise single pulses for a variety of currents between 6A and 10A (Figure 2.19), finding that higher current pulses can give larger increases in the number of trapped atoms in shorter times. This is beneficial from the point of view of experimental repetition rate. However, we have discovered that higher current pulses can break the dispensers, so decide to be cautious in our next set of investigations, which tests a sequence of pulses for reproducibility.

## 2.7.3 Many Pulses

We test the reproducibility of the 8A dispenser pulses by running six pulses in a sequence, with 180s between each pulse. This timescale is long compared to many atomic physics experiments, and is an upper limit to what we would tolerate in
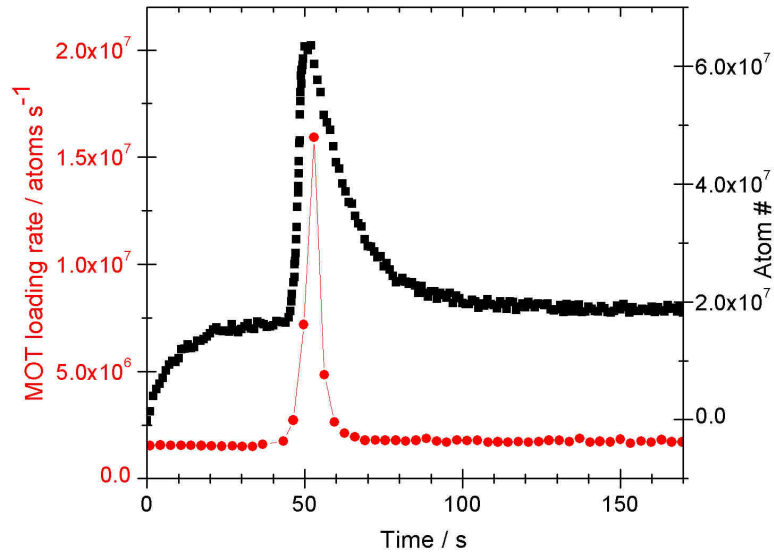
**Figure 2.18:** *The number of atoms and the pressure for a single 8A pulse lasting 8.5s.*
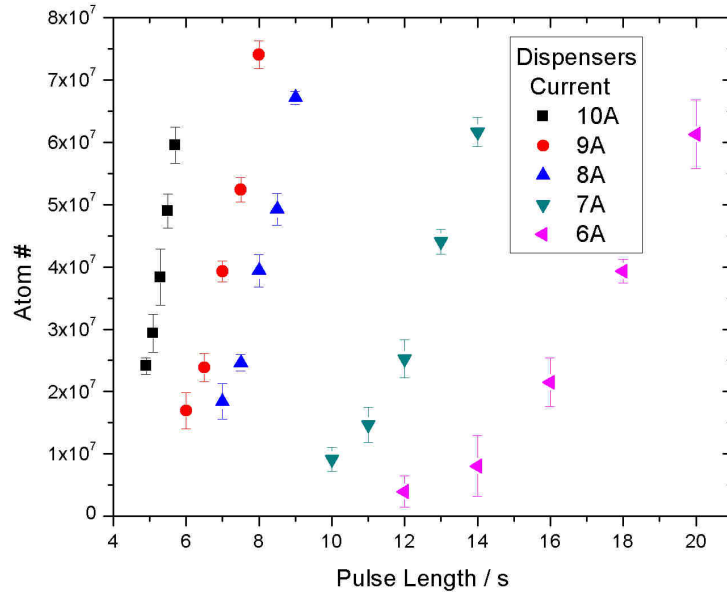


**Figure 2.19:** *The effect of various dispenser pulses on the number of trapped atoms.*

practice. We measure the pressure throughout the sequence, and the results are shown in Figure 2.20. The background pressure between pulses gradually builds to a value higher than the original background pressure, causing us to load MOTs 50% larger after the pulse sequence than before (Figure 2.21).
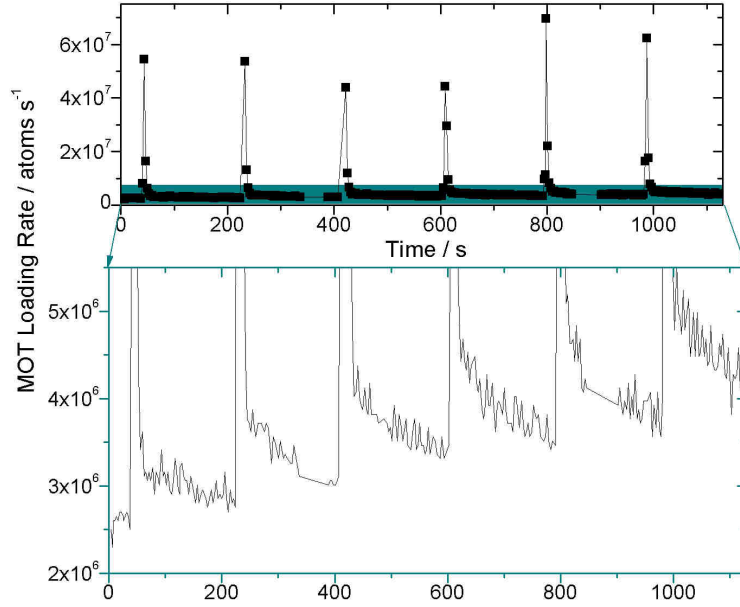


**Figure 2.20:** *Pressure versus time for 6 dispenser pulses lasting 8.5s at 8A, with 3 minutes between pulses. The pressure can be seen to rise during the sequence, which is not desirable for a reproducible atomic physics experiment.*

The atom number loaded during the pulses is also seen to rise, and most tellingly so does the voltage across the terminals of the dispenser feedthrough, which is proportional to resistance and thus temperature (Figure 2.22). We believe that this temperature rise is the limiting factor to the pulsed dispenser method, and is responsible for the rise in pressure that we observe. If the dispensers are hotter on subsequent pulses, the flux of rubidium leaving the dispenser will be greater. Without applying direct cooling to the dispenser feedthrough, we have been unable to circumvent this feature, and must therefore look for alternative methods to enable evaporative cooling. If the walls of the chamber are releasing lots of atoms under heating, there must clearly be a large atomic reservoir on the walls of the chamber anyway. We turn our attention to a method which can make use of this reservoir in a controllable and non-thermal way.
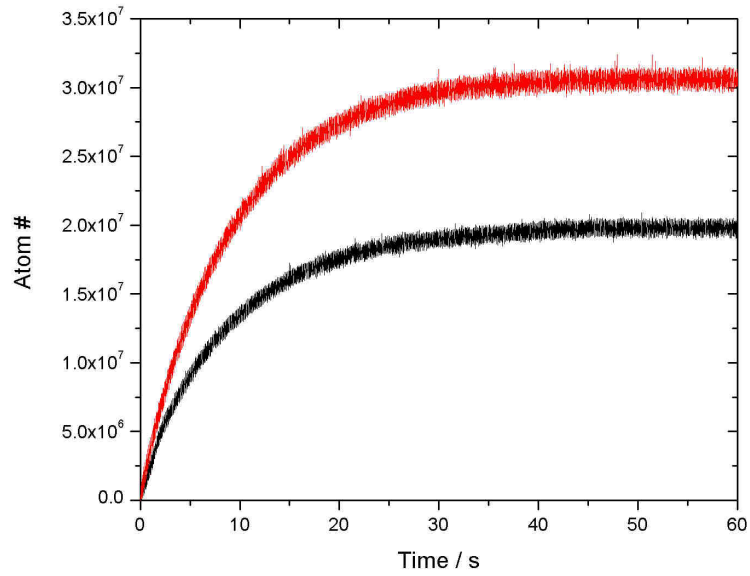
**Figure 2.21:** *The number of atoms trapped in the MOT before (black) and after (red) the pulse sequence of Figure 2.20.*
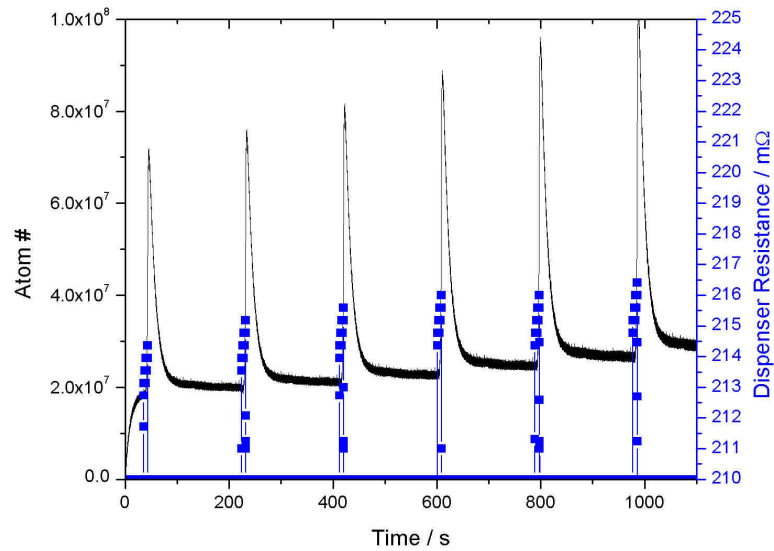


**Figure 2.22:** *The number of atoms and the temperature are found to rise during the pulse sequence. We believe the temperature rise is the reason for the pressure rise.*

## 2.8 Light-Induced Atomic Desorption

As gradual heating of the apparatus leads to an increased pressure over time during pulsed dispenser operation, we decided to investigate a non-thermal method of modulating the background pressure in time: Light-Induced Atomic Desorption (LIAD). By illuminating the inner surfaces of the vacuum chamber with UV light, atoms which are stuck to the surface can be desorbed. When the light is switched off the atoms should re-stick to the surface, quickly lowering the pressure in the MOT region.

We purchased two high power Surface Mounted Devices (SMDs) - arrays of twenty-five LEDs on a chip to investigate the dependence of MOT size and loading rate on light frequency and intensity. The SMDs (Enfis Uno Tag Array Blue and UVA) have a peak wavelength of 465nm and 375nm, and maximum output power of 5.5W and 0.6W respectively, which is controlled by the current supplied to the SMD. The SMDs are around 1cm by 1cm in size, and we mount them outside one of the vacuum chamber viewports which is specially coated to transmit UV light at a greater efficiency than standard viewports.

The high electrical powers (20W) of the SMDs cause a significant amount of heat to be generated during operation. Temperatures above 85°C can fatally damage the SMDs, so precautions have been taken to minimise the temperature increase of the arrays. We decide to mount the SMDs on a heatsink using thermally conductive glue. The temperature difference as a function of electrical power is given by

$$\Delta T = P \times (R_s + R_g + R_h), \tag{2.9}$$

where $R_s = 0.7$°C/W is the substrate thermal resistance, $R_g = 0.001$°C/W is the thermal resistance of the glue and $R_h$ is the thermal resistance of the heatsink. As we want $\Delta T < 65$°C, we choose a heatsink with a thermal resistance of 2.5°C/W.
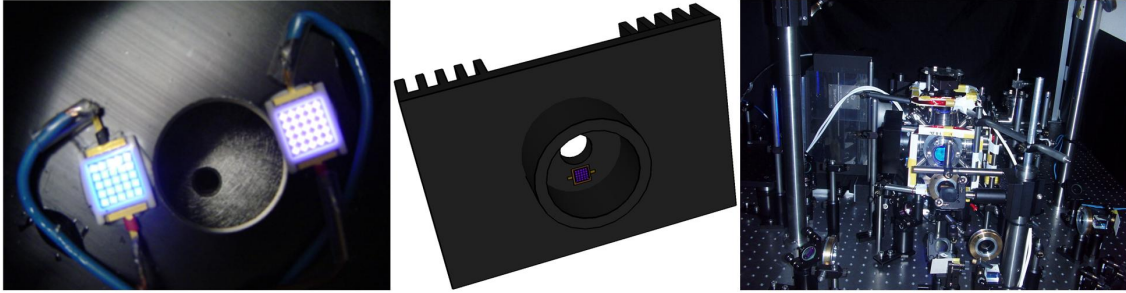


**Figure 2.23:** *(left) The Blue and UVA SMDs in low-power operation. (centre) The heatsink which keeps the SMD temperature low is also used to mount the SMDs to the vacuum chamber. The collar is placed around the flange of the vacuum chamber, and is held in place by screws. (right) The experimental apparatus during a LIAD experiment. The black heatsink can be seen at the left of the vacuum system.*

As the heatsink, which is 4cm × 5cm × 7cm, adds a large bulk to the SMDs, we decided to use it as the only support by which they are directed into the vacuum system by clamping it to one of the vacuum flanges. The final design for the heatsink and mount is shown in Figure 2.23. The hole in the middle of the heatsink retains

some optical access through the viewport while the SMDs are in use. The "collar" around the SMDs has small tapped holes through which screws steady the mount against the flange. Further small holes also allow the electrical connections to reach the power supply.

The LIAD effect in our stainless steel chamber proved to be disappointing (Figure 2.24). Loading an initial MOT of $1.75 \times 10^7$ atoms from background pressure, we turn on the SMDs at full power for 25s. The MOT loads an additional $6 \times 10^6$ atoms with UV light, and $3 \times 10^6$ atoms with Blue light. Although this demonstrates that LIAD does have an effect in our apparatus, this effect is not sufficiently large to aid us in our goal of trapping large numbers of atoms at low pressure.
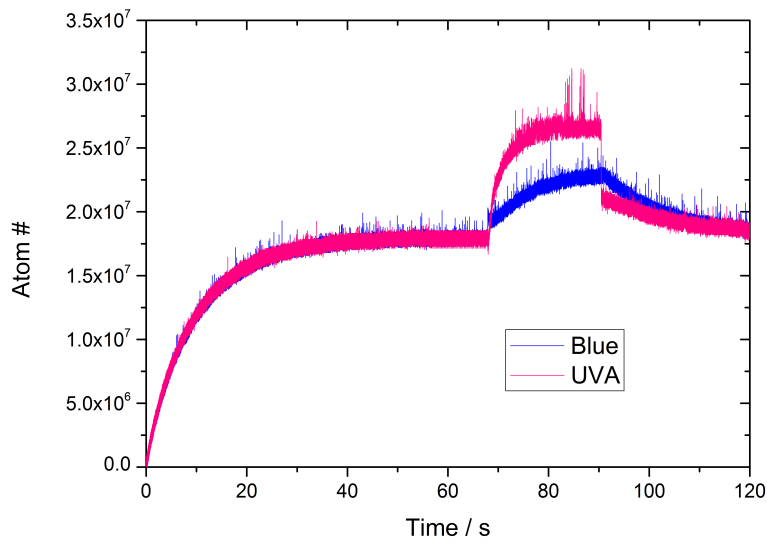


**Figure 2.24:** *Increased MOT loading with LIAD in a stainless steel chamber. By loading the MOT fully from base pressure, we trap $1.75 \times 10^7$ atoms. By turning on UVA (Blue) LEDs at $0.6\,W$ ($5.5\,W$), we increase this number of trapped atoms by $6(3)\times10^6$ atoms.*

## 2.9 Limitations of the Stainless Steel Apparatus

In addition to the rising pressure during pulsed loading with dispensers and the small LIAD effect in this system, we found that the design of the vacuum system caused problems with MOT alignment. Due to the size of the MOT beams relative to the viewports, we had no flexibility in the alignment of the off-horizontal beams, thus fixing the intersection of our MOT beams. Similarly, in order to use as low a current as possible for magnetic trapping, the MOT coils were placed close to the cell and wound around formers which surrounded the vacuum system flanges, allowing a limited movement of the coils.

As was indicated in Section 2.4, we found that, by varying the magnetic field gradient, the MOT would move within the vacuum system, as shown in Figure

2.25. We interpret this as poor alignment of the magnetic field null with the optical molasses. At high magnetic fields, the MOT forms closer to the magnetic field null, whilst at low fields it forms closer to the optical molasses. The fixed geometry imposed by the cell prevented us from moving the coils to compensate for this misalignment. Adding shim coils can compensate this alignment problem so that the MOT does form in the centre of the molasses region, but the use of shim coils for this purpose means that they cannot be used to ensure an homogeneous expansion of the gas during the molasses cooling stage.
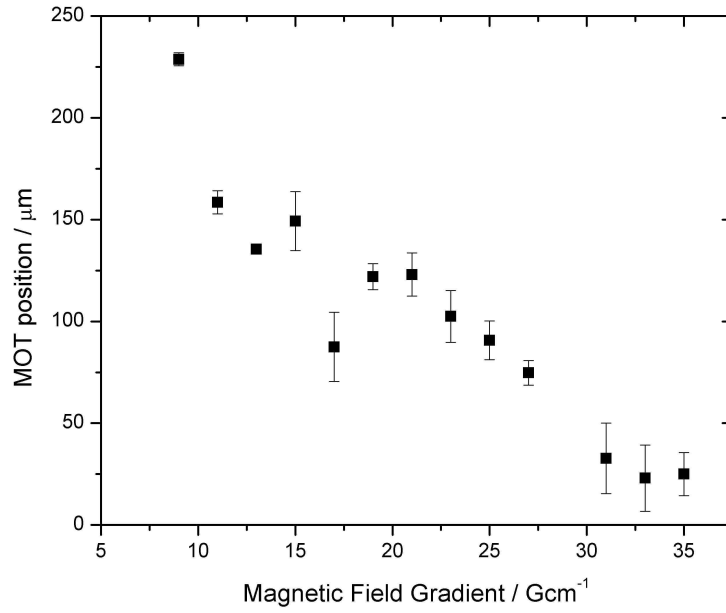


**Figure 2.25:** *By varying the MOT magnetic field gradient, the position of the trap can be made to vary. This indicates poor alignment between the optical and magnetic fields: at high magnetic field gradients the trap will form closer to the magnetic field null.*

The limitations in alignment and in keeping the background pressure low led us to design a new vacuum system which will improve the possibility of reaching quantum degeneracy in a single cell.

## 2.10   Summary and Prospects

We have built a single-chamber Magneto-Optical Trap which can regularly trap over $10^8$ $^{87}$Rb atoms. Although investigations of Light Induced Atomic Desorption were unsuccessful in loading large MOTs, the investigations with pulsed dispensers were more promising. Large MOTs can be loaded at a low background pressure, and if a method can be found to avoid rising chamber temperatures over many repetitions this technique may prove to allow evaporative cooling in a single chamber. For

example, one could try cooling regions of the chamber using a Peltier cooler, as in [133], while the authors of [134] have recently demonstrated a method to reduce this heat dissipation by using an electron beam to drive the dispenser. Furthermore, the lessons learned in the above investigations have helped to shape the design of a new experimental apparatus.

The apparatus will continue to be used to investigate dual-species trapping of either bosonic $^7$Li or fermionic $^6$Li with $^{87}$Rb, including measurements of inter-species collisional rates. The pulsed MOT loading techniques will also be attempted with the Lithium atoms, and if either prove to be successful in trapping large Lithium MOTs it will present a massive simplification over standard techniques of trapping these light elements, which commonly require bulky Zeeman slowers to load the MOT.

# Chapter 3

# Pulsed Loading of a Rubidium Magneto-Optical Trap in a Glass Vacuum System

## 3.1 Motivation for new apparatus

As previously discussed, evaporative cooling of cold atoms requires optimisation of an awkward constraint: maximising the number of atoms in the trap but minimising the background pressure to avoid unwanted collisions ejecting atoms from the trap. The investigations of pulsed loading of the MOT in the stainless steel system showed that the pulsed dispensers method successfully loaded the MOT in the desired way, with the disadvantage of lack of reproducibility due to increased pressure over many repetitions. Meanwhile, LIAD was shown to cause only a very small increase in the size of the MOT.

In order to aid the pumping of the system and stop the slow rise of pressure, we decided to build a new, smaller vacuum system. The small size of the apparatus would also be advantageous for the inclusion of magnetic trapping in this system: placing the coils as close as possible to the trapping region allows the use of lower currents to achieve the required magnetic fields, which will produce less heat and reduce the need for a complicated water-cooling system. As was demonstrated Section 2.9, the stainless steel vacuum system did not allow for flexible positioning of magnetic coils close to the trapping region, which we will overcome in the new apparatus.

We also decided to base this new trapping system around a glass cell, which gave us more optical access to the atoms. A further advantage of the pyrex cell is that the LIAD effect is more pronounced for atoms leaving glass surfaces than for atoms leaving metal surfaces, as was demonstrated originally in [90].

## 3.2 New Vacuum System

Following the constraints laid out in Section 3.1, we purchased a Pyrex glass cell (Starna Scientific UHV/PX/16x16x70/CF70.40) with a square cross section (side

length 2.4cm) as the centrepiece of our new apparatus. The rectangular part of the cell is 7.25cm long, and is connected to a 15.75cm glass-to-metal transition. This allowed us to mount magnetic coils within a few cm of the atoms, as well as complete freedom in the alignment of the coils and the laser beams.

We keep the volume of the system to a minimum in order to aid high-speed pressure variation. We connect the glass cell to a 40mm ConFlat four-way cross, the other flanges of which are connected to: a 40l/s Ion pump (Varian StarCell), identical dispenser feedthroughs to those used in the steel system, and an all-metal valve to allow the connection of the turbo pump for use during bakeout. A three dimensional sketch of the vacuum system is shown in Figure 3.1. The dispensers are mounted 27cm away from the MOT trapping region. An added advantage of this vacuum system is that it can be removed (e.g. to replace dispensers and bakeout) from between its magnetic coils without disturbing any coils or optical alignment.
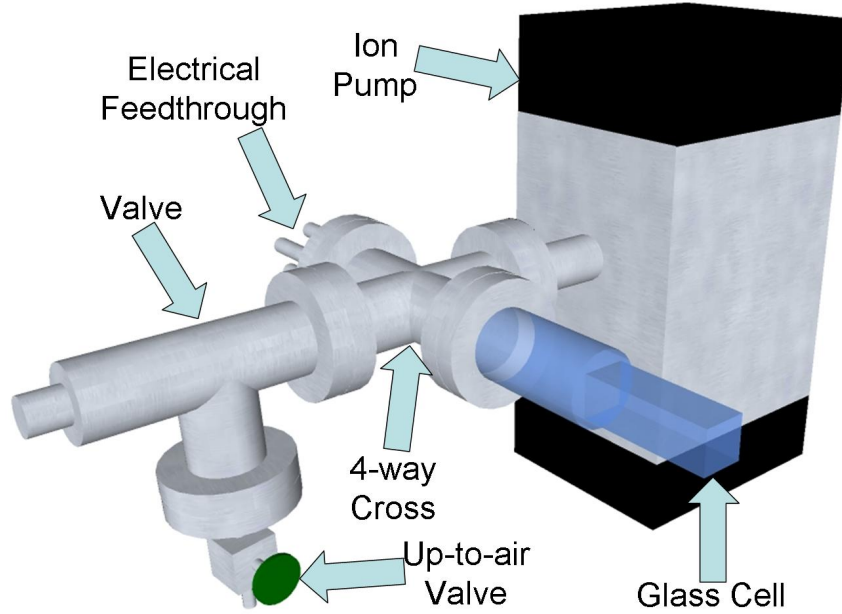


**Figure 3.1:** *The vacuum system based on a glass cell.*

Cleaning and bakeout is carried out in a similar way to the stainless steel system, although the compact nature of the new vacuum system allows us to place the whole vacuum apparatus in a home-made aluminium oven which is connected to ceramic heaters. In order to improve the energy-efficiency of the oven, we insulate the outside using rolls of glass fibre and aluminium foil, which are held in place with high-temperature Kapton tape. The currents to the heaters are individually controlled by variable transformers, and thermocouples inside the oven allow us to modify each heater to ensure uniform temperature inside the oven. We limit the baking temperature of this apparatus to 220°C in order to avoid damaging the glass-to-metal transition, which should not be exposed to temperatures above 240°C due to the different thermal expansion coefficients. To help limit temperature gradients across the glass, we enclose it in a brass cylinder during bakeout. Dispensers are degassed in the same fashion as in Section 2.2.

If this single-cell system does not provide the required results, we have designed it in such a way that it can be quickly integrated into a two-chamber differential vacuum by removing the dispensers and attaching it via a differential to a stainless steel cylindrical octagon chamber (Kimball MCF600-SO200800). The glass cell would then provide the low pressure science chamber, while the octagon would provide pre-cooled atoms. The large glass area of the octagon should enable LIAD to be used in this system if necessary.
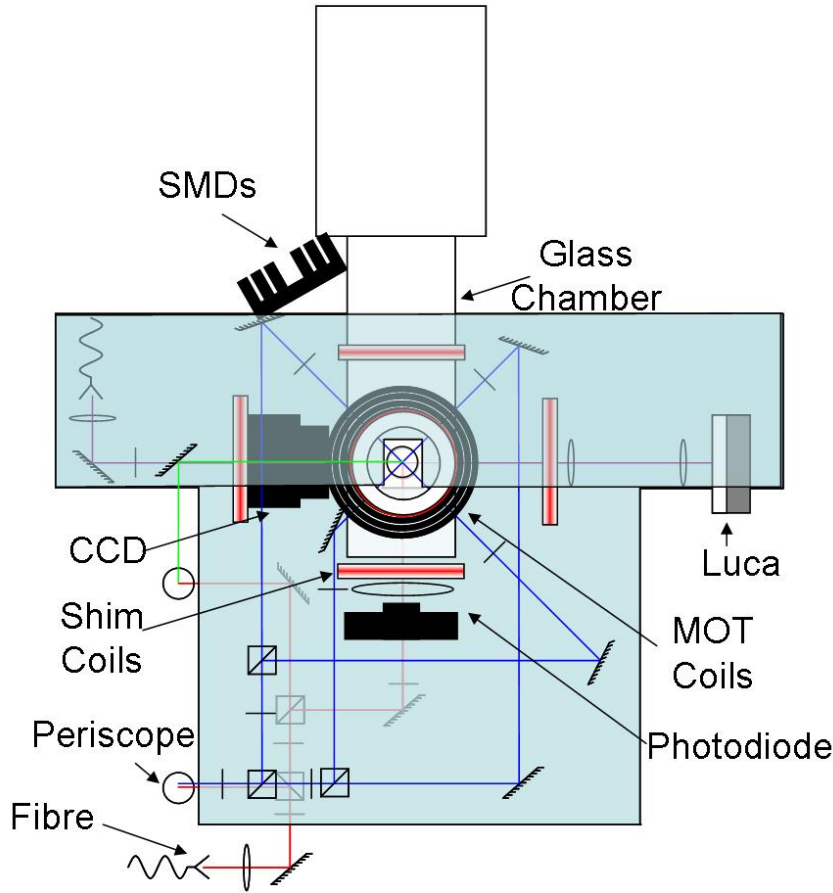
## 3.3  Optics



**Figure 3.2:** *Layout of optical components and magnetic components for the achievement and observation of a Magneto-Optical Trap of rubidium in the glass chamber. The optics are arranged on three levels: red beams denote the lowest level, blue beams the middle level and green beams the highest level. Purple beams show the imaging and optical pumping beams.*

We again operate a six-beam MOT, with a peak power of 4.2mW per beam. We use the existing laser setup from Chapter 2 on the first optical table, but add an additional $\frac{\lambda}{2}$ waveplate and PBS to divert the cooling and repumper light to a new single-mode, polarization maintaining optical fibre which delivers the light to

the other end of the second optical table, giving us up to 50mW of cooling light and 6mW of repumper. This combined beam is collimated using an $f = 75$mm achromatic doublet lens to a $\frac{1}{e^2}$ waist of 7.5mm.

On the second optical table, the beams are split using PBSs and $\frac{\lambda}{2}$ waveplates and sent to three horizontal tiers: the bottom tier houses a beam which is directed vertically upwards through the glass cell; the middle tier supports two orthogonal pairs of counter-propagating beams which are directed horizontally through the glass cell, and the top tier provides a downward beam which is overlapped to the upward one from the bottom tier. The schematic of this layout is Figure 3.2.

A photodiode and $f = 40$mm lens are placed at the end of the glass cell to collect fluorescence from the MOT, which is used to count the number of atoms as in Section 2.6.1, and a CCD camera is used to monitor the MOT.

Alignment of the beams is carried out by overlapping the beams in each pair on the mirrors before the cell. Fine alignment is easier in this apparatus than the steel chamber, as one can see the MOT and fluorescence directly using an infrared monocular. We adjust the beams so that the MOT forms perfectly in the centre of all beams.

## 3.4 Magnetic Fields

In this experiment, we plan to use a pair of anti-Helmholtz coils to provide the gradient in the MOT and to magnetically confine the atoms after an optical molasses stage in a quadrupole magnetic trap.
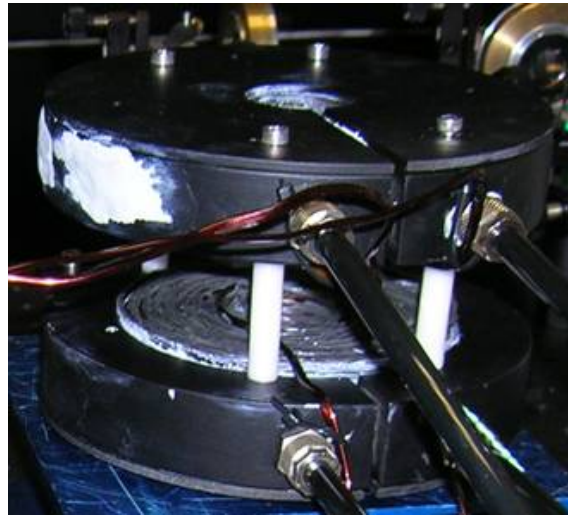


**Figure 3.3:** *The new coils can be seen inside their black mounts. The black tubes carry the water from the refrigerator to cool the coils during high-current operation.*

We use 3.04mm × 1.52mm rectangular cross-section copper wire, as it is easier to wind in a controllable fashion than that with round cross-section. We want to use the same power supply as we used for the MOT coils in the previous setup, so the maximum current is restricted to 20A. As the coils have to fit outside the glass

cell, we fix the separation to be 36mm, and we decided to wind them in such a way that we can direct a pair of MOT beams through the axis. We thus decided to wind them with a 30mm hole in the middle. Using the Biot-Savart law, and the resistance of the wire (0.0045 $\Omega$ m$^{-1}$), we estimate that by having a central radius of 15mm and 8 turns per layer to give 160 turns total and a total length of 32m of wire per coil, we can generate 220 G cm$^{-1}$ with a current of 18.5A, at which we will dissipate 49W.

We wind these coils around a home-made drum which we cover in grease so that it can be removed to leave mount-free formed coils, and use Araldite glue (which can withstand temperatures up to 120°C) to hold the windings together. During winding, we find that we lose a fraction of a turn per layer; we end up with 7.4 turns per layer. We therefore wind 20 layers to give 148 turns, which have a resistance of 0.28 $\Omega$ (measured), and thus 112W of power dissipation at 20A operation. The inductance of the coils is calculated using $L = \pi\mu_0 N^2 r^2/l$ (where $l$ is the depth of the coils) to be 0.9mH, which gives a natural switching time $\tau = L/R$ of 3ms.

The high power dissipation means we need to worry about overheating and damaging the coils. We place a thermocouple inside the coils to allow us to monitor the temperature, and mount the coils in a water cooling system. The coil mounts contain channels through which water may flow and are connected in a closed-circuit to a refrigerated water cooler. We design this mount to be cylindrical, but with a cut through one section of the circumference in order to prevent eddy currents.

The fact that the coils are free to move relative to the vacuum system is useful when we calibrate the coils. We place a Gauss meter on a translation stage and measure the axial magnetic field component at various positions between the coils for a number of driving currents, in order to extract the magnetic field gradient. Using this we find that the magnetic field gradient is 10.4 G cm$^{-1}$ per ampere of current, which will give us a maximum gradient of 208 G cm$^{-1}$. This can be used with the LabView computer control program, rather than just extrapolating the magnetic field gradient from the Biot-Savart equation as we had to in the steel chamber.

The setup can be quickly adapted to allow evaporative cooling to quantum degeneracy in a purely magnetic trap by the addition of a third magnetic coil perpendicular to the two existing ones in the Quasi-Ioffe-Configuration (QUIC) trap [135]. The third coil adds an additional magnetic field component, raising the bottom to a non-zero value to prevent Majorana losses.

We have also built similar square shim coils to those introduced in the old system to counteract background magnetic fields. Whilst these are adequate in the horizontal plane, the shim coils for the vertical direction have to be placed farther away (90mm separation) due to the MOT coils, so we use 79mm radius circular coils with 30 turns, which give 3.1 G A$^{-1}$ in the MOT region.

## 3.5 Observation of a new MOT

By running the dispensers at 3.5A continuously, we observe a MOT of $1.2 \times 10^8$ with a loading time of 4.2s, which is optimized for a magnetic field gradient of 18 G cm$^{-1}$ and a detuning of -13 MHz (Figure 3.4). While these figures for the MOT

are satisfactory, the loading time is very short for starting evaporative cooling. We therefore try to use our pulsed techniques to achieve large MOTs at lower pressure. To avoid the thermal effects of pulsed dispensers, we investigate the suitability of the LIAD effect to give us a starting point for evaporative cooling.
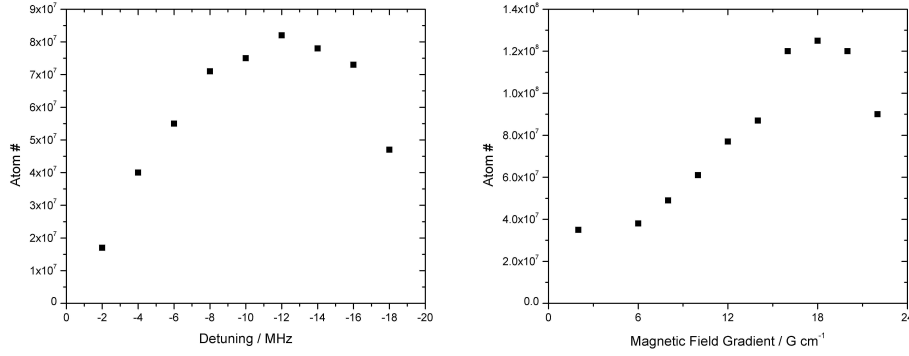


**Figure 3.4:** *(left) The number of trapped atoms is investigated as a function of detuning, at a constant magnetic field gradient of 13 G cm$^{-1}$. (right) By varying the magnetic field gradient at the optimal detuning, we further optimize the MOT.*

## 3.6   Light-Induced Atomic Desorption

The work presented in the remainder of this Chapter was carried out in close collaboration with Lara Torralbo-Campo: in particular, the data presented in Figures 3.7, 3.8, 3.9 and 3.13 are also presented in Lara's thesis [130].

To load the MOT with a switchable burst of atoms from the chamber walls, we use SMDs which can output 5.1W in the violet (405nm) and new, increased power ultraviolet (1.2 W at 375nm) SMDs. (When we began our investigation in the new apparatus the Blue SMD was irreparably damaged due to air pockets in the thermal-glue causing poor heatsinking.)

We control the SMDs with LabView to allow automated data acquisition, and switch the SMDs on by switching the current from below threshold ($I < 0.01$A) to the desired current. The SMDs still emit light at subthreshold currents, but we measure that this light has no effect on MOT loading, as shown in Figure 3.5.

As we believe the critical parameters in LIAD are wavelength and intensity, we firstly calibrate the output intensity in the cell as a function of current empirically. Unlike the special viewport in the stainless steel apparatus (Section 2.8), the walls of our glass cell are not coated for use with UV light, so we measure the extinction due to the glass walls.

The SMDs are mounted on an identical heatsink to their predecessors, and positioned to the rear of the chamber as shown in Figure 3.2 in order to illuminate the largest possible area. The light power is measured before and after the glass
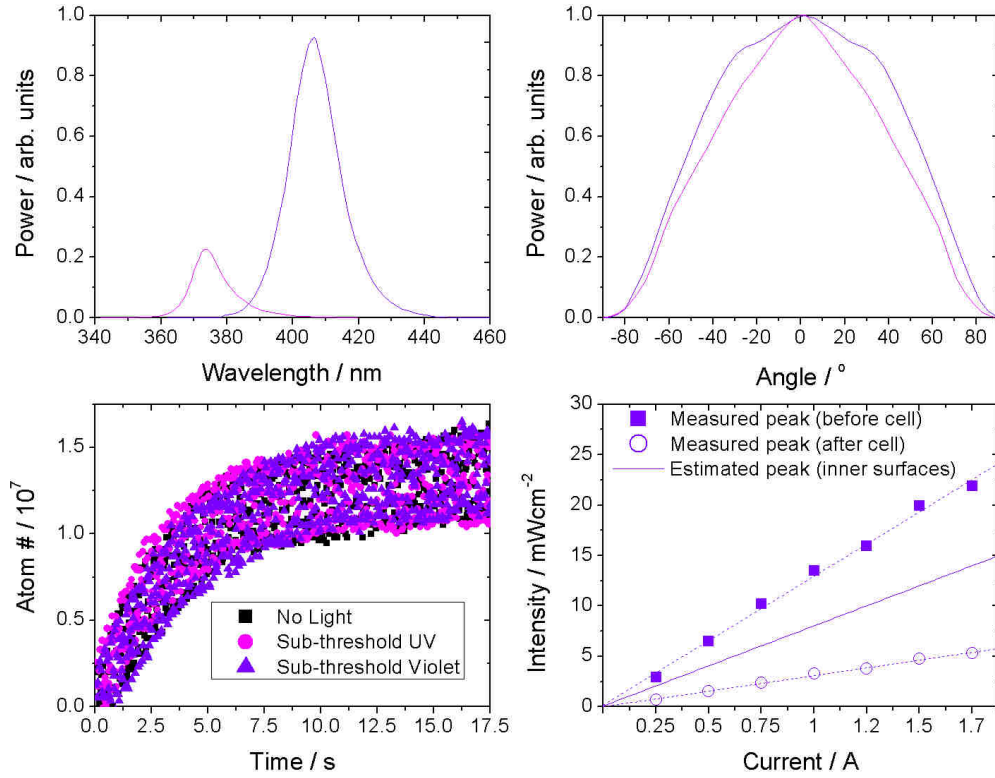
**Figure 3.5:** *(top) The output wavelengths and illumination angles for the UV SMDs (shown in pink) and the Violet SMDs (shown in violet), as supplied by ENFIS. (bottom left) We control the SMD output using LabView by varying the drive current about the threshold point. To validate this approach, we verify that the sub-threshold illumination causes no measurable effect on the MOT. (bottom right) We empirically measure the intensity output of the SMDs as a function of current by measuring the power before and after the cell. The average of these two values approximately gives the intensity on the internal surfaces of the cell.*

cell for a variety of currents. The change in intensity over a distance of 2.5cm at an initial distance of 7.5cm is negligible. As the two walls of the cell are made of the same material we safely assume that the average of the intensity before and after the walls is the intensity on each of the two surfaces. For simplicity, we ignore the illumination of the top and bottom surfaces of the cell.

### 3.6.1 Increased Atom Number and Pressure from Individual Light Pulses

We initially measure the effect of LIAD on the MOT loading in terms of increased atom number in the MOT. To do this, we firstly load the MOT in the presence of only sub-threshold SMD light until it has reached an equilibrium atom number, before switching the SMDs to the desired current. The SMDs remain on until the atom number reaches a new equilibrium value, before being switched off. The data acquisition ends when the number of atoms in the MOT has returned to the original equilibrium value.

An example of the variation of atom number during the sequence is shown in Figure 3.6. When the SMDs are switched on, the number of trapped atoms increases quickly to a new equilibrium in around 15s. Once the SMD is switched off, the atom number decays at a slower rate, taking around 2 minutes to return to the original equilibrium value. We vary the illuminating intensity of each colour of light and find that the maximum number of atoms trapped during LIAD increases with the intensity (Figure 3.7). Unlike previous studies of the LIAD effect, we do not see a pronounced dependence on the wavelength of the illuminating light. This may be due to the broad frequency-spectrum of the SMDs. The fact that the violet SMDs offer almost 5 times the optical power, and that the atomic yield seems to saturate at the highest violet intensities, mean that the remainder of the experiments in this chapter were performed using only the violet SMDs.

An example of the pressure measurement and atom number for a single violet pulse of 14 mW cm$^{-2}$ is shown in Figure 3.6. This data also highlights the approach one will use to achieve Bose-Einstein condensation in our experiment: the pressure is found to drop at a quicker rate after the SMD is switched off than the rate at which the MOT loses atoms. Therefore an optimal value of the number of atoms in the MOT divided by the pressure can be used to set the loading of a magnetic trap, before evaporative cooling can begin.

### 3.6.2 Many Pulses

The limitation of the pulsed dispensers method discussed in Chapter 2 was not apparent until we attempted to load a sequence of MOTs using the pulsed technique: the background pressure in the chamber gradually increased over many pulses of the dispenser. Our hypothesis that a rising temperature is to blame for this rising pressure suggests that we should not see this effect using LIAD.

By applying a sequence of 10 pulses of 8 mW cm$^{-2}$ violet light (25s pulse duration with a 160s gap), we find that the background pressure between pulses actually decreases over time (Figure 3.8). This effect is verified by measuring the number of
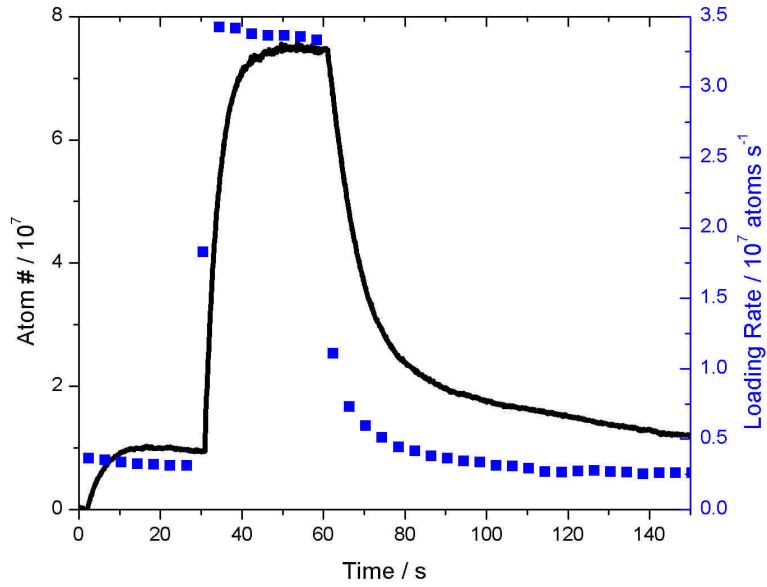
**Figure 3.6:** *The trapped-atom number and pressure evolution during a single 14 mW cm$^{-2}$ violet pulse. The pressure can be seen to decay more quickly than the number of atoms trapped in the MOT, which will allow an optimal delay between the end of the pulse and the loading of the magnetic trap to be found.*
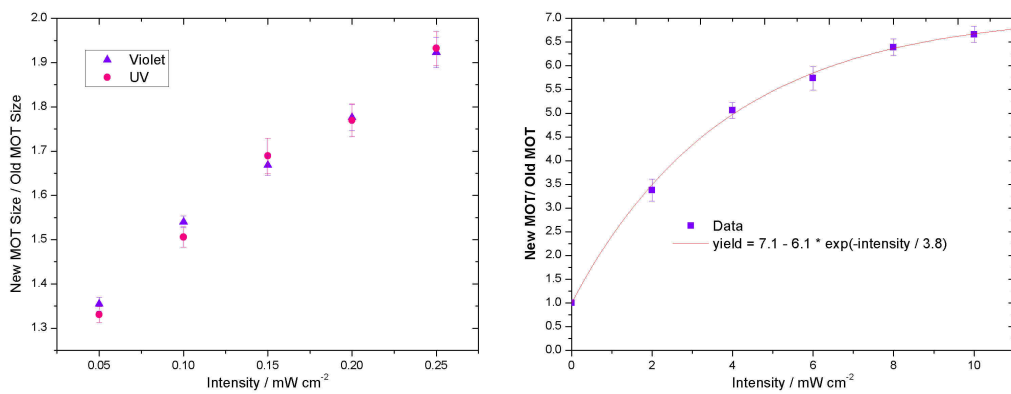


**Figure 3.7:** *(left) At low intensities, the increased MOT size due to LIAD is the same for both wavelengths of light. (right) The yield increases with the intensity of violet light with an exponential decay dependence.*

atoms trapped in the MOT in the absence of LIAD before and after the sequence: we see a 45% decrease in the number of trapped atoms. We investigate whether this is a result of the ion pump depleting the rubidium content of the chamber as no new rubidium is added, or is a result of the LIAD lowering the local rubidium density of the walls of the chamber: "cleaning" the illuminated portions of the chamber and moving the rubidium to "dark" regions of the cell.

We load a "normal" MOT, then measure the pressure in the system over half an hour, finding no significant change. We then load another MOT, and find negligible difference from the first one. Thus, there appears to be no decay due to the pump.

The pressure drop is no more desirable than the increase due to pulsed dispensers. To use the technique in a Bose–Einstein condensate apparatus, we need every experimental cycle to be identical.
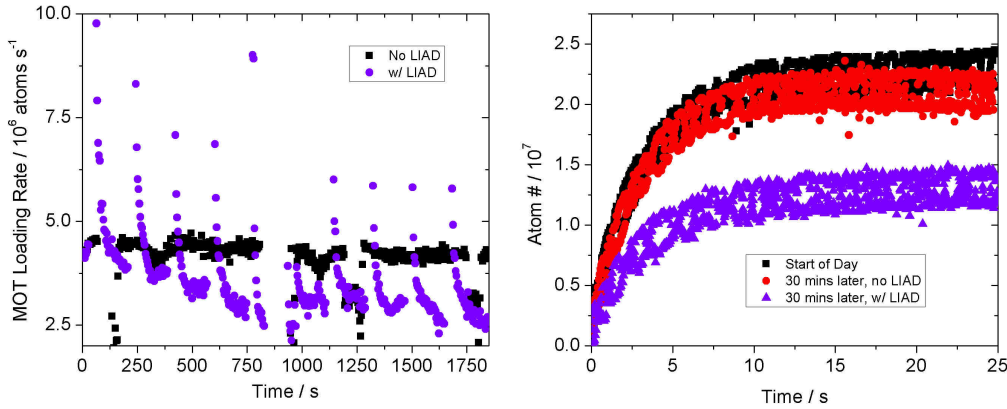


**Figure 3.8:** *A sequence of pulses of violet light at $8\ mW\ cm^{-2}$ causes the background pressure to fall much faster than the case without violet light, showing that the reduction is not due to the pumps alone. This pressure drop can also be seen in the number of atoms loaded into the MOT from background pressure alone.*

### 3.6.3   Compensating the Pressure Drop

To aid reproducibility, we try to eliminate this pressure drop by turning on the dispenser at a low value. We firstly run the dispensers at the minimum current for which we see pressure increasing (3A). However, this over-compensates for the LIAD effect and causes the pressure to rise after a number of pulses, so we run the dispensers at 2.5A and can stop the pressure decrease in a "plateau" region after an initial drop. The "plateau" region lasts for several hours until the LIAD pulses stop, as shown in Figure 3.9.

We measure the number of atoms trapped in the MOT in the plateau region to be $8 \times 10^7$. Although this is a smaller number of atoms than in the constant background pressure case, the variable background pressure will allow us to proceed
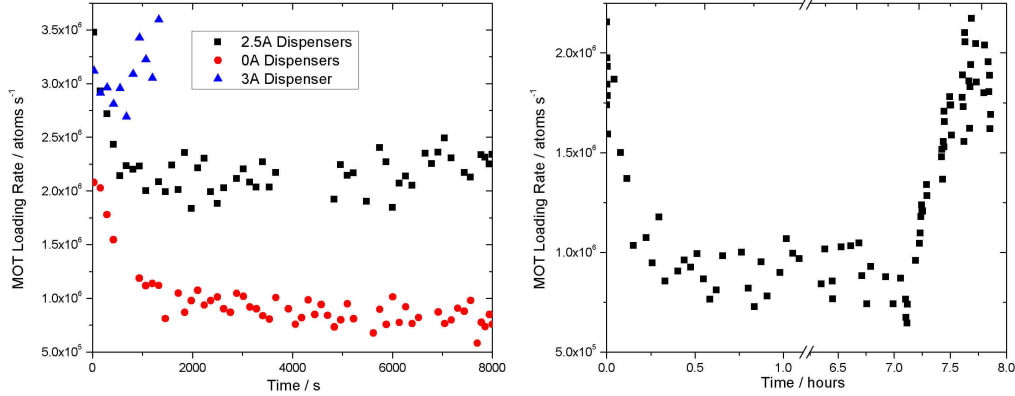
**Figure 3.9:** *By running the dispenser at 0A and the LIAD at 8 mW cm$^{-2}$, we see the pressure decay over hours. If the dispenser is run at 3A, the pressure grows. However if we run the dispenser at 2.5A, we can stabilise the pressure drop. This stabilisation lasts many hours, until the SMDs stop pulsing. At this point, the effect of the dispenser is to increase the pressure.*

to evaporative cooling of cold atoms in a single cell. The investigations in Section 4.14 into a new, efficient method of BEC give hope that this pulsed technique will allow the achievement of Bose–Einstein condensation in this simple apparatus. To demonstrate the worth of the LIAD effect, we will load a magnetic trap after the MOT phase and measure the decay of the atoms from the trap due to collisions with background gas. To measure this, we first need to be able to measure atoms in the magnetic trap.

## 3.7 Absorption Imaging of Cold Atoms

To provide an easy way of extracting the temperature, density and the number of trapped atoms, we use the absorption imaging technique.

A circularly polarized laser beam (0.15mW with $1/e^2$ radius of 4mm, giving us 36% of $I_{sat}$) resonant with the F= 2 $\longrightarrow$ F$'$ = 3 atomic transition is directed through the atomic cloud and collected by our Luca CCD camera (1004 $\times$ 1002 8$\mu$m $\times$8$\mu$m pixels), as shown in Figure 3.2. We apply a $\sim$ 1G bias field using the shim coils which are coaxial with the probe beam to provide a quantisation axis such that the circular polarization is well-defined. The atoms absorb and re-radiate the light so that a shadow of the cloud is imprinted on the beam, and this shadow is imaged on the camera using a pair of $f = 75$mm achromatic doublet lenses.

The absorption of the radiation as it propagates along the $z$-direction is described by Lambert's law

$$I_{out} = I_{in} \exp\left(-\sigma_0 \int_{z_{min}}^{z_{max}} \rho(x,y,z)\,\mathrm{d}z\right), \tag{3.1}$$

where $\rho(x,y,z)$ is the density of the cloud and the absorption cross section is given by

$$\sigma_0 = 3\lambda^2/(2\pi), \tag{3.2}$$

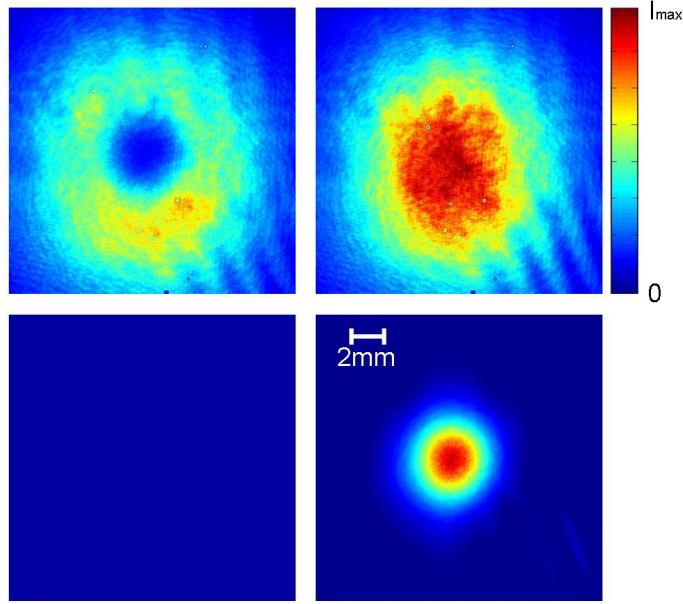assuming low saturation, where $\sigma_0$ is the cross section for resonant absorption.



**Figure 3.10:** *To obtain an absorption image of the atoms, three images are taken which correspond to the colour bar on the right: probe beam with atoms (top-left), probe beam without atoms (top-right) and darkground (bottom-left). The distribution of the atoms (bottom-right) is extracted by subtracting the darkground from both of the other images and dividing the atom image by the background image.*

If the opacity (reduction in the intensity of the probe beam due to the optical density) of the cloud can be measured, we can extract the two-dimensional number density or absorption profile of the cloud.

To remove the background light from the picture of the cloud one acquires three images as shown in Figure 3.10. Firstly, the probe beam is fired through the atoms and onto the CCD for $50\mu$s (controlled by the imaging AOM); all the light unabsorbed by the atoms ($I_A$) is recorded. A second image containing the probe beam in the absence of atoms ($I_B$) and a third acquisition without probe or atoms records the background light ($I_D$). These images are acquired 81ms apart, due to the limited 12.4 images per second acquisition rate of our camera.

The opacity of the medium is $(I_B - I_D)/(I_A - I_D)$, and the optical density is

$$D(x,y) = \ln\left(\frac{I_B - I_D}{I_A - I_D}\right), \tag{3.3}$$

giving the spatial density of the atoms, as shown in Figure 3.10. By integrating the two-dimensional density profile obtained in the absorption image over the x and y directions, we can extract the number of trapped atoms.

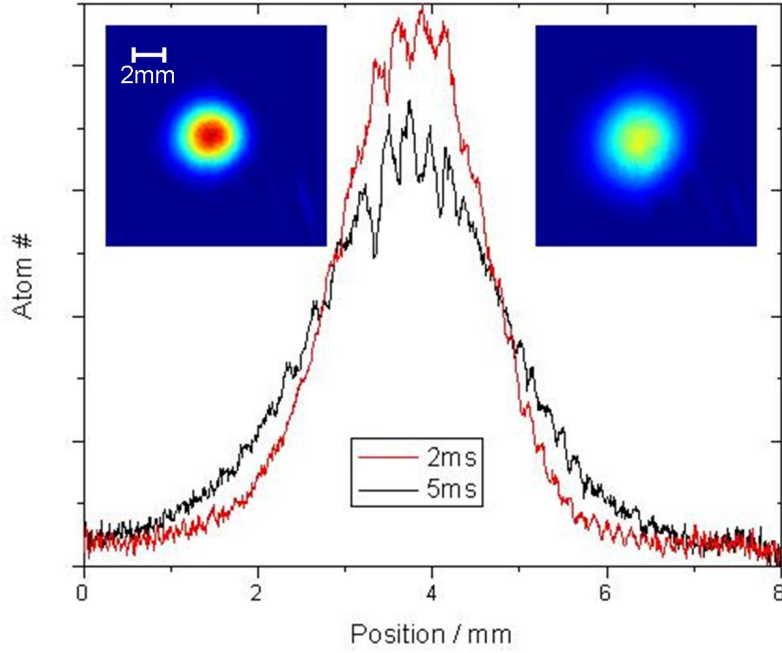$$N = \frac{1}{\sigma_0} \int \int D(x, y) \, \mathrm{d}x \mathrm{d}y. \tag{3.4}$$



**Figure 3.11:** *The temperature of the trapped atoms is obtained by taking images of the atoms at a controllable delay after releasing them from the trap. The positions of the atoms are recorded using absorption imaging, and the width of the Gaussian distribution extracted. The expansion of the cloud can clearly be seen.*

The pictures of the cloud can also be used to obtain the temperature of the gas experimentally, the atoms are released from the confining potential and allowed to expand freely for a pre-determined time of flight (typically a few ms), before being absorptively imaged. The effect of this is to map the momentum-distribution of the atoms into position-space.

Neglecting the effects of interactions, the expansion is given by a convolution of the initial position distribution $n_{\vec{r}}$ and the velocity distribution $\rho_{\vec{v}}$. The density at position $\vec{r}$ at time $t$ is given by

$$\rho_{\vec{r}}(\vec{r}, t) = \int \rho_{\vec{r}}(\vec{r} - \vec{v}t, t = 0) \, \rho_{\vec{v}}(\vec{v}) \, \mathrm{d}\vec{v}, \tag{3.5}$$

where each atom has moved by $\vec{v}t$.

The spatial distribution $\rho_{\vec{r}}$ and velocity distribution $\rho_{\vec{v}}$ of atoms in a harmonic

trap are, under normal conditions, approximately given by a Gaussian distribution

$$
\begin{aligned}
\rho\left(\vec{r}, \vec{v}\right) \;=\; & \frac{1}{(2\pi)^3} \frac{1}{\sigma_x \sigma_y \sigma_z} \frac{1}{\sigma_{v_x} \sigma_{v_y} \sigma_{v_z}} \\
& \times\; \exp\left(-\frac{x^2}{2\sigma_x^2}\right) \exp\left(-\frac{y^2}{2\sigma_y^2}\right) \exp\left(-\frac{z^2}{2\sigma_z^2}\right) \\
& \times\; \exp\left(-\frac{v_x^2}{2\sigma_{v_x}^2}\right) \exp\left(-\frac{v_y^2}{2\sigma_{v_y}^2}\right) \exp\left(-\frac{v_z^2}{2\sigma_{v_z}^2}\right).
\end{aligned} \tag{3.6}
$$

Assuming the distribution is separable in terms of the three location coordinates, the result is the one-dimensional spatial distribution $\rho_x\left(x, t\right)$

$$
\rho_x\left(\vec{x}, t\right) \propto \int \exp\left(-\frac{(x - v_x t)^2}{2\sigma_x^2}\right) \exp\left(-\frac{(v_x)^2}{2\sigma_v^2}\right) \mathrm{d}v_x. \tag{3.7}
$$

The resultant convolution is a Gaussian of width $\sigma_x\left(t\right)$

$$
n_x\left(\vec{x}, t\right) = \frac{1}{\sqrt{2\pi}\sigma_x\left(t\right)} \exp\left(-\frac{x^2}{2\sigma_x\left(t\right)^2}\right), \tag{3.8}
$$

with

$$
\sigma_x\left(t\right)^2 = \sigma_x\left(t = 0\right)^2 + \left(\sigma_v t\right)^2. \tag{3.9}
$$

By fitting this function to the density profile after the time of flight, one obtains $\sigma_x\left(t\right)$. Figure 3.11 shows images of the expanding MOT and cuts through the atomic distributions.

Repeated measurements for different times of flight $t$ give the size of the cloud as a function of time; this evolution can be fit by (3.9) to extract the initial spatial distribution and velocity distribution of the cloud.

If the velocity widths are identical $\sigma_v = \sigma_{v_x} = \sigma_{v_y} = \sigma_{v_z}$ the temperature of the atomic gas is given by $m\sigma_v^2 = k_B T$. Using this method we find the MOT temperature to be $254 \pm 36\mu\mathrm{K}$.

## 3.8   Cooling Toward Quantum Degeneracy

To reach quantum degeneracy, a number of stages are required - pre-cooling and trapping in the MOT, an optical molasses cooling stage, optical pumping and loading of a magnetic trap for partial evaporative cooling before transfer to an optical trap in preparation for further evaporative cooling. To do this, 11 separate devices are dynamically controlled using LabView: a schematic of the sequence (neglecting device delays) is shown in Figure 3.12. The following sections detail the evolution of the atom cloud during this procedure.

For the work reported in this thesis, we have progressed as far as loading atoms in the magnetic trap, so as to characterise the benefit of the LIAD effects.

Using the dispensers in continuous mode, we load $1 \times 10^8$ atoms into the MOT. To measure the MOT temperature, we turn off the optical and magnetic fields and
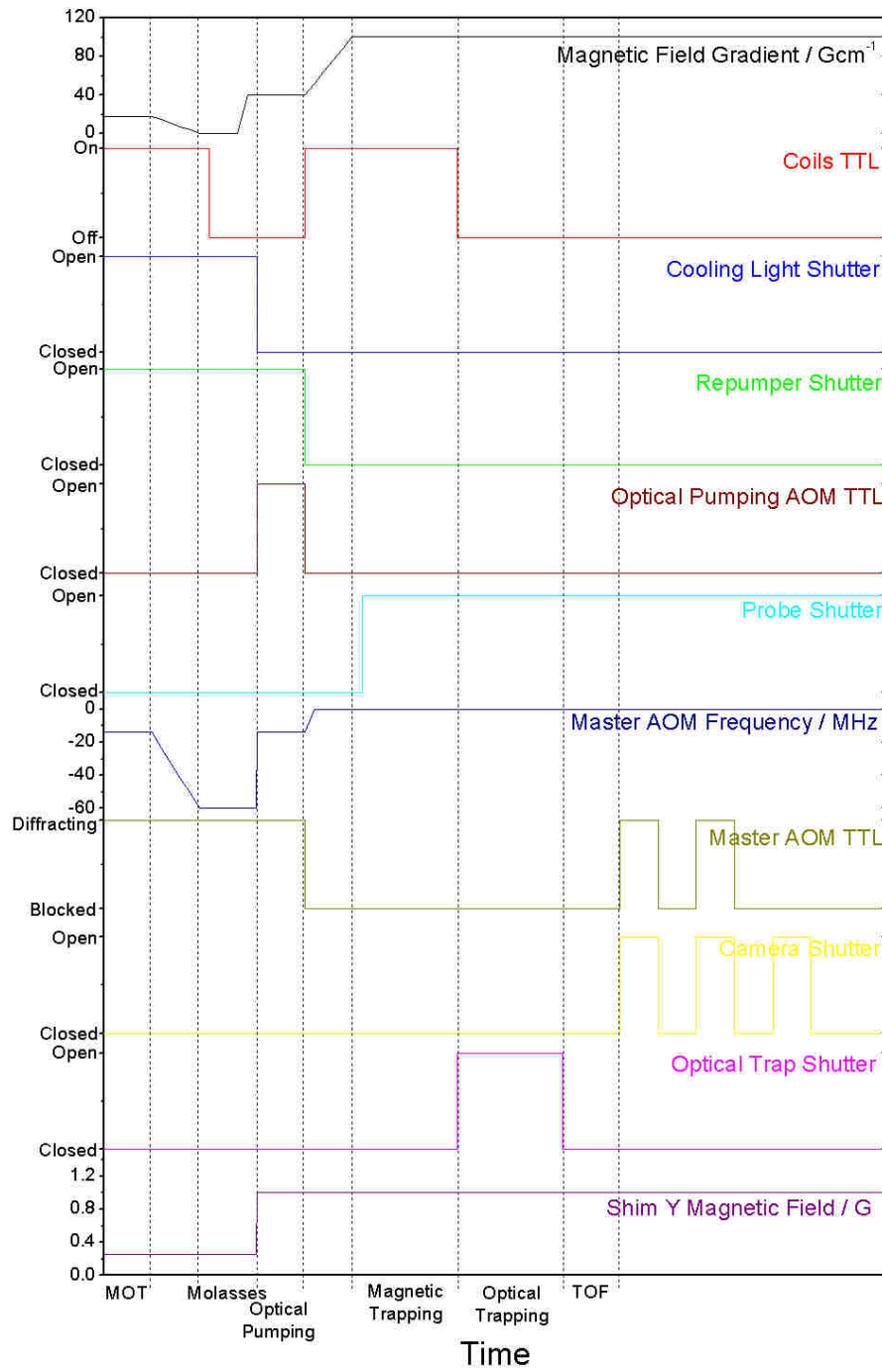
**Figure 3.12:** *Device timings for cooling the gas from MOT toward quantum degeneracy. Eleven separate devices are used, with the shortest timescale in the sequence the 50$\mu$s probe pulse. This schematic is not to scale, and ignores device delays for clarity.*

allow the atoms to expand for a variable time of flight. The temperature is measured as outlined in Section 3.7 to be $254\mu$K.

To cool the gas further, we ramp the magnetic field gradient to 0 Gcm$^{-1}$ in 5ms and the detuning of the cooling beams from $-14$MHz to $-60$MHz in 3ms, such that the two ramps finish simultaneously. These values are maintained for 3ms of optical molasses cooling, giving us $10^8$ atoms at a temperature of $60\mu$K.

The magnetic trap is loaded in two stages: we switch on the trap at a low gradient (40 Gcm$^{-1}$) to compensate the fall of the cloud due to gravity and to mode-match the initial trap to the cloud, hold for 100ms to allow excitations to die out, then ramp up the gradient to 180 Gcm$^{-1}$ in 100ms to trap $2 \times 10^7$ atoms at $160\mu$K.

We can also load the magnetic trap 8s after a LIAD pulse and trap the same number of atoms. If we measure the exponential decay of the atoms from the magnetic trap which is caused by collisions with background atoms, we see the advantage of using LIAD. The lifetime (time constant of the decay) in the magnetic trap is only 65ms in the continuous dispenser case, the lifetime is 380ms using LIAD (Figure 3.13). (N.B. - our only comparative measurements of trap lifetime were performed after an irreversible degradation of the vacuum. During the optimisation of the magnetic trapping procedure, however, the trap lifetime was over 1s in the constant background case. If the LIAD effect is similarly successful at increasing the lifetime in such conditions, the technique allows a number of fast-evaporation techniques to be attempted.)
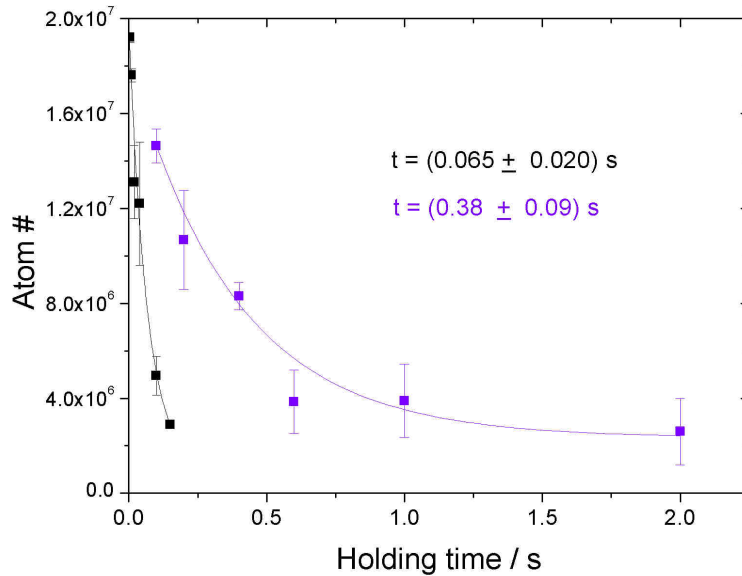


**Figure 3.13:** *Under continuous dispenser or LIAD operation, $2 \times 10^7$ atoms can be loaded into the magnetic trap. The trap lifetime under continuous conditions is only 65ms, but the trap lifetime under LIAD is significantly improved to 380ms.*

From this point, radio-frequency will be used to perform evaporative cooling as in Section 1.4 until the point at which Majorana losses overwhelm the evaporation.

For the MOT / trapping coils, we control the current from the power supply in two ways. For continuous variations of the magnetic field strength, we tune the current using an analogue channel. To achieve fast-switching we have placed used a relay (Crydom D1D40) to quickly break the circuit.

Mechanical shutters are used to block the optical trap beam, the probe beam, the beam from the slave laser or both MOT beams together, and receive 5V trigger signals from digital outputs.

The probe beam is controlled by three devices. The frequency is controlled by the master AOM, and the light is extinguished if either the probe shutter is closed or the AOM trigger is deactivated. The shutter allows us to use the master light to seed the slave laser without the probe light being present in the trapping region. However, the shutter is too slow to allow a short imaging pulse. Once the MOT light is no longer required (after optical pumping) the slave shutter blocks the cooling light. This allows us to now use the AOM trigger (switching speed $1\mu$s) to control the presence of the probe beam appropriately.

Our radio-frequency coils (two single loops of 100mm diameter which are separated by 40mm) are driven by a commercial RF-generator (TTI TG2000), which performs an linear ramp of the radio-frequency radiation upon receiving a 5V trigger. Once the ramp is completed, the frequency is kept constant until a second 5V trigger is used to switch off the generator.

The Optical Pumping AOM is used to bring the optical pumping beam to the appropriate frequency, but the frequency of this AOM need not be dynamically controlled as the master AOM can impart appropriate shifts of frequency. Thus we only control the trigger of this AOM in order to give us fast control of the optical pumping light.

## 3.9   Summary and Prospects

We have built and characterised a simple, single-cell apparatus in which we load atoms from background vapour into a magnetic trap via magneto-optical trapping and optical molasses phases.

In this compact glass-cell, we can successfully load MOTs containing up to $10^8$ atoms, which is a good starting point for evaporative cooling. Lifetime measurements in the magnetic trap, however, indicate that the pressure is too high to achieve this goal.

Although the current lifetime in the magnetic trap does not look promising, we have investigated the Light-Induced Atomic Desorption effect as a method of loading large MOTs at low background pressure. We find that the largest MOTs are achieved by using as much optical power as possible to illuminate the walls of the chamber, encouraging us to experiment with the violet LEDs, which offer greater power than their UV counterparts.

The LIAD effect is seen to deplete the reservoir of atoms on the walls of the chamber over many iterations. We have overcome this depletion by running the atomic dispenser at a minimal current to replenish the coating on the cell.

Vacuum problems have not allowed us to fully investigate the promise of the method to achieve Bose-Einstein condensation in a simple chamber, but we have

demonstrated that the LIAD effect does offer us greatly enhanced lifetime in the magnetic trap. By using a fast evaporation or an alternative efficient strategy, the aim is still to achieve BEC using this apparatus.

As an alternative future strategy, new compact techniques for BEC are being developed regularly. Of particular note may be methods to generate a MOT using planar diffraction gratings [74] and atom chips [72]. The investigations we have performed into LIAD, particularly the methods to create reproducibility, can be of use in experiments based on both of these methods.

# Chapter 4

# Holographic Atom Traps

In Chapters 2 and 3, I have outlined our attempts to reduce the size of the apparatus we use to create ultracold gases. The reason we have not used an atom-chip in this apparatus is that we intend to investigate all-optical methods of creating more flexible trapping structures. In this Chapter I will introduce the techniques used to calculate holographic atom traps and discuss our new approach which, for the first time, creates smooth and arbitrary continuous holographic atom traps using Spatial Light Modulators. I will show examples of the widespread potential uses of our method, and give detailed descriptions of the optical traps we intend to use to investigate a novel approach to bring bosons into the quantum degenerate regime and also to investigate superfluid effects in cold atoms.

## 4.1   Spatial Light Modulators

A SLM is a computer-controlled dynamic diffractive optical device, which consists of an array of individually controllable pixels that imprint phase and / or amplitude information onto an incident light beam. Dynamic manipulation of this light can be achieved by displaying a sequence of phase patterns on the SLM.

Many varieties of SLM exist, such as Digital Micro-mirror Devices (DMDs) or those based on one of two types of liquid crystal technology: either the nematic liquid crystal (NLC) or the ferroelectric liquid crystal (FLC).

As their name suggests, DMDs are controllable arrays of square mirrors (typical mirror sizes are of the order of $10\mu$m). The mirrors can be individually switched between two reflective positions, and thus a beam of light incident on the array undergoes amplitude modulation. Typical use of this technology involves imaging one of these reflected beams to impart the pattern on the surface of the modulator onto the trapping candidate particles (Figure 4.1), but it can be used as a hologram by placing a lens system between the modulator and particles. Dynamic manipulations can be made at rates of up to 50kHz.

In both liquid crystal technologies, the liquid crystals act as a birefringent medium through which the light must pass. The liquid crystals can attenuate the light, causing amplitude modulation, or merely retard the wavefront like a waveplate to modulate only the phase of the light. A combination of phase and amplitude modulation can usually be achieved by varying the polarisation of the incoming
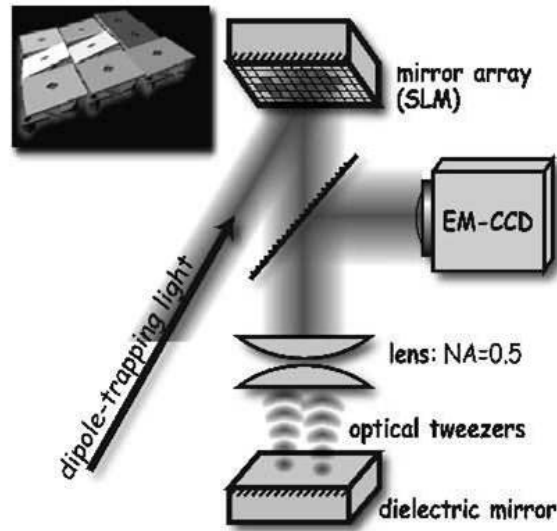
**Figure 4.1:** *Principle of operation of an amplitude modulating Digital Micromirror Device. (inset) Subset of the DMD surface showing mirrors in the two reflective positions. Image from [136]*

light. These devices have a limited diffraction efficiency, resulting in undeflected light forming a bright spot in the output plane. This undeflected light comes from a number of effects, including gaps between the pixels.

The liquid crystal arrangement can be addressed by either optical or by electronic means. Electronic addressing involves voltages being applied directly to individual pixels to align the liquid crystals (see Figure 4.2), and can lead to pixellation effects, while in optically addressed SLMs the liquid crystal alignment is set by the local light intensity of some incoherent reference beam, which has to be created using a spatially-tailored light field.

Similarly to DMDs, FLC devices give very fast frame rates of up to 1 kHz and offer binary pixels which can retard a wavefront by 0 or $\pi$. This restricted flexibility may limit the complexity of the calculated hologram. Additionally, FLCs tend to exhibit a large relaxation effect of the liquid crystal alignment, which can cause an undefined retardation on the light and thus change the light pattern. To combat this, the pixels must be continuously flipped between the two phase values. This in turn presents another problem - as the retardation effect is briefly cancelled during the flips, the diffraction pattern will tend to flicker if too many pixels are flipped at once. Despite these limitations, optical traps for cold atoms have been successfully demonstrated with FLC SLMs [123] after the careful implementation of flicker-limiting measures [137].

In contrast, NLC devices offer much slower variation (of the order of a few tens of Hz), but have a much greater pixel depth, typically allowing hundreds of unique possible liquid crystal orientations. For simplicity of addressing, we have chosen an electronically addressed NLC SLM, while we have made a choice to favour pattern complexity over frame rate. We also operate in phase-only modulation mode, in order to preserve as much optical power as possible.
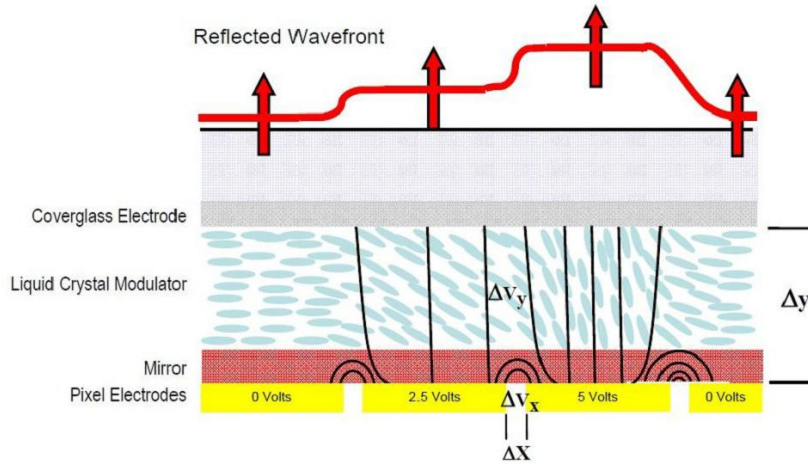
**Figure 4.2:** *Principle of operation of an electronically-addressed nematic liquid crystal SLM. By varying the orientation of the liquid crystals, a retardation can be applied to the light. Image from Boulder Nonlinear Systems*

The SLM we use in the experiments reported in the rest of this thesis is the Boulder Nonlinear Systems BNS XY-series P256 phase-only SLM, which is based on nematic liquid crystals and is used in reflection. The SLM is an array of $256 \times 256$ pixels, each of which can shift the phase of incident light by an arbitrary value between 0 and $2\pi$ in discrete steps of $2\pi/256$. Phase-only modulation is achieved by aligning the polarisation of the incoming light to the vertical axis of the SLM, while some amplitude modulation can be achieved by shifting the polarisation by 45°. The brightness of the zeroth order of undiffracted light is minimised when the light is vertically polarized, i.e. when there is no amplitude modulation.

## 4.2 Experimental Apparatus

Our light source for diagnostics is a temperature stabilised, free-running laser diode (Roithner RLT1060−100G) emitting at $\lambda = 1060$nm which can output up to 100mW of light. The beam is spatially filtered using a polarization maintaining optical fibre, and collimated to a $\frac{1}{e^2}$ beam waist of 6.04mm to cover the full array of the SLM ($6.14 \times 6.14$mm). This gives us almost uniform illumination of the SLM array; all of the pixels are illuminated by comparable power and can therefore impart phase changes on the beam. In order to improve the fibre-coupling of the highly-astigmatic beam, we have used anamorphic prisms and a pair of cylindrical lenses, which have $f = 75$mm and $f = 150$mm.

After the fibre output, a $\lambda/2$ waveplate and a PBS provide polarization filtering to ensure that phase-only modulation is achieved, before the beam is directed onto the SLM with a narrow incidence angle ($\sim 6.5°$). The reflected beam is then focused using a plano-convex achromatic doublet lens, with typical focal lengths in the range 50mm to 200mm. To monitor the output intensity distribution we have used two techniques: block the zeroth order of the diffraction pattern on the focal plane and

magnify the first diffracted order by a factor of four onto a CCD camera (Thorlabs DCU224M); or image the output field directly onto the CCD camera in the focal plane. The camera has 1280 by 1024 square pixels of side $4.65\mu$m. The optical setup is shown in Figure 4.3.

In our original investigations, the SLM was controlled using Boulder Nonlinear System's Blink software. This consisted of a "drag and drop" window, where the user can upload a list of .bmp files of the desired phase patterns, placing them in a list in order of display, and specify parameters such as the refresh rate. The Blink software then sends appropriate instruction to a Data Acquisition Card, which was also supplied by Boulder Nonlinear Systems. Latterly, we decided to develop our own software to control the DAC using MATLAB, as all calculations for producing phase masks and also the control of the camera were performed in MATLAB.
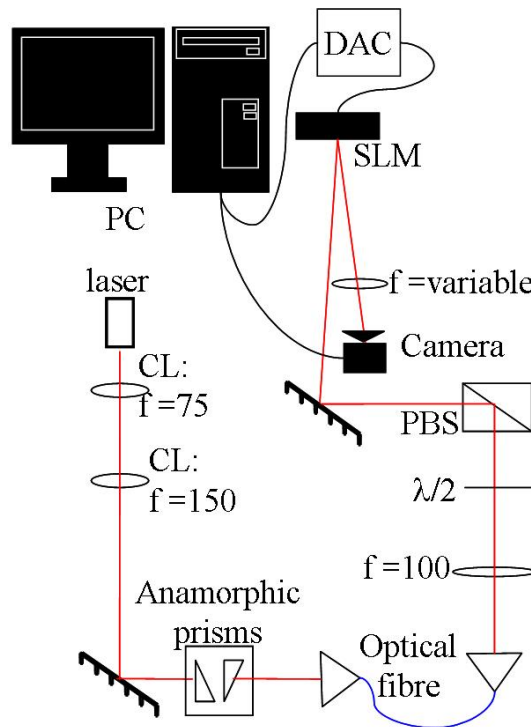


**Figure 4.3:** *The test apparatus for the SLM. Cylindrical lenses (CL), anamorphic prisms and a single-mode, polarization maintaining optical fibre are used to produce a Gaussian beam profile. The fibre output is collimated to overfill the active area of the SLM, and is polarized to ensure phase-only modulation. The light is focussed by a lens, and the image in the focal plane recorded by a camera. The camera and the SLM are controlled by the same computer. All focal lengths are in mm.*

Since the intensity recorded on the camera is integrated over the exposure time of each frame, we can alternatively replace the camera with a fast photodiode which gives us the intensity variation on much faster time scales.

The undiffracted light (zeroth order) is made brighter by our overfilling the active area as the mount surrounding the SLM array is partially reflective. To combat this we have constructed a non-reflective mask to surround the SLM array.

Positioning this mask anywhere else in the beam path can cause additional fringes in the diffraction pattern.

Phase modulation provides precise control of the intensity in the trapping plane, but the behaviour of the intensity out of the focal plane is unpredictable, and does not necessarily diverge quickly enough to provide confinement in all directions. To provide stable 3D confinement when we integrate the SLM into the experimental apparatus of Chapter 3 we intend to use one of two approaches. Firstly, a light sheet can be applied orthogonal to the trap beam to provide a tight confinement. For some applications (see Section 4.13), we intend to recycle and reuse the trap beam after it has left the vacuum chamber in a figure-four configuration. The additional confinement beam will replace the photodiode which is currently used to monitor the number of atoms in the MOT.

Whilst we have used a limited power for diagnostics, our SLM can be illuminated by up to 3.5 Wcm$^{-2}$. To accomplish this, we have installed a 3W 1064nm diode laser-pumped solid state laser based around a Nd:YVO$_4$ crystal. This beam will be polarised using a PBS and will be directed onto the SLM as shown in Figure 4.4. In order to allow imaging in the plane of the optical trap, we intend to align the trap beam with the imaging probe beam. The diffracted beam will be overlapped onto the probe beam using a dichroic mirror and the lens of the imaging system is used to focus the beam onto the atoms.

Pre-cooling is likely to be performed in a quadrupole magnetic trap until the point at which Majorana losses become significant. At this point the optical trap will be turned on.
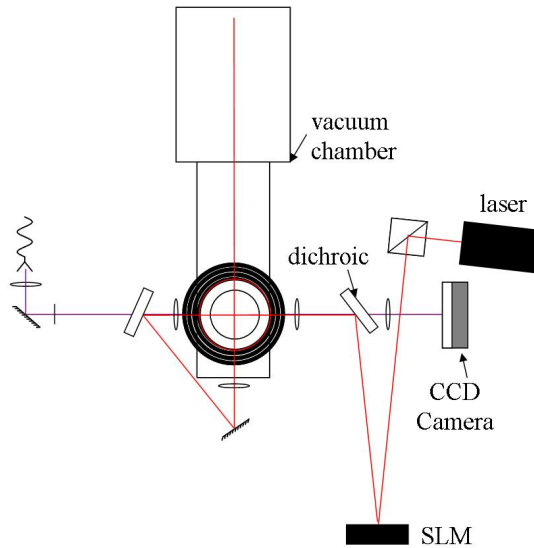


**Figure 4.4:** *Combination of the cold atom experiment and the SLM. The laser is the 3W 1060nm laser. Red beams denote trapping beams, whilst purple are probe beams. The first lens in the imaging setup also acts as the focussing beam for the optical trap.*

## 4.3 Calculating Holograms

The calculation of a light field at another plane is relatively straightforward provided one has appropriate initial conditions: e.g. if one knows the amplitude and phase in one plane. This remains true in holography: given a fixed hologram and incident beam, we can predict the resultant intensity distribution when the beam is focussed with a lens by means of a Fourier transform (assuming the paraxial approximation).

However, if we know only the amplitude information in two planes and want to find a phase hologram which connects them, the calculation becomes more difficult. A seemingly obvious simplification would be to assume flat phase in the output plane, and calculate the hologram phase by means of an inverse Fourier transform. The phase calculated this way generally has real and imaginary parts, meaning modulation must be made to both the phase and the amplitude of the light field. This is not desirable for trapping applications as one deliberately loses power in amplitude modulation.

Physics gives us a helping hand in this problem: for far-off resonant optical dipole traps the phase is unimportant for the trapping potential provided the dipole approximation is valid. This "phase freedom" in the output plane gives us the capability to calculate the hologram: disregarding the output phase, we can now optimise the input phase to produce the amplitude of interest in the output plane. The mathematics of this problem is still non-trivial, and the calculation is a well-known inverse problem with multiple possible solutions. In order to calculate the required phase pattern, a number of algorithms exist, which are described in the following sections.

## 4.4 Programming Simple Gratings

A simple method of arranging a limited number of discrete spots in the output field is to program a linear superposition of simple grating functions. We refer to this method as the "point by point" method. A simple grating creates a single diffraction-limited spot at a position in the output plane, as in Figure 4.5. This grating is given by

$$\phi\left(x, y\right) = \left(\alpha x + \beta y\right) \bmod \left(2\pi\right). \tag{4.1}$$

By changing the periodicity of this grating, i.e. by varying $\alpha$ and $\beta$, the distance between the spot and the zeroth order (centre of the Fourier plane) can be varied, as shown in the middle frame of Figure 4.5. The spot can also be moved about the zeroth order by rotating the grating as in the bottom frame of Figure 4.5.

These gratings can be combined using a linear superposition to place multiple points in the output plane. For example, using an equal superposition of the first two gratings in Figure 4.5 one obtains the uppermost grating and output in Figure 4.6, i.e. two spots of equal brightness.

If one wishes the spots to have different brightness, then an unequal superposition can be used (Figure 4.6 (middle)). More spots can be placed in the field simply by superimposing more gratings, as in Figure 4.6 where we attempt to place 3 spots
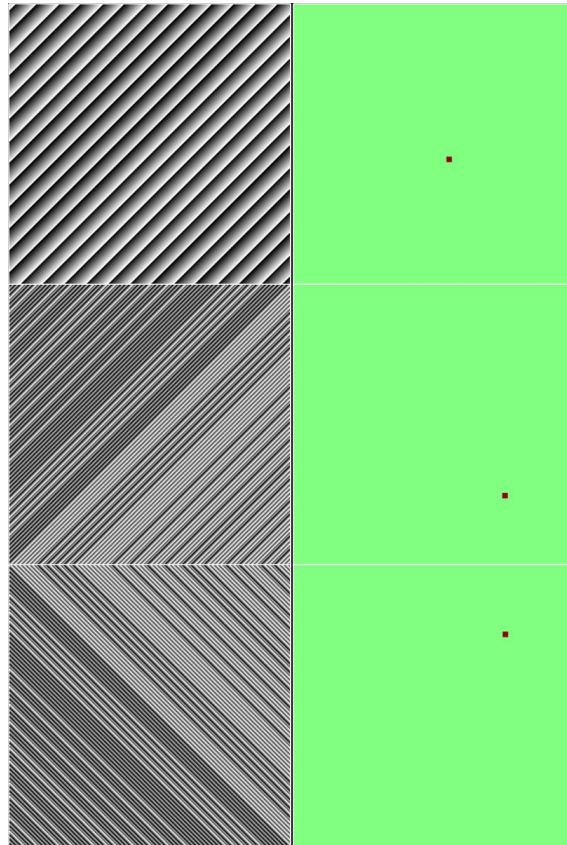
**Figure 4.5:** *(top) A simple grating leads to a diffraction limited spot in the Fourier plane. By changing the periodicity (middle) and angle (bottom) of the grating, the spot can be moved around the Fourier plane*
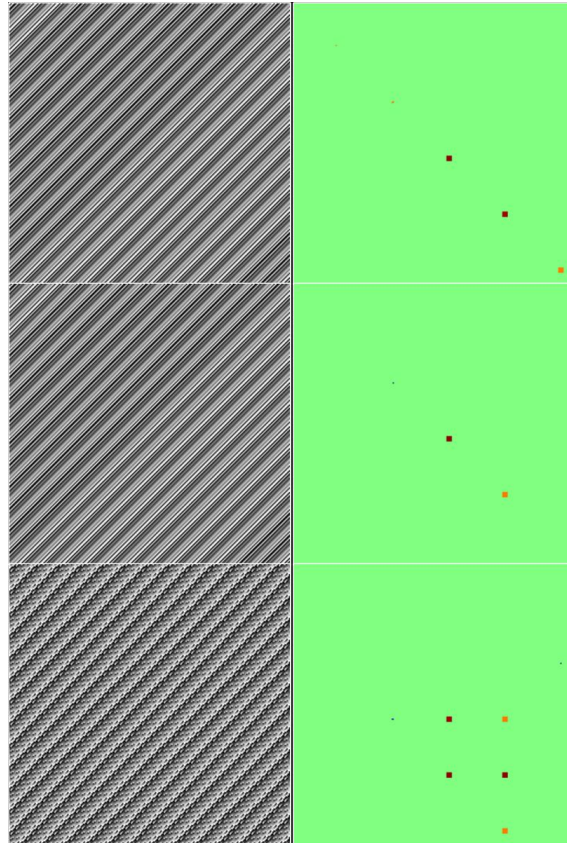
**Figure 4.6:** *(top) Equal superposition of two linear gratings to give two equally bright spots. (middle) Weighted superposition to create spots of different intensity. (bottom) In adding a third spot, additional diffracted orders begin to constructively interfere, leading to 'ghost' spots (orange).*

in the plane. At this stage, it becomes apparent that the method is not allowing complete control over the output field: as well as the programmed (red) spots in this field, there are two additional, fainter spots (orange). This can be understood if one remembers that we are programming diffraction gratings: these spots are constructive interference between higher diffracted orders of the grating. We refer to these additional spots as 'ghost' spots.

This simple algorithm can create single spots or simple symmetric arrays without the ghosts being present. However, the size and shape of the spots is not easily manipulated, and continuous patterns are impossible without some form of time-averaging.

## 4.5 Alternative Methods

Given the limitations of the "point by point" method, another method for finding the hologram is required.

One such method, which has been previously used to generate atom traps with a FLC SLM in Oxford, is the Direct Binary Search (DBS) algorithm [138]. DBS, as the name suggests, restricts the hologram to two phase values, 0 and $\pi$. To begin, an arbitrary pattern of pixels is generated, a Fourier transform is carried out and the intensity pattern this produces is compared to the desired intensity distribution to produce an error function.
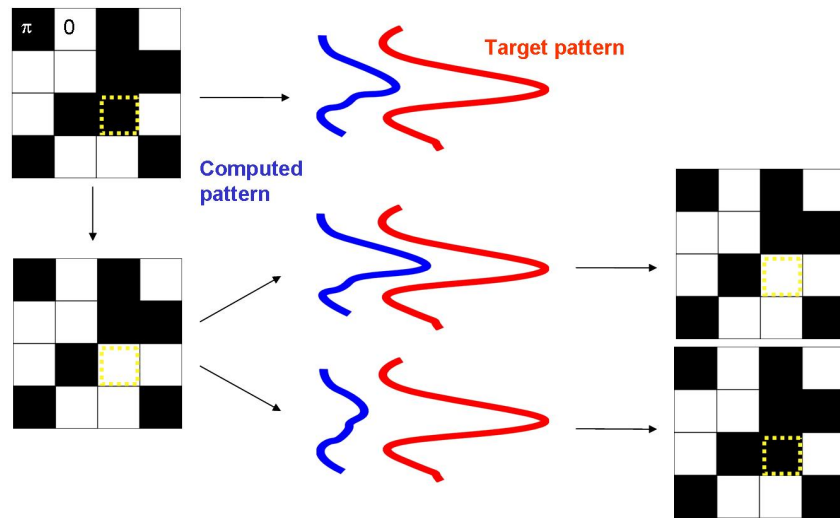


**Figure 4.7:** *An initial phase is iteratively optimised using Direct Binary Search. A random pixel is changed from the initial phase pattern, and a Fourier transform computed. If the output is closer to the target, then new pixel value is maintained, otherwise it is reset. Image courtesy of G. Smirne.*

The algorithm then flips the value of a random pixel, and calculates the new error function. If the error function shows that the new pattern is closer to the desired result, the change is kept, otherwise the pixel is reset (as demonstrated in Figure 4.7). This process is iterated until the desired pattern is reached.

Local traps in the iterative improvements exist using this method, although they can be corrected using modifications such as the simulated annealing method [139]. More troublesome is the fact that, for binary holograms, this method is computationally intensive - for holograms of 256 possible phase levels it becomes even more demanding.

The DBS method could be used with a high speed supercomputer, but if one has such a resource a better method is to use Genetic Algorithms [140]. These are an example of evolutionary computation, and produce higher accuracy holograms than achievable with DBS, although the computing needs are very high, putting such algorithms out of reach for most atomic physicists.

## 4.6 Iterative Fourier Transform Algorithms

One computationally efficient method to calculate holograms does exist, and is known as the Iterative Fourier Transform Algorithm (IFTA). This algorithm places three constraints on the problem: we know the intensity distribution at both the SLM and the plane of interest; we can change the phase at the SLM at will; and we do not care about the phase at the plane of interest. The IFTA also starts from a guess hologram and a convergence is obtained by iteratively Fourier transforming between the two planes and enforcing the amplitudes required while maintaining the evolving phase pattern.

### 4.6.1 Gerchberg-Saxton Algorithm

The original IFTA was developed by Gerchberg and Saxton in 1972 [141]. It allows one to calculate a phase mask that converts an input amplitude $A_0(x, y)$ (usually given by a Gaussian laser beam which is apodized by the physical dimensions of the hologram or spatial light modulator) into a target intensity $I_0(x', y')$. The IFTA models the propagation of the light through a lens and into the focal plane by means of fast Fourier transforms (FFTs). A block diagram showing the key steps of an IFTA is shown in Figure 4.8.

The first step in an IFTA is to make an educated guess $K_0(x, y)$ to the required phase pattern on the SLM (more details are included in Section 4.7.1). This gives an input light field $E_{in}^{(1)} = A_0 e^{iK_0}$.

To find the effect of this hologram in the focal plane of the lens, we calculate the Fourier transform $\mathcal{F}$ of the input field to find $E_{out}^{(1)} = \mathcal{F}\left(E_{in}^{(1)}\right)$. This gives an electric field in which the amplitude is probably incorrect, but can be made acceptable by replacing the amplitude with one which matches $I_0$. This gives an electric field of the form $G^{(1)} = \sqrt{I_0} e^{i \arg\left(E_{out}^{(1)}\right)}$.

This new field is then propagated back to the plane of the SLM by means of an inverse Fourier transform $\mathcal{F}^{-1}$ to give an electric field. The amplitude of this field is unlikely to match the illumination of the SLM, so is replaced by $A_0$, to give the starting point for the next iteration of the loop $E_{in}^{(2)} = A_0 e^{i \arg\left(\mathcal{F}^{-1}\left(G^{(1)}\right)\right)}$.

For subsequent iterations, $\left|E_{out}^{(n)}\right|^2$ is compared to $I_0$, using a figure of merit $\eta$
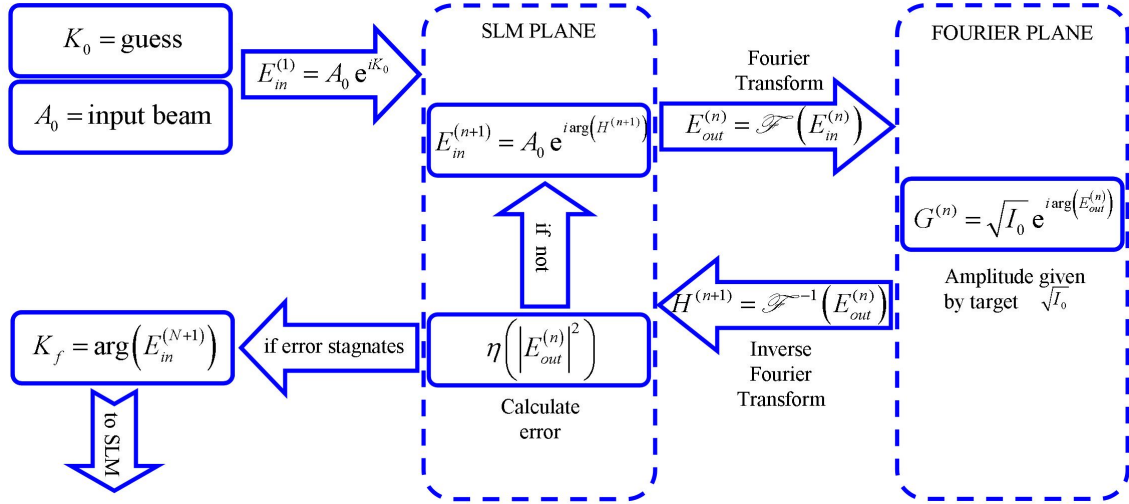
**Figure 4.8:** *Schematic representation of an Iterative Fourier Transform Algorithm.*

given by

$$\eta = \sqrt{\frac{1}{N_{pixels}} \sum_{x',y'} \frac{\left(\left|E_{out}^{(n)}(x',y')\right|^2 - I_0(x',y')\right)^2}{I_0(x',y')^2}}. \tag{4.2}$$

If $\eta^{(N)}$ is no better than $\eta^{(N-1)}$, the algorithm terminates and the final phase $K_f = \arg\left(E_{in}^{(N+1)}\right)$ is sent to the SLM.

This algorithm works well for arrays of discrete spots of light, but continuous patterns are unusable, as all the patterns generated with this method contain a large quantity of speckle in high intensity regions. Modified versions of the Gerchberg-Saxton algorithm have been created to overcome this deficiency.

## 4.6.2 Adaptive-Additive Algorithm

In an effort to remove the speckle effect from the optical traps, a degree of amplitude freedom in the focal plane was introduced via the Adaptive-Additive (AA) algorithm [142]. The key difference from the GS algorithm is the amplitude replacement in the Fourier plane $G^{(n)}$, given by

$$G^{(n)} = \left(m\sqrt{I_0} + (1-m)E_{out}^{(n)}\right)e^{i\arg\left(E_{out}^{(n)}\right)}. \tag{4.3}$$

The electric field from the previous iteration is mixed with the target intensity, with the relative weighting given by a mixing parameter $m$ which is positive and less than unity (when $m = 1$, $G^{(n)}$ is the same as for the GS algorithm). This addition of a degree of amplitude freedom reduces the level of speckle in the regions where the intensity given by $I_0$ is non-zero and allows the algorithm to converge more quickly,

at the expense of power efficiency. The smoothness of patterns improves, but not sufficiently to even consider trapping atoms in the resultant intensity pattern.

### 4.6.3   Mixed-Region Amplitude-Freedom Algorithm

In 2008, Pasienski and DeMarco designed a modified version of the AA algorithm with the explicit goal of achieving smooth intensity distributions for the purposes of trapping atoms [143]. As shown in Figure 4.9, the main difference is to separate the output plane into two subsets: the signal region (where we want to control the atoms with our holographic optical trap) and the noise region (far from the trapping region). In the noise region one permits both phase and amplitude freedom, *c.f.* the AA algorithm. However, in the signal region only phase freedom is permitted, *c.f.* the GS algorithm. By ensuring a sizable region of zero light intensity at the boundary of the signal region, atoms are prevented from tunnelling into any light in the noise region. In this way, $G^{(n)}$ becomes

$$G^{(n)} = \left( m\sqrt{I_0}\big|_{SR} + (1-m) \left| E_{out}^{(n)} \right|_{NR} \right) e^{i\arg\left( E_{out}^{(n)} \right)}. \tag{4.4}$$

The effect of dividing the plane in this way is to improve the accuracy of the algorithm within the signal region at the expense of accuracy in the noise region. By allowing light in the noise region, the power efficiency of the hologram suffers by typically a factor 3 or 4.

Analysis on the quality of the light pattern, as discussed in Section 4.7.3, are performed within a third subset. This "Measure Region" is defined to be the subset of the signal region in which the intensity is non-zero.



**Figure 4.9:** *An example target, along with the associated signal region, noise region and measure region. During the IFTA, the light in the signal region will be constrained to match the target, whilst the amplitude in the noise region will be undefined. This allows greater accuracy within the signal region.*

The algorithm calculates smooth optical potentials, which should avoid fragmentation of a cloud of ultracold atoms, surrounded by dark regions to minimise atom losses to light in the noise region. It provides excellent predictions for both discrete and continuous intensity distributions. Until the work presented below, experimental achievement of optical traps suitable for ultracold atoms using this algorithm had not been shown [143, 144].

MRAF is capable of calculating the phase required to generate the desired intensity distribution regardless of the incoming beam profile, so in future the overfilling we apply with our expanded illuminating beam could be relaxed to allow more power in the optical trap.

## 4.7  Hologram Calculation

### 4.7.1  Setting Initial Phase

Having generated the target pattern and defined the signal and measure regions, the initial step for the IFTA must be generated. A guess is made to the initial phase profile $K_0$. The optimal $K_0$ is generally one that slightly overfills the signal region. The guess is critical not only in speeding up the algorithm and improving the accuracy of the output, but also must not produce unwanted optical vortices in the output plane as these cannot be removed by the IFTA once they appear in any iteration of the algorithm [143].

We calculate $K_0$ by linear superposition (modulo $2\pi$) of a sequence of gratings for which we know the Fourier transform:

$$K_0 = K_C + K_Q + K_L. \tag{4.5}$$

$K_L$ is a linear phase profile such as those in Section 4.4 which shifts light from the centre of the image plane. $K_Q$ is a quadratic phase profile which acts as a lens, moving the image of the SLM closer to or farther from the focal plane. The effect is to spread out the intensity within the output plane in the first step of the IFTA. $K_C$ is a conical phase profile which can be used to generate rings in the intensity without producing optical vortices. These profiles are given by:

$$K_L = D\left(X\cos\theta + Y\sin\theta\right), \tag{4.6}$$
$$K_Q = 4R\left(\gamma X^2 + (1-\gamma)Y^2\right), \tag{4.7}$$
$$K_C = B\sqrt{(X^2 + Y^2)}, \tag{4.8}$$

where $D$ controls the distance from the centre of the output plane and $\theta$ the angle ($\theta = 0$ is defined to place light to the left of centre); $R$ controls the amount of "stretch" applied to the light and $\gamma$ controls the aspect ratio; and $B$ gives the radius of a dark ring in the field (see Figure 4.10).

For some of the light patterns created, it is possible to define these parameters as a function of the parameters of the target, but in many cases the best guess is determined empirically. A Graphical User Interface (Figure 4.11) was developed to display the difference between the predicted output and signal region for user-specified values of $D$, $R$, $B$, $\gamma$ and $\theta$ for any uploaded target image. When one of the parameters is changed, the initial field $A_0 e^{iK_0}$ is Fourier transformed to give a predicted output. This is compared to the signal region by means of a subtraction, and displayed on screen along with the target. The Fourier transform and update of display run in real time, allowing fast empirical optimisation of the guess.
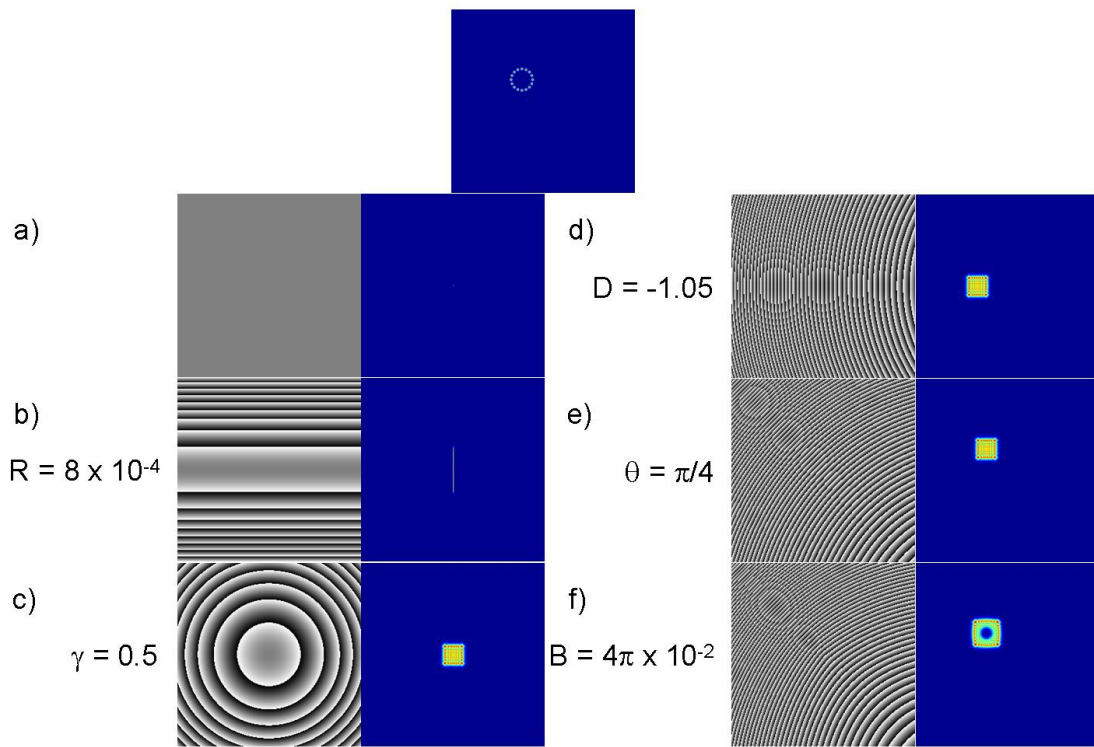
**Figure 4.10:** *Evolution of the guess phase. (top) Target pattern. a) No phase mask leaves a diffraction limited spot in the centre of the output plane. b) Setting $R \neq 0$ stretches the intensity. c) Setting $\gamma \neq 0$ changes the aspect ratio of the intensity. d) Setting $D \neq 0$ moves the intensity within the plane. e) Setting $\theta \neq 0$ changes the position of the intensity around the centre of the plane at constant radius. f) Setting $B \neq 0$ produces a ring in the plane.*
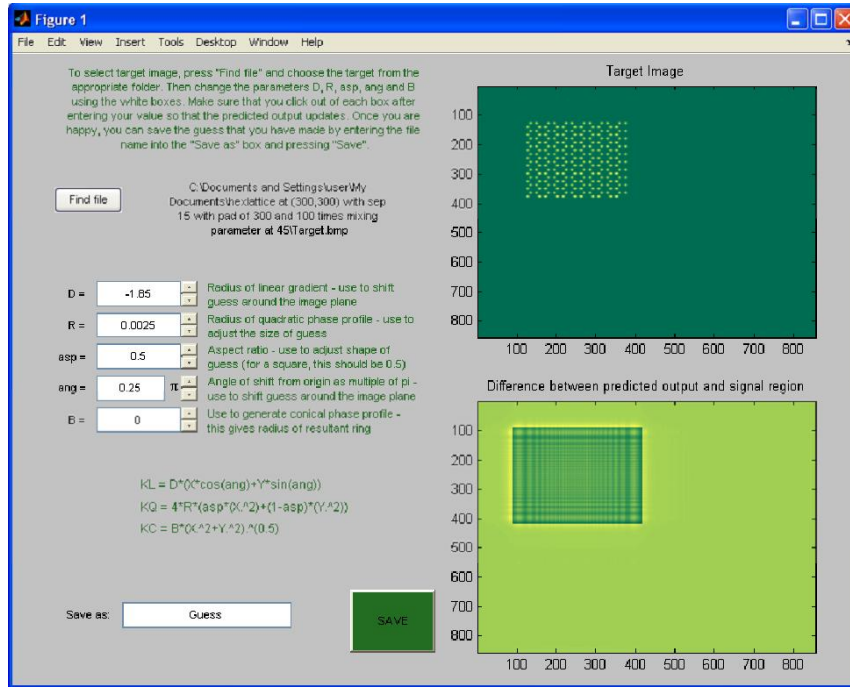
**Figure 4.11:** *The GUI to enable fast production of the phase guess required to start the IFTA. The images in the figure update in real time to give the user an indication of the effect of the phase guess on the intensity after one Fourier transform.*

In addition to the guess method outlined above, we tried using the output phase from a GS IFTA (Section 4.7.6) to generate a guess for the start point of an MRAF IFTA, as GS tends to converge quickly but inaccurately.

### 4.7.2   Padding of the Field

The resolution of details in the experimental output of the algorithms is restricted by the diffraction limit $l$ of the optical system:

$$l \approx 1.22 \frac{\lambda f}{D}, \tag{4.9}$$

where $f$ is the focal length, $D$ the diameter of the lens, and $\lambda$ the wavelength of the light. In order to create optical patterns with this resolution, we can extend the optical field in the calculation by including a zero-intensity region around the field of view within the algorithm. Although the illumination in the input field is restricted by the size of the SLM, there is no reason to restrict the output field to the same size. The input field can be arbitrarily grown inside the computer by adding a zero intensity region around the outside.

The size of the "pad" is optimized using the following procedure. Firstly, we generate a simple (unpadded) diffraction grating to give two spots in the output plane. We measure the separation $d_p$ (measured in number of pixels) of these spots in the predicted output and the separation $d_m$ (measured in mm) in the actual output obtained by applying this grating to the SLM.

For a square SLM with $M$ pixels along one side, the field of view in the Fourier plane is given by

$$F = M \frac{d_m}{d_p}. \tag{4.10}$$

If we want to create optical patterns with this resolution, we need $\frac{F}{l}$ pixels to do this. Thus the optimal size $P$ of the pad (the number of empty pixels on each side of the target array) is

$$
\begin{aligned}
P &= \frac{1}{2} \left( \frac{F}{l} - M \right), \\
&= \frac{M}{2} \left( \frac{d_m D}{1.22 \lambda f d_p} - 1 \right). \tag{4.11}
\end{aligned}
$$

### 4.7.3 Evaluation Metrics

The predicted light pattern for the hologram produced by the IFTA does not provide a perfect match to the target pattern: we expect deviation within the noise region, but intensity variations also occur within the measure region. These will have an adverse effect on the suitability of the pattern for atom trapping, as atoms will be most strongly attracted to the brightest regions.

To optimise and evaluate the hologram generated, we use a number of metrics. The number of iterations the algorithm takes to exit has moderate importance: while few iterations are beneficial from a time-management viewpoint, a large number of iterations is acceptable if the pattern quality is especially high.

The exit point of the algorithm is determined by a stagnation of the error function $\eta$ which is the intensity-weighted RMS difference between the predicted output and the target intensity:

$$\eta = \sqrt{ \frac{1}{\sum\limits_{x',y' \in MR} 1} \sum\limits_{x',y' \in MR} \frac{\left( I_{pred}\left(x',y'\right) - T\left(x',y'\right) \right)^2}{T\left(x',y'\right)^2} }, \tag{4.12}$$

where $MR$ denotes the measure region, $x', y'$ are co-ordinates in the output plane, $T$ is the target intensity profile and $I_{pred}$ is the predicted intensity. For every potential pattern, we vary the mixing parameter $m$ to minimise $\eta$.

When considering experimental use of the holograms, one important parameter to maximise is the efficiency $\xi$, which is the percentage of the total intensity contained within the signal region of the predicted output.

$$\xi = \frac{\sum\limits_{x',y' \in SR} I_{pred}}{\sum\limits_{x',y'} I_{pred}}. \tag{4.13}$$

Large efficiency will allow deeper traps for cold atoms. As expected, $\xi$ usually increases with mixing parameter $m$. Unfortunately, $\eta$ also usually increases with $m$.

For discrete arrays of spots, we consider the discrepancy $\Delta$ which is the difference between the peak intensity of the spot in the target and the peak intensity of the spot in the predicted output. We also consider the range $R$ of discrepancies across the whole array of spots: the difference between the largest and smallest $\Delta$.

These metrics will also be applied to the real light fields which are measured after the holograms are sent to the SLM.

### 4.7.4   Progression of an IFTA

Once the target, guess phase and pad size have been defined and the output plane divided in to the appropriate regions, the IFTA is run. Further input parameters are the mixing parameter $m$, the maximum number of iterations, and the stagnation parameter.

This stagnation parameter is compared to the difference between the error $\eta$ (as defined in (4.12)) of subsequent iterations of the IFTA. The IFTA rarely stagnates completely ($\Delta\eta = 0$), so we specify instead a tolerance. If $\Delta\eta$ falls below this tolerance, the algorithm terminates. Figure 4.12 shows the evolution of both $\eta$ and $\Delta\eta$ with number of iterations, where the stagnation parameter is $10^{-3}$.
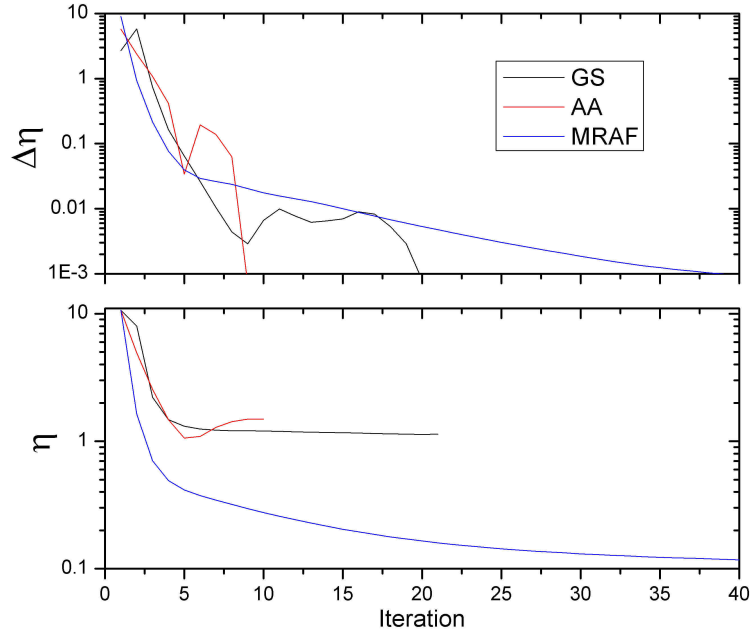


**Figure 4.12:** *The evolution of the hologram accuracy during the iterations of the IFTA. The lower graph shows the value of the error for each of the three types of IFTA: Gerchberg-Saxton (black), Adaptive Additive (red) and Mixed-Region Amplitude Freedom (blue). The upper graph shows the difference between this error for consecutive iterations. When $\Delta\eta$ falls below the stagnation parameter ($10^{-3}$) the algorithm terminates.*

We use the same guess to run all three types of IFTA, meaning $\eta(1)$ is the same for all three IFTAs. Increasing the number of iterations tends to decrease the value of $\eta$, but this is not strictly so. As can be seen by inspecting the evolution of the Adaptive Additive algorithm, the optimal hologram may be found before the algorithm terminates. This occurs when the stagnation parameter is set to a high value. When holograms are to be generated for output to a physical device, the stagnation parameter we use is between $10^{-5}$ and $10^{-6}$, which gives us greater accuracy as shown in Figure 4.13.
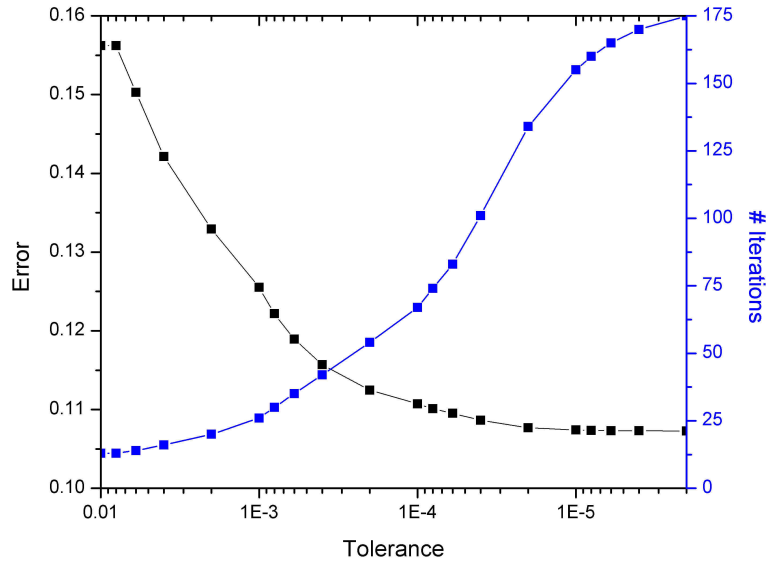


**Figure 4.13:** *By lowering the stagnation tolerance, the algorithm takes more iterations to exit the IFTA, but increase the accuracy of the light pattern. This improvement becomes less noticeable beyond a tolerance of $10^{-5}$, so typical holograms for experiments are generated with tolerance in the range between $10^{-6}$ and $10^{-5}$*

As can be seen by the differing termination points between algorithms, a low stagnation parameter does not necessarily give a low error $\eta$. As this is the case, a number of different phase guesses must be generated for any proposed hologram and a number of mixing parameters $m$ must be investigated, in order to minimise $\eta$.

## 4.7.5 Optimisation of an IFTA

In the optimisation of the output hologram, we typically vary the guess parameters so that the guess narrowly overfills the signal region of our desired pattern. As examples, consider the two patterns shown in Figure 4.14: a continuous ring with two bright spots and a ring lattice of discrete spots. These rings have the same radius, although the thickness of the continuous ring is greater than the size of the individual spots in the ring lattice.

Figure 4.14 shows the Fourier transform of 25 possible guesses, where $R \in (0.8, 1.2) \times 10^{-3}$ is the size of the rectangular output and $B \in (20, 40) \times 10^{-3}$ is the size of the dark ring.
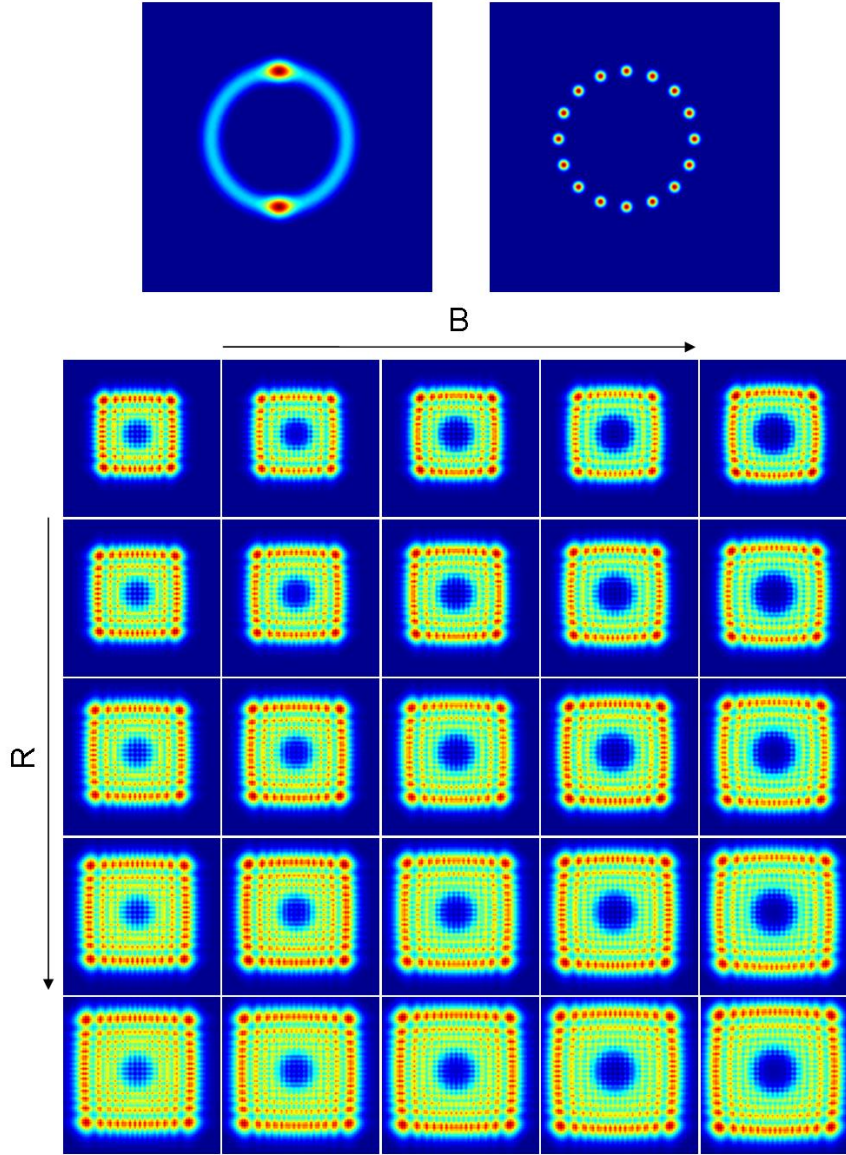


**Figure 4.14:** *The two target patterns used in Sections 4.7.5 and 4.7.6, along with the range of initial guess outputs used in optimising the hologram. Two of the guess phase parameters are varied, R controlling the size of the light region and B the size of the dark ring.*

The reason for selecting a range of guesses becomes apparent upon inspection of the top ten combinations of guess and $m$ in terms of accuracy (Table 4.1). Although it is clear that larger values of $R$ are better, the full range of $B$ values are present. Furthermore, by selecting the ninth most accurate combination, 40% additional optical power can be obtained, although the error increases by 0.11% due to the larger mixing parameter.

| $R$ | $B$ | $m$ | $\eta$ | $\xi$ |
|-----|-----|------|---------|---------|
| 1.2 | 20 | 0.38 | 0.01066 | 0.27687 |
| 1.1 | 40 | 0.37 | 0.01094 | 0.26048 |
| 1.1 | 40 | 0.38 | 0.01095 | 0.27726 |
| 1.2 | 40 | 0.36 | 0.01095 | 0.2435 |
| 1.2 | 20 | 0.39 | 0.01121 | 0.29368 |
| 1.2 | 30 | 0.38 | 0.01139 | 0.27715 |
| 1.2 | 30 | 0.37 | 0.01144 | 0.26045 |
| 1.2 | 40 | 0.37 | 0.0115 | 0.25964 |
| 1.0 | 40 | 0.44 | 0.01171 | 0.38823 |
| 1.2 | 20 | 0.40 | 0.01176 | 0.31149 |

**Table 4.1:** The ten combinations of guess phase and mixing parameter $m$ which give the lowest value of error $\eta$.

The variation with $m$ is generally more predictable. As can be seen in Figure 4.15, increasing $m$ improves the efficiency of the output, at the expense of quality. The efficiency gain is monotonic, but the error is optimally low for $m \in (0.3, 0.5)$. The precise value of the optimal $m$ varies for different patterns, so must be investigated for each new hologram.

In a typical optimisation routine, we run the IFTA with around 5 values of $R$ in the phase guess (for circular patterns we also use 5 values of $B$, giving 25 permutations) and mixing parameters in the range $(0.35, 0.45)$. On our modest desktop computer, one hologram takes around 3 minutes to calculate. In order to calculate an optimal new hologram, $3 - 10$ machine-hours is allowed. This limitation of generating optimal holograms is offset in three ways: once the optimal hologram is calculated, the phase is saved and does not need to be calculated again; the holograms generally do not have to be calculated in real time, so are typically left to run overnight; and, as discussed in Section 4.8, the actual output when a hologram is placed on an SLM is far from optimal. Under typical operating conditions, we do not fully optimise the hologram, but try to find one which gives a predicted error under 1%.

The MRAF IFTA can be performed using the output of the GS algorithm as an input phase. The error is found to be comparable using this method, but a major difference is the distribution of light in the noise region. Using a standard guess with a low mixing parameter often creates a high-intensity boundary around the SR. The aim of the dark region surrounding the measure region is to prevent atoms being attracted into the noise, but if the noise intensity is particularly high the trapping potential may be perturbed. As shown in Figure 4.16, when the GS phase pattern is used in the initialisation of the MRAF IFTA the noise is distributed in a speckle pattern throughout the noise region, instead of surrounding the signal region. Although we have not used this method in the work in the rest of this thesis, it could be useful in experiments if the high intensities at the boundary of the signal region do trap atoms in unwanted regions.
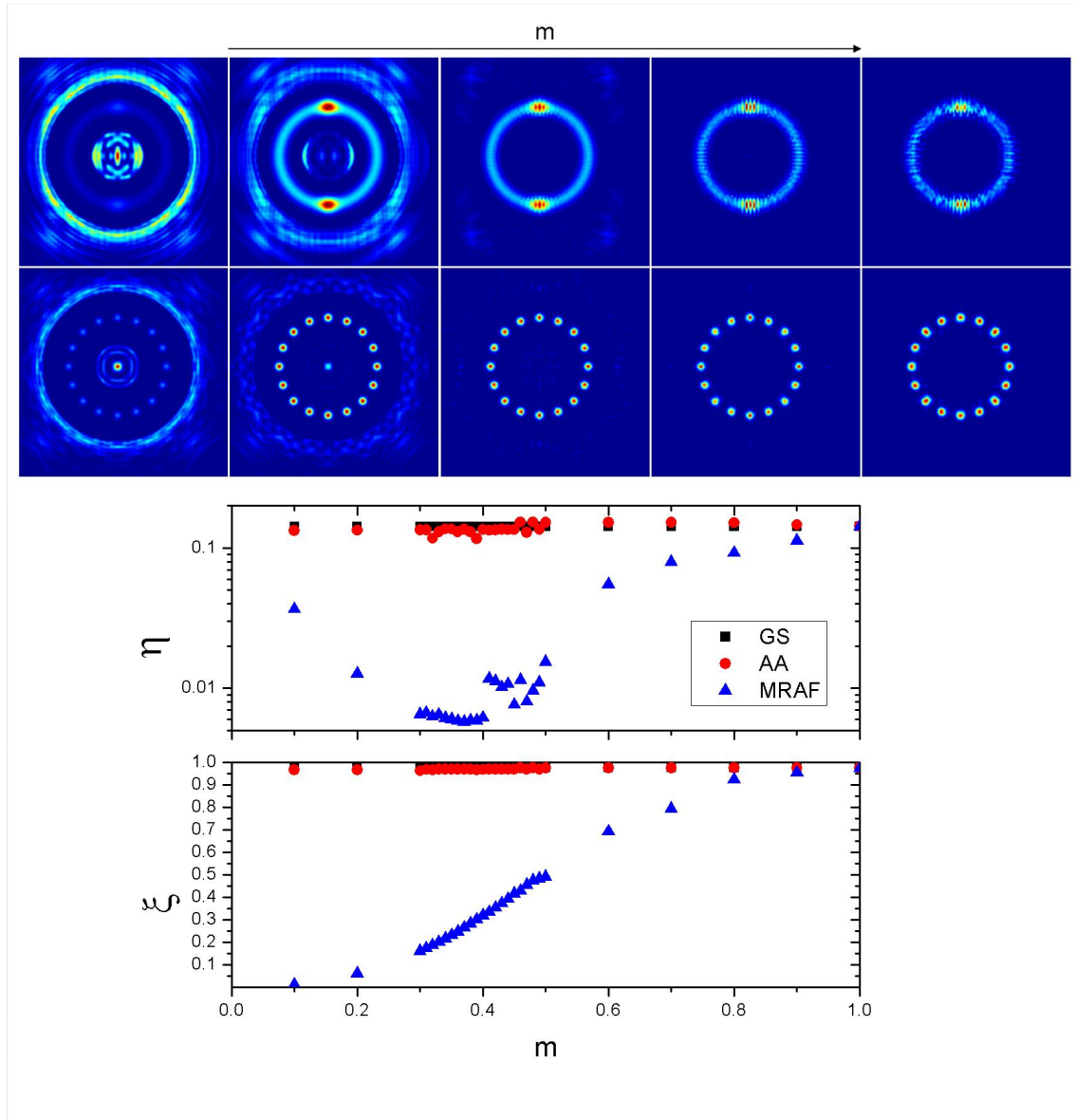
**Figure 4.15:** *Both holograms become more efficient as m is increased. As can be clearly seen in the continuous pattern, however, high values of m give fragmented light patterns. The graphs show that the optimal m for high accuracy is between 0.3 and 0.5.*
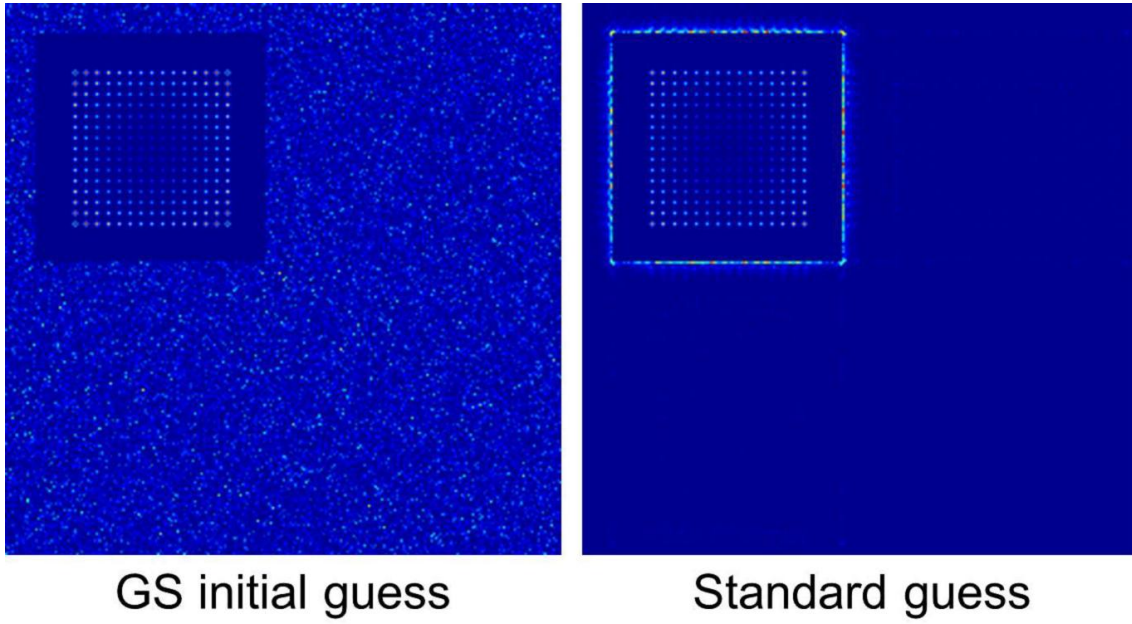
**Figure 4.16:** *(left) Tapered square lattice generated with a standard guess. (right) Tapered square lattice generated with the GS output. The noise is spread more evenly across the noise region when the GS algorithm output is used to start the MRAF IFTA.*

### 4.7.6 Comparison of IFTAs

As was shown in Figure 4.12, the MRAF algorithm tends to a more accurate hologram than the other algorithms, and does so more quickly. The graphs in Figure 4.15 also show that MRAF is more accurate than the other forms of IFTA, at the expense of efficiency.

By examining the predicted outputs for two of the target patterns in Section 4.7.5, we can see the true benefit of using the MRAF algorithm over any of the others (Figure 4.17). For the discrete case, the accuracy within the spots is comparable for the three IFTAs, but the point by point method produces an array of point-like spots rather than Gaussian spots. The main advantage of MRAF in this case is that this algorithm does not allow the small fluctuations around the spots that can be seen in all of the other predicted outputs.

For continuous patterns, the point by point method cannot be used. Of the three IFTA outputs, only MRAF gives a smooth output within the signal region. The patterns generated with GS and AA contain a large amount of fluctuations within the measure region, which would definitely impact on any quantum behaviour of atoms loaded into these traps, as has been seen in atom-chip experiments [76, 145].

We have made the decision to use MRAF for all patterns of experimental interest, favouring accuracy over efficiency. In future, the other algorithms may prove to be useful for generating the discrete patterns at a higher efficiency, and GS can be used to modify the noise output of MRAF. Unless explicitly stated, in the remainder of this thesis the MRAF algorithm will be used. The authors of [143] noted in their
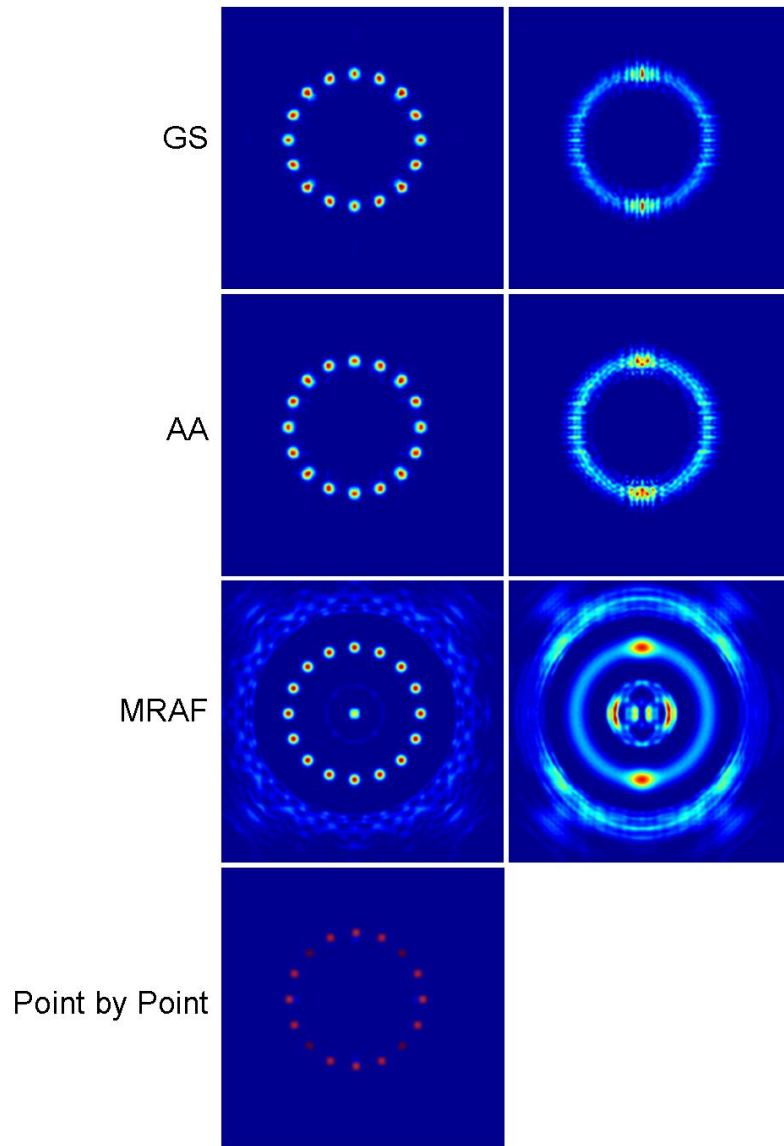
**Figure 4.17:** *Predicted outputs for the various methods discussed in the text. MRAF produces the most accurate and smoothest patterns, but does this at a cost of some light in the noise region.*

proposal of the MRAF algorithm that the only remaining hurdle in the creation of arbitrary holographic atom traps for cold atoms was experimental implementation, and in [144] demonstrated the difficulties in crossing this hurdle. In Sections 4.8 - 4.11 we show for the first time that this algorithm can, with some modifications, generate light patterns suitable for the trapping of ultracold atoms.

## 4.8 Initial Experimental Characterisation

To test our SLM's performance we initially use simple phase patterns of experimental interest which we generate using the point by point algorithm and directly load onto the SLM using the software and controller provided by BNS. To align the measured intensity to the target or predicted patterns, we use a simple grating to generate two diffraction-limited spots separated vertically in the output plane. In the computer, the positions of these spots are known, and they can be measured in the image acquired and offsets, rotations and stretching can be corrected for comparison. Figure 4.18 shows examples of test phase patterns and the corresponding light patterns as recorded by the CCD camera.
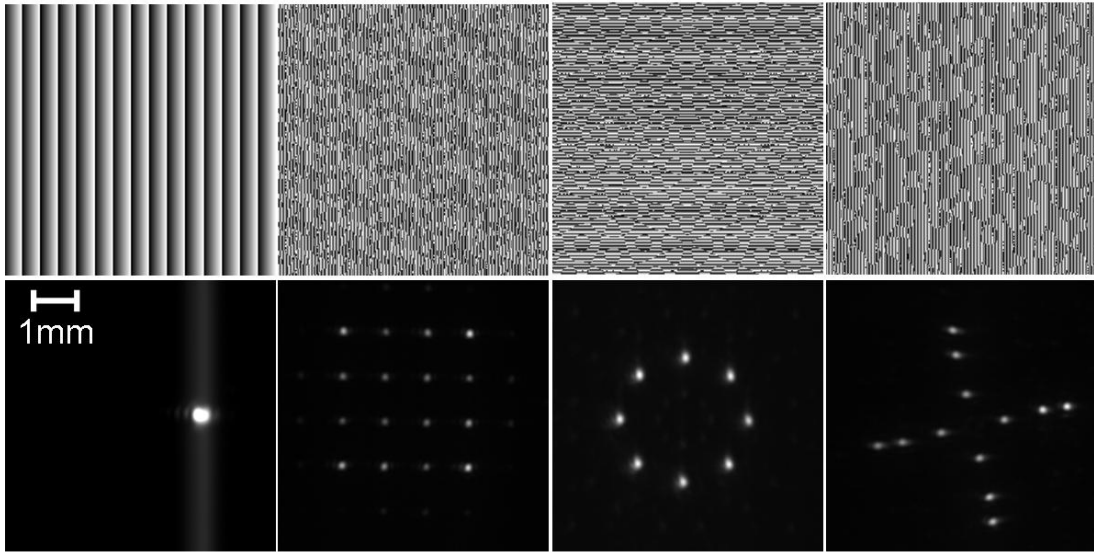


**Figure 4.18:** *Test phase patterns generated using the point by point algorithm (top) and the corresponding light intensity imaged using the CCD camera (bottom). From left to right the patterns show a single spot, a uniform square lattice, a ring lattice, and a series of 1D lattices.*

In order to test the suitability of these traps for ultracold atoms experiments, we measure the fluctuations in the power and position of a stationary single spot. This is the first diffracted order generated by the phase grating and has a $\frac{1}{e^2}$ waist of $w = 45\mu m$. As shown in Figure 4.19, the position is stable within $\pm 4.65\mu m$ ($\pm 1$ pixel), while frame-to-frame intensity fluctuations are within those of the illuminating laser, which are $\pm 0.5\%$, giving the same level of fluctuation in trap depth (1.25).
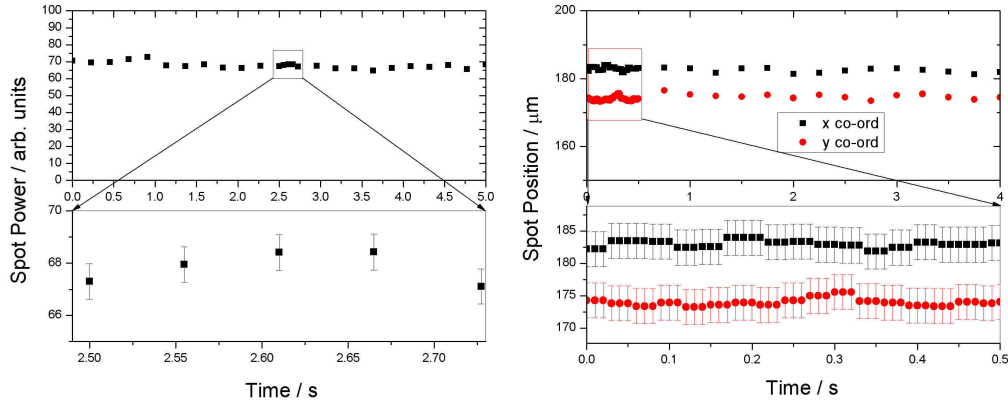
**Figure 4.19:** *For a stationary spot, the power fluctuates by $\pm0.5\%$, which is limited by the power fluctuation of the illuminating light. The position fluctuation is probably less than 5% of the spot diameter, but our resolution is restricted by the pixel size of the camera.*

Another feature we have characterised is that the diffraction efficiency of the SLM decreases as the separation between first and zeroth order is increased (as shown in Figure 4.20). Additionally, the width of single spots in the plane of the camera is found to increase with separation from the zeroth order. It is suspected that the width deviation is caused by the fact that the camera plane is flat and (ideally) parallel to the SLM surface, while the Fourier plane is in fact curved and parallel to the surface of the convex side of the lens. This results in a single image containing portions of the Fourier plane, and regions outwith the Fourier plane, which may be converging or diverging.

The point by point method suffers from several problems: inspection of the square lattice in Figure 4.18 shows that ensuring the spots have the same intensity is difficult, due to a combination of speckle-induced noise and the varying diffraction efficiency. Additionally, the appearance of "ghost" spots in the region of the programmed spots gives unwanted trapping potential and continuous traps are not possible without some form of time-averaging.

The phase patterns shown in Section 4.7.6 are sent to the SLM, and the results are shown in Figure 4.21. We find that the physical implementation of these CGHs using an SLM is susceptible to aberrations in the optical system and imperfect device response, thus introducing errors and roughness that were not present during the calculation.

However, we will show that this roughness can be reduced by incorporating the MRAF algorithm into a feedback loop.

As a last example of the flexibility of the MRAF algorithm in producing uncorrected output, and one which shows the full-speckle problem, we have generated a truly arbitrary pattern, shown in Figure 4.22.
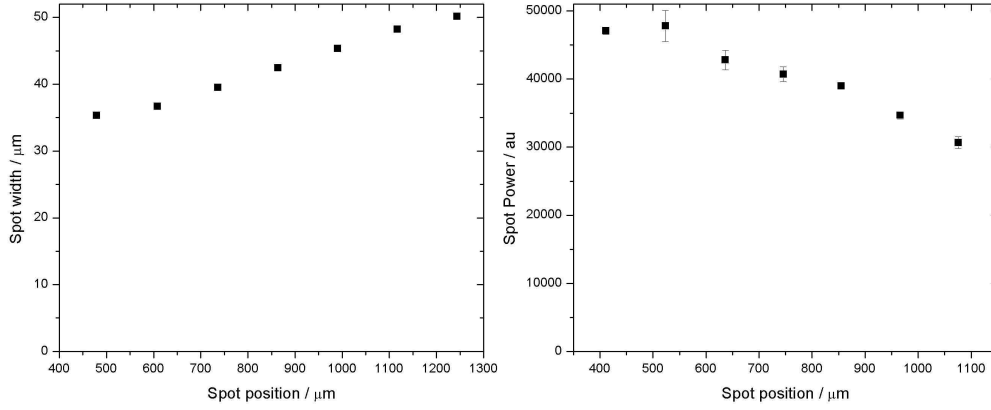
**Figure 4.20:** *As the spot moves away from the zeroth order, the power in the spot and the size of the spot change.*
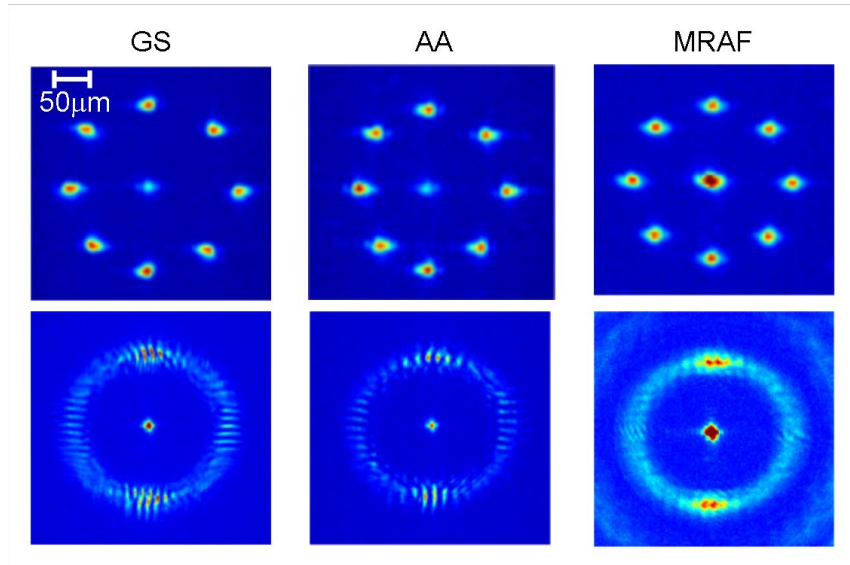


**Figure 4.21:** *The light patterns on the CCD camera when the phases of Figure 4.17 are sent to the SLM and illuminated. As with the predicted output, MRAF is more accurate than the other IFTAs. However, the continuous ring trap is severely fragmented, and would be incapable of coherent trapping of atoms.*
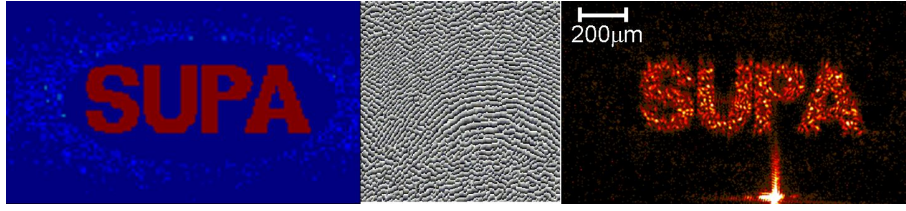
**Figure 4.22:** *MRAF computation (left) can create almost any pattern, although physical implementation (right) for flattop patterns contains a large amount of speckle.*

While the optical potentials shown in the preceding sections are exciting and varied, many are not suitable for the trapping of ultracold atoms due to intensity roughness. To overcome this, new methods are required.

## 4.9   Achieving Discrete Optical Traps Arrays

In order to create reliable output for cold atom traps, we have developed a new method based on feedback of the output light pattern into the calculation stage of the IFTA. Initially, we have created an algorithm to achieve this with discrete patterns.

To solve the problem of aberrations, we have designed a simple feedback algorithm, as shown in Figure 4.23. This algorithm uses the MRAF-generated phase as an input, which is sent to the SLM and the resultant light pattern in the Fourier plane is imaged. This output is analysed for accuracy, and a corrected target pattern is generated which compensates for discrepancies. This serves as the input for another iteration of the IFTA, and generates a new phase. The whole process is repeated until the output pattern is acceptable.

The first step in correcting the aberrations in the output is to detect how the light is distributed in the plane. We do this by finding individual spots and applying a two-dimensional Gaussian fit.

A spot finder has been created in MatLab. The image of the output plane is reduced in resolution by grouping the pixels into $3 \times 3$ sub arrays, in order to reduce the importance of small-scale fluctuations. Local maxima of this reduced array are found and the co-ordinates of these maxima within the higher resolution original image are returned (Figure 4.24). This gives the location of the spot only to an accuracy of $\pm 1$ pixels in each direction, which can be further improved if desired by searching for the maximum within the located $3 \times 3$ array. In order to locate further spots, the regions of the plane containing spots which have already been located are ignored.

Once the spots have been detected and a Gaussian fit performed, they must be compared to the corresponding spots in the original target. We analyse three properties of the spot in the $n$th iteration of the feedback loop, given by the Gaussian fit parameters: the spot intensity $h'(n)$, the $\frac{1}{e^2}$ waist of the spot $w'(n)$, and the position $(x'(n), y'(n))$ in the output plane. Primes denote properties in the output
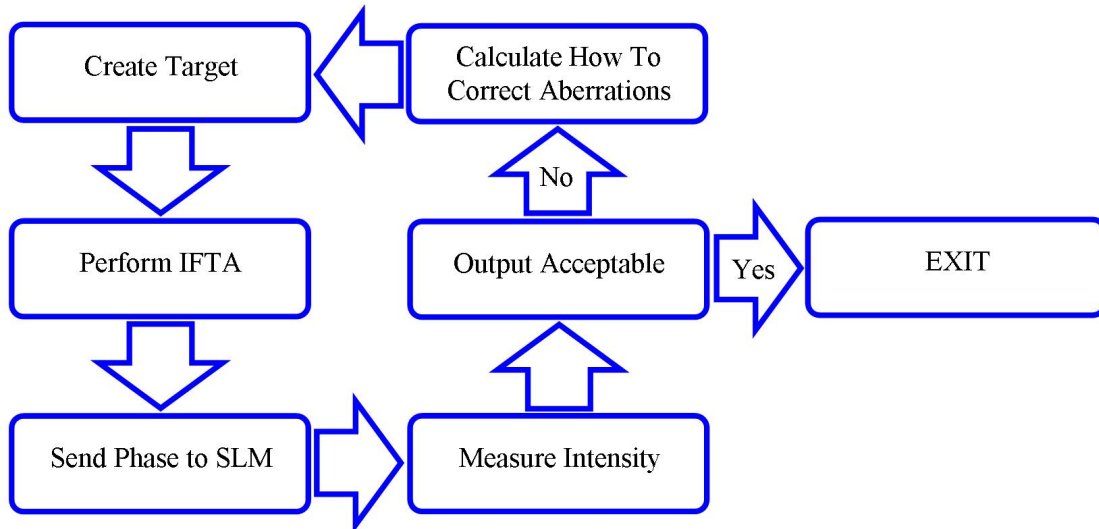
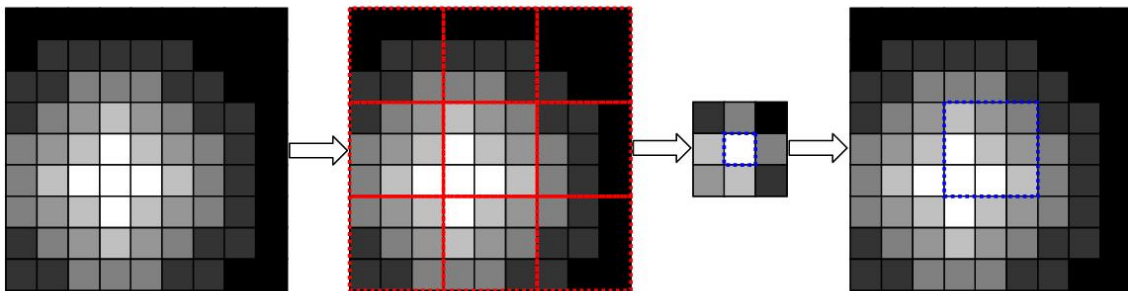**Figure 4.23:** *Block diagram of the feedback process.*



**Figure 4.24:** *The camera output is divided into $3 \times 3$ arrays, and the average value of each array is found and placed in a reduced resolution version of the output plane. The maximum value in this array is found, and this co-ordinate is returned to the main output. The method of breaking the array down helps the code to ignore random noise.*

pattern, whereas unprimed quantities are those in the target.

To create a new target (iteration $n + 1$), the properties of the spots are cumulatively varied depending on the results of the $n$th iteration. The transforms are given by

$$h(n + 1) = h(n) \times \frac{h(0)}{h'(n)}, \qquad (4.14)$$

$$w(n + 1) = w(n) \times \frac{w(0)}{w'(n)}, \qquad (4.15)$$

$$x(n + 1) = x(n) + x(0) - x'(n), \qquad (4.16)$$

$$y(n + 1) = y(n) + y(0) - y'(n), \qquad (4.17)$$

where $n = 0$ denotes the original target. The effect of the transforms is demonstrated pictorially in Figure 4.25.
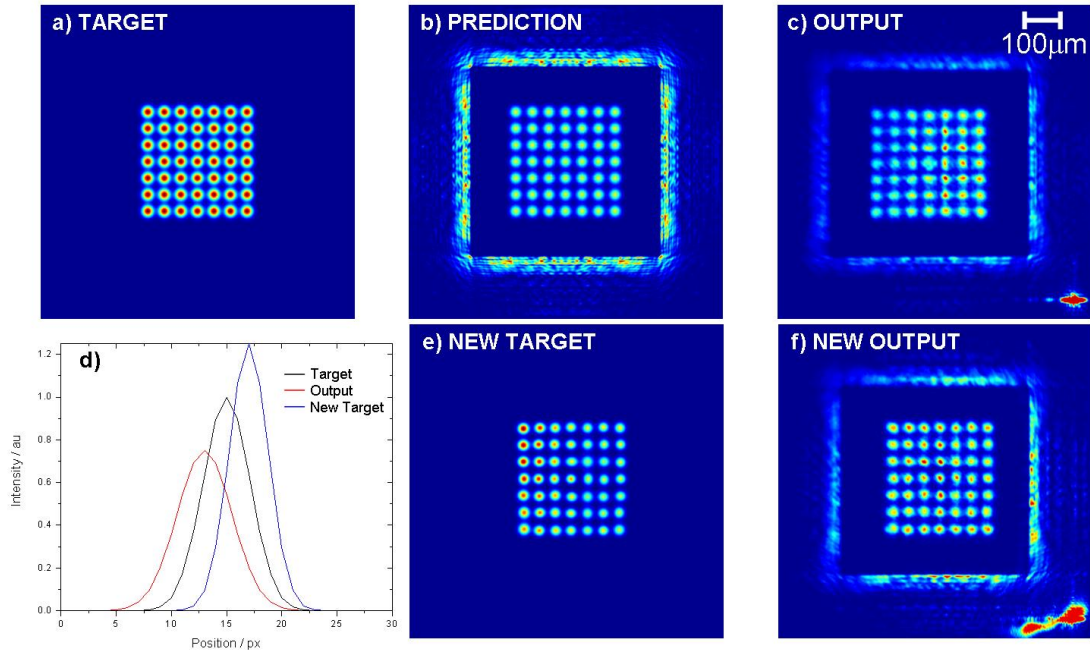


**Figure 4.25:** *The predicted output (b) for a uniform square lattice is very close (within the signal region) to the target pattern (a). The actual output (c) contains, however, many discrepancies. The measured spots of light are analysed and compared to the original target as in (d). If a spot is too faint, too wide and off-centre (red curve) compared to the target spot (black curve), it is made brighter, narrower and offset in the opposite direction (blue curve). Performing this analysis for every spot in the array leads to a new target (e). When the IFTA is performed again and the phase output on the SLM, the new output (f) is much closer to the desired pattern (a).*

Measurement errors restrict the accuracy that we can hope to achieve with the feedback process. We find that the Gaussian fit function within MatLab predicts

the intensity with an uncertainty of $\pm 3\%$, so we build a tolerance into the feedback mechanism. If the spot intensity is within 3% of the target, it is not corrected in the current iteration of feedback.

We find that within 10 iterations, the feedback algorithm significantly improves the quality of the light pattern. Figure 4.26 shows the progression of the standard deviation and the range of spot brightness within a square uniform array.
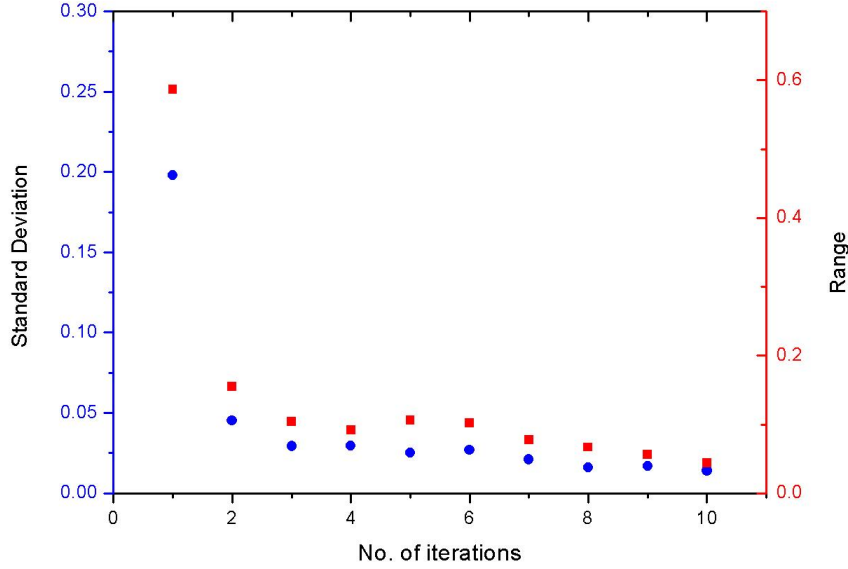


**Figure 4.26:** *The standard deviation and the range of spot intensities within a uniform square lattice are seen to improve to within our tolerance of 3% within 10 iterations of feedback.*

To show the flexibility of our method, we demonstrate a number of interesting optical traps that are possible. For all patterns of interest, the pattern quality is seen to improve beyond the initial MRAF output. The images in these sections show only light in the measure region, for clarity.

The standard deviation of most initial patterns is around 20%, but is reduced to within our tolerance value of 3% using the feedback algorithm. The spot widths do not require a high degree of correction, unless feedback is applied only to the spot heights, in which case large spots can occur. Spot position discrepancies tend to be small compared to spot size and are corrected within one feedback iteration.

As discussed in Sections 1.2 and 1.7, there is great interest in the behaviour of cold atoms in optical lattices. To achieve a closer analogy between cold atoms and electrons in metals, the spatially-varying chemical potential in the Hubbard Hamiltonian can be removed if uniform square optical lattices are used. These are now easily created using our feedback method, as demonstrated in Figure 4.27.

These lattices are completely controllable and individual sites can be manipulated. For example, we remove every second lattice site in a checkerboard pattern. To show the flexibility in generating lattices with modulated intensity across the lattice, we take inspiration from experiments proposed in [146]. This novel trapping potential was proposed to confine atoms within an optical lattice by decreasing the

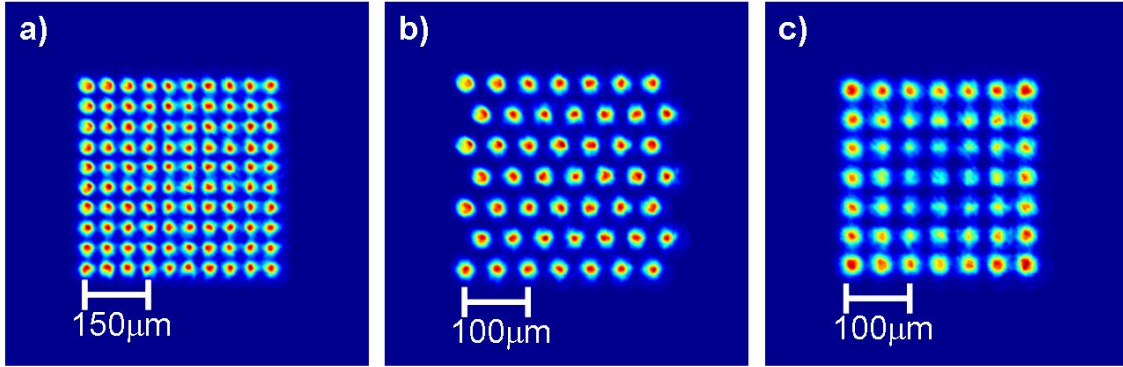tunnelling matrix element toward the edge of the lattice.



**Figure 4.27:** *Light pattern images acquired with CCD camera. a) Uniform square lattice b) Checkerboard lattice c) Tapered lattice.*

This control over individual lattice sites may be used in future to controllably study disorder effects in optical lattices, such as the Anderson localization effect [33, 34].

One of the current goals in the field of ultracold atoms is the achievement and investigation of the transition to an antiferromagnetic ordered state. The low temperatures required to enter this phase are, at present, beyond the reach of experiments (we note the success of an alternative strategy to model this phase [30]). New cooling schemes to reach lower temperatures have been proposed using tailored optical lattices to divide the atoms into different lattice regions [147].

One major advantage of cold atom experiments is the control of dimensionality that is afforded by flexible trapping potentials. In particular, 1D lattices present popular experiments as the models of these systems tend to be exactly solvable [148].

Using holography, it is possible to create a type of 1D lattice that is impossible with standard interference methods: a ring lattice (Figure 4.28). This infinite length lattice with periodic boundary conditions is also useful if it is to be used with any underlying cylindrically symmetric trap, as lattice sites can be placed on an equipotential, once again negating the influence of the spatially-varying chemical potential in the Hubbard model.

These ring lattices have been the subject of a number of recent proposals for generating excited states of fixed angular momentum [149], and for quantum information processing with Rydberg atoms [150].

There are a vast range of theoretical proposals for experiments in cold atoms in non-trivial optical lattices, including those with a bow-tie [151], hexagonal [152] or superlattice structure [39].

To further push the flexibility of our apparatus, we decide not to restrict ourselves to discrete arrays of optical traps, and develop a method for arbitrary continuous traps.
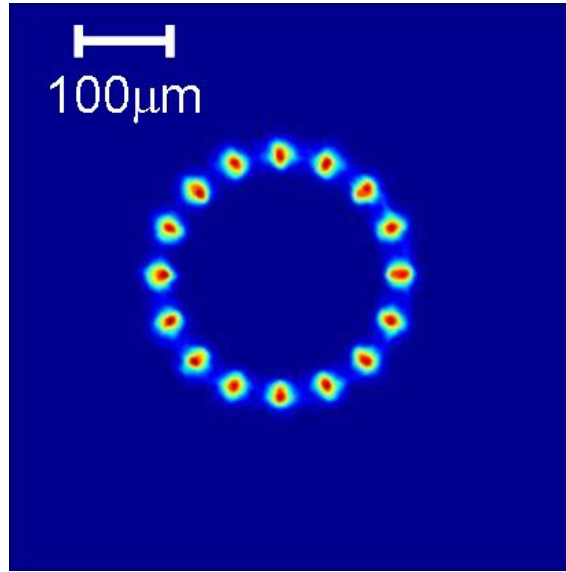
**Figure 4.28:** *An infinite length, one-dimensional optical lattice (or a 16-spot ring lattice with periodic boundary conditions).*

## 4.10 Achieving Continuous Optical Traps

Whilst the technique to create accurate, arbitrary optical lattices is impressive, in order to work with these lattices in the Hubbard regime a large NA optics system such as the one used by the authors of [127] and [128] is required. Additionally, there are many experiments in cold atoms that could be performed on arbitrary continuous patterns. The feedback method developed above is not obviously extendable to continuous patterns, but the following sections will demonstrate how we accomplish this and introduce the areas of application for some continuous patterns.

By enclosing the MRAF algorithm in a similar feedback loop to the one we have used for the discrete patterns, we have been able to smooth the intensity profile at the trap location. The MRAF algorithm is performed as before, and the calculated phase pattern is again sent to the SLM and the light is imaged using the CCD camera, so that the achieved intensity profile can be compared to the target. Any discrepancies are used to redefine the target for the next iteration of the IFTA. The key difference here is to make the algorithm more general, without the need for the Gaussian fit and the spot-finder.

To do this, consider the example of the Gaussian ring with two bright spots, as reshown in Figure 4.29. The output of the MRAF algorithm within the measure region is compared to the original target by means of a subtraction, to find a discrepancy. This discrepancy is then simply added onto the target of the previous iteration, and the IFTA run once again.

After a few iterations of this feedback loop, the measured light profile shown in Figure 4.30 improves its accuracy compared to the original target. The intensity of light around the trapping minimum of a section of the ring is measured by integrating over the pixels within a small angle, and plotted in Figure 4.30c).

Equation (1.25) shows that any local roughness in the intensity of the light pat-
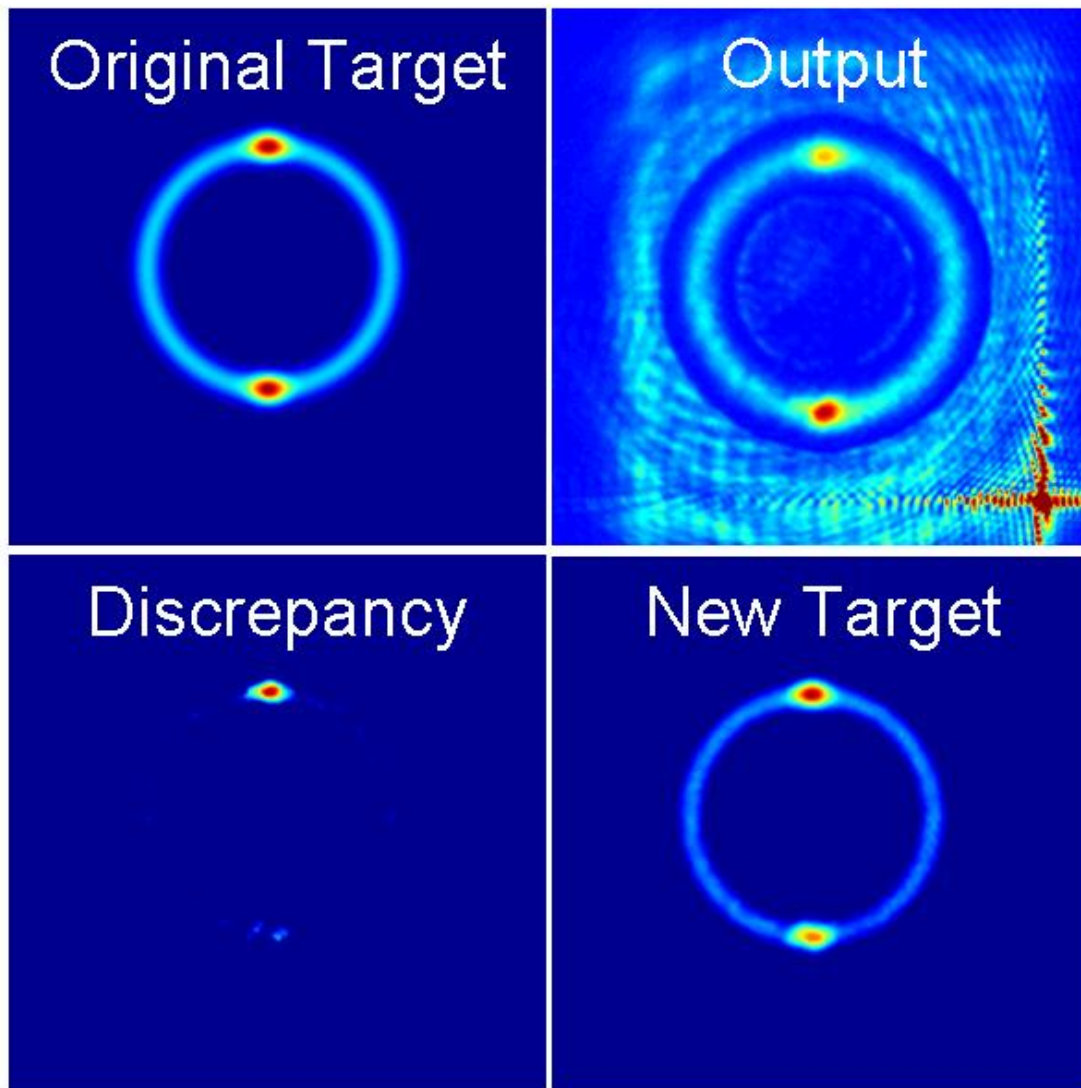
**Figure 4.29:** *Feedback algorithm for continuous patterns. Within the measure region, the output is subtracted from the original target to give a discrepancy. This is added onto the target of the previous iteration to form the target for another iteration of the IFTA.*
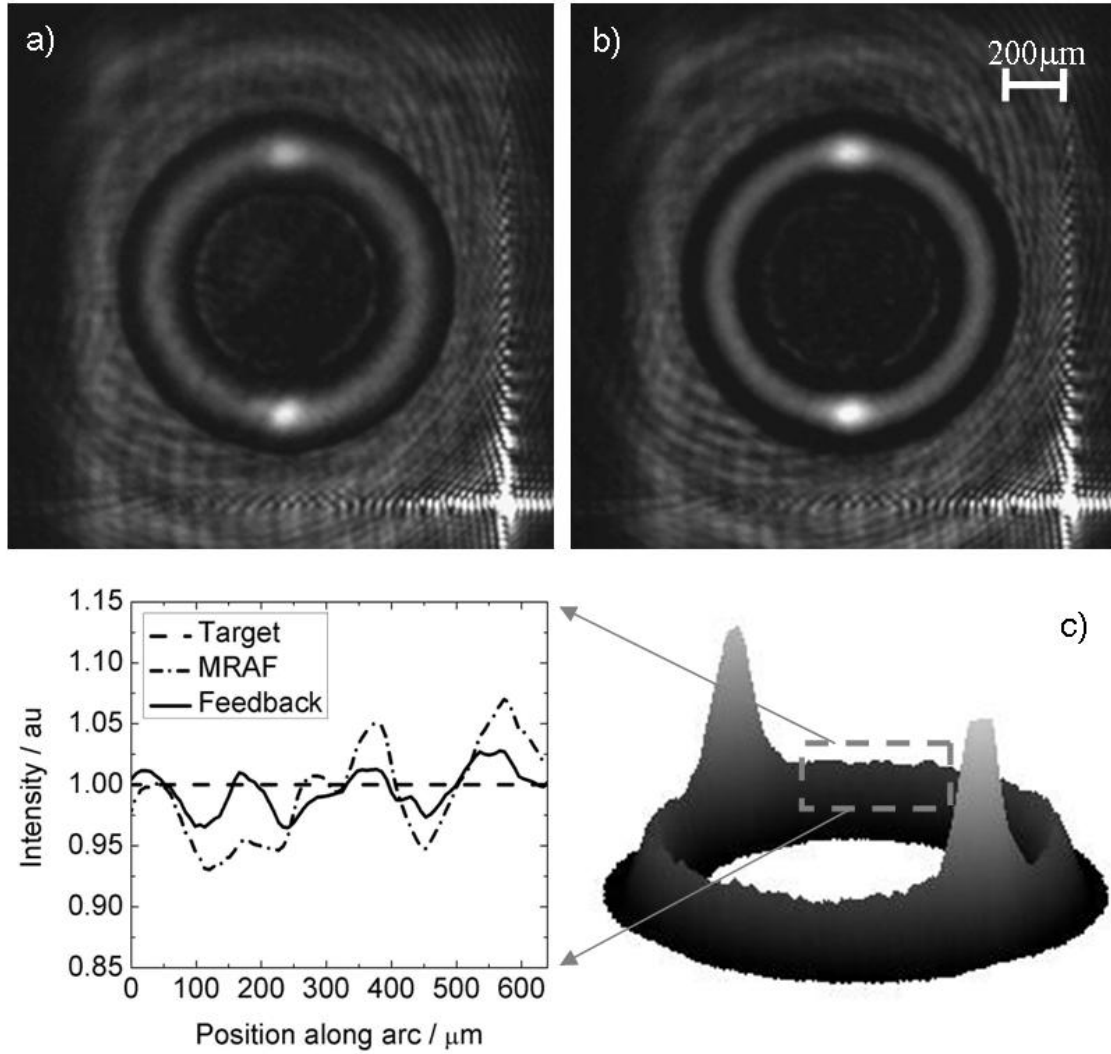
**Figure 4.30:** *a) Initial output of MRAF algorithm. The bright cross at the bottom-right of the image is zeroth order of diffraction by the SLM. b) Light intensity after seven iterations of the feedback loop. c) The final light intensity within the ring portion of the trap (solid line) is significantly smoother and more accurate than the initial output (dash-dots). The desired intensity distribution is shown (dashed) for reference.*

tern creates a varying energy landscape, which could cause heating or fragmentation of the atom cloud. Our feedback loop reduce the rms error from 8.48% to 3.88% at the minimum of our optical trap.
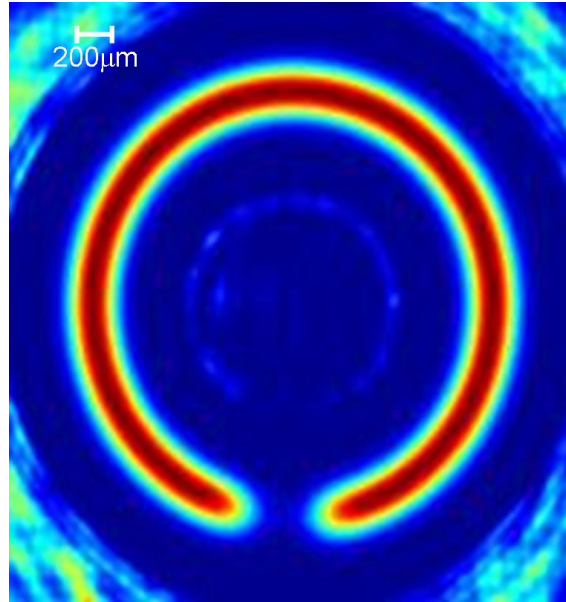


**Figure 4.31:** *A ring with a tunable weak link for the observation of Josephson oscillations.*

One possible extension of the ring trap idea is to evolve the rotating trap into a ring with a weak link, and watch Josephson oscillations of the cold gas across the barrier, in an analogue of a Superconducting Quantum Interference Device [23]. This system is also expected to exhibit macroscopic two-current states [153] and to provide a cold atom qubit candidate [40].
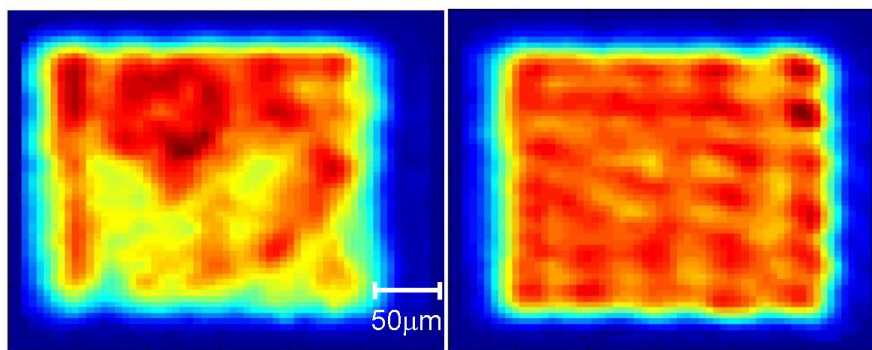


**Figure 4.32:** *Top-hat trapping potential improvement from (left) 24.8% rms error to (right) 8.8%. The remnant noise in the measure region is correlated to the initial guess at the start of the IFTA.*

A light pattern of particular interest is the "top hat": a region of uniform high intensity, falling off rapidly to zero intensity elsewhere. Although this target is

straightforward to define, the MRAF algorithm is incapable of generating a prediction with under 10% error using our current guess methods. This is probably limited by the Fourier frequencies available on a pixellated, finite-size array: sharp edges require very high spatial frequencies in Fourier space. The authors of [154] have identified that the FFT is not sufficient to model the propogation of light in the system, and showing that the Helmholtz equations at least predict the rough features seen within the flat-tops. Our most successful attempts were with high-order superlorentzian functions, as shown in Figure 4.32, and the feedback algorithm improves the rms error within the flat-top from 24.8% to 8.8%. This problem is a popular one in optical physics, with current limits restricted to the level of around 1% in the flat-top [155].

As shown in Figure 4.33, we have proved the flexibility of our feedback method by creating a square barrier (which can be thought of as a dark flat-top beam). This could be used in the lattice-separating schemes mentioned in Section 4.9.
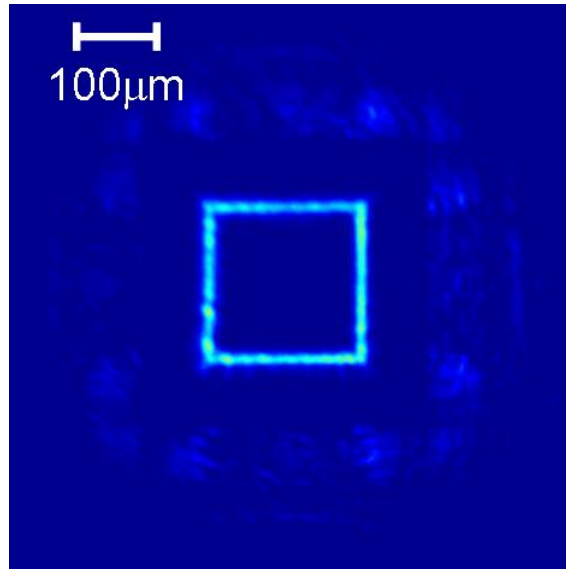


**Figure 4.33:** *A square continuous optical potential, which could be created with blue-detuned light and superimposed on an optical lattice as a barrier.*

A different family of potential of interest is the multi-well trap, such as the controllable double-well in Figure 4.34, which has a non-zero intensity between the two trapping minima. Such multi-well potentials provide an excellent testing ground for fundamental quantum mechanics and appear regularly in theoretical investigations. This example also provides a very visual demonstration of the ability of our algorithms to "clean" the original output into a much more accurate representation of the desired optical trap.

Additionally, we have generated power-law optical traps, which will be discussed in detail in Section 4.13.
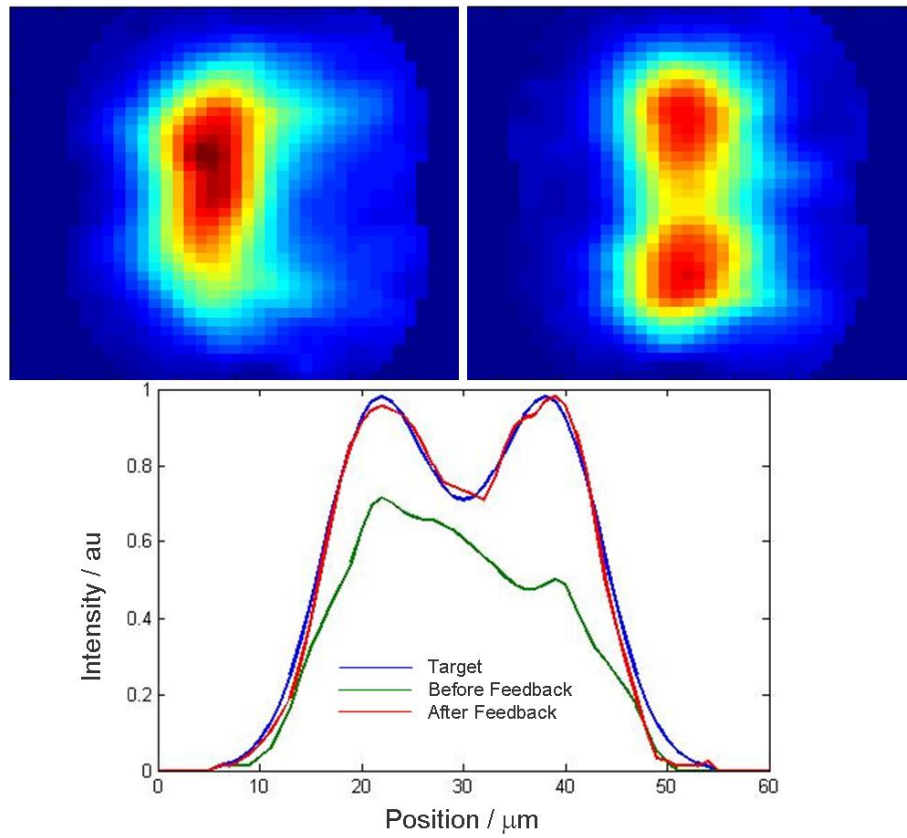
**Figure 4.34:** *A controllable double-well potential before and after feedback.*
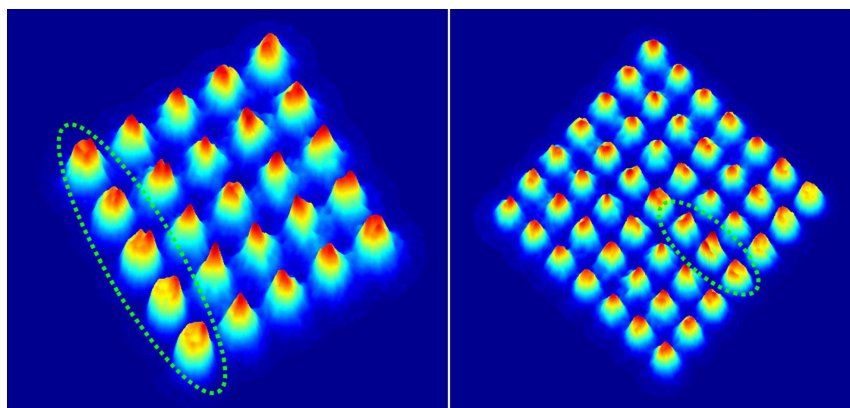


**Figure 4.35:** *When generating discrete patterns, double-wells can be formed rather than single Gaussians. These are not detected by the discrete feedback algorithm in its present form.*

# 4.11 Limitations of the Feedback Algorithms

On some occasions, the effect of the feedback algorithm can be limited due to unusual effects in the output pattern. For example, the discrete patterns can include double-well spots (these are artifacts from the guess phase), which are not detected using the Gaussian fit (see Figure 4.35).
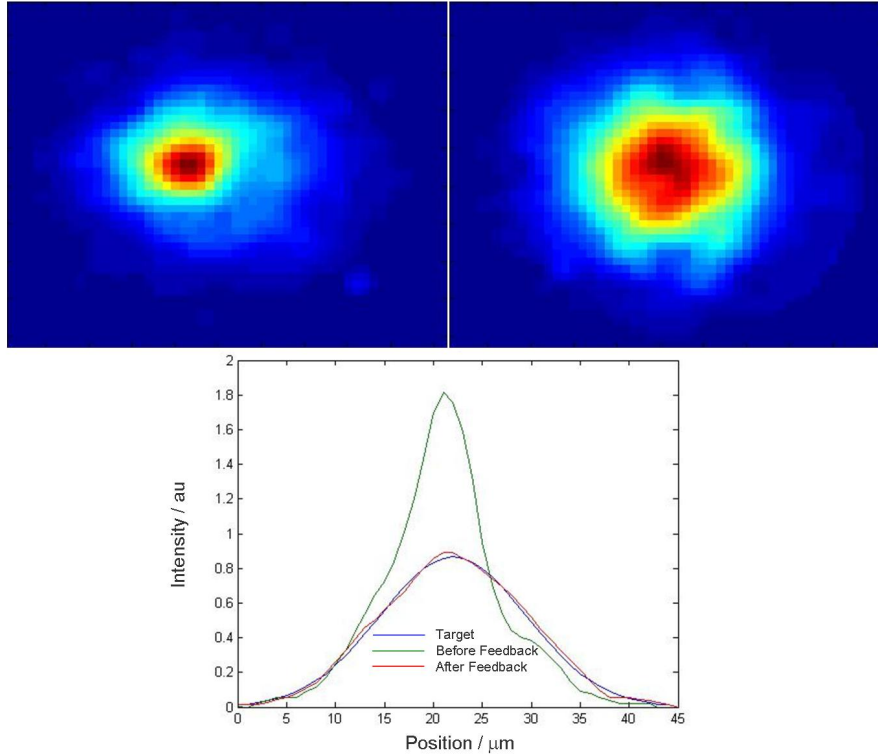


**Figure 4.36:** *The aberrations associated with the discrete feedback method can be overcome using the continuous feedback method. A single Gaussian spot is corrected to match the target.*

These effects should be remedied by using the method of the continuous feedback for discrete patterns. At present, this has not been attempted due to technical difficulties arising when the intensity in the measure region approaches zero (which does not happen in the continuous patterns). We have, however, demonstrated that we can correct individual aberrated Gaussian spots, as shown in Figure 4.36.

For the ring trap of Figure 4.30, the predicted rms error is 0.6% but the feedback-enabled output has an rms of 4%. The feedback algorithm accuracies are presently limited by detection issues. A more reliable and sensitive probe of the light will be possible by using the atoms. As experiments with cold atoms are carried out under vacuum, the windows of the vacuum system will themselves introduce aberrations which would not be accounted for by the feedback loop in its present form. However, atoms are a very sensitive probe of roughness of the trapping potential, so we envisage continuing to use the feedback loop by taking *in situ* images of the trapped atoms rather than directly imaging the light profile [156], and use these

images within the feedback loop.

A further limitation to the use of these light patterns is the diffraction limit, which will impede attempts to place lattice sites sufficiently close to one another in order to enter the Hubbard regime where macroscopic tunnelling is possible. However, the advances of [127] and [128] show that such experiments could be performed in future.

## 4.12 Dynamic Optical Traps

In order to use holographically generated light patterns to *dynamically* trap and manipulate ultracold atoms, the variation of the pattern must be fast compared to the lifetime of the cloud. Additionally, the evolution of the trap must be very smooth, i.e. there should not be large "flicker" between consecutive patterns.

We tested our SLM by characterising the dynamic performance of our light patterns in terms of intensity stability, and inter-frame flicker, initially using the point by point programming method to move one spot around the output plane.

By changing the periodicity of the hologram, the spot was propagated by $200\mu$m in the $x$-direction in one hundred equal steps. The position of the centre of the spot is monitored to check the pointing stability and the intensity of the spot as a function of time gives an indication of the flicker (see Figure 4.37). The spot centre is found to fluctuate by $\pm 2$ pixels, for a spot measuring 40 pixels (FWHM).
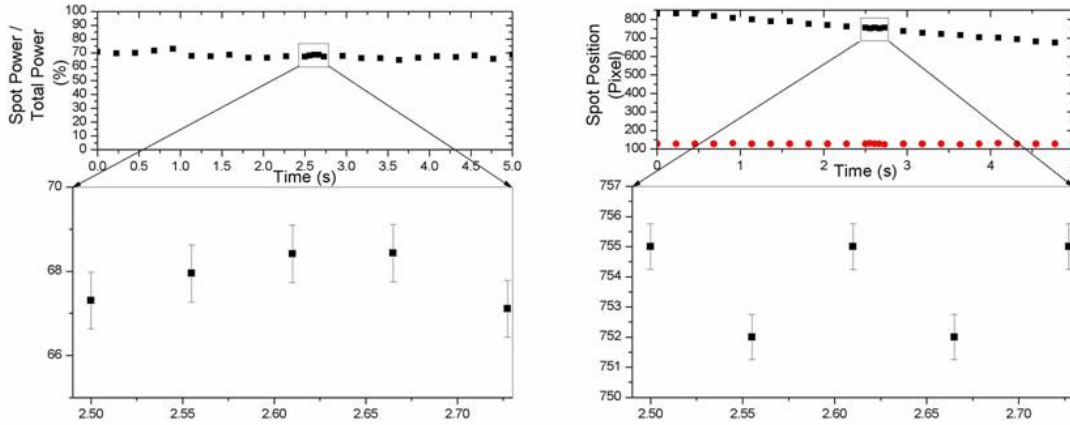


**Figure 4.37:** *A single spot is moved in steps of* $0.2w$, *where* $w$ *is the width of the spot. (left) The intensity between frames changes by a maximum of* $0.5\%$, *which is also the maximum intensity variation of the laser before the SLM. (right) After factor 4 magnification, the spot position can change by 4 camera pixels from shot to shot.*

The flicker measurement was also repeated using the fast photodiode. Due to the small surface of the photodiode and the magnification, the range of spot position was restricted to $2w$. When traversing this distance in ten steps of $0.2w$ or in 100 steps of $0.02w$ no appreciable flicker is detected. For a $2w$ jump (cycled at 1 Hz) we

measured a glitch in the signal at the time of going from one position to another of about 17.5% of the total DC value, meaning that dynamic traps for ultracold atoms are possible, provided the pattern evolves smoothly.

## 4.13 Power-Law Optical Trap

In this section, I introduce our novel method for achieving quantum degeneracy in a dynamic Power-law optical trap.

### 4.13.1 Production of Power-Law Potentials

Using the MRAF algorithm and our SLM, we can create arbitrary light patterns, including power-law intensity distributions $I(r)$ of order $\alpha$:

$$I(r) = \begin{cases} I(0)\left[1 - \left(\frac{r}{r_0}\right)^{\alpha}\right], & r \leq r_0, \\ 0, & r > r_0. \end{cases} \tag{4.18}$$

Atoms in this light field will, via the AC-Stark effect, experience a conservative trapping potential for $r \leq r_0$:

$$U(r) = A\left(\frac{r}{r_0}\right)^{\alpha}, \tag{4.19}$$

where $r_0$ is the trap radius and

$$A = \frac{3\pi c^2 \Gamma I(0)}{2\omega_0^3 |\delta|} \tag{4.20}$$
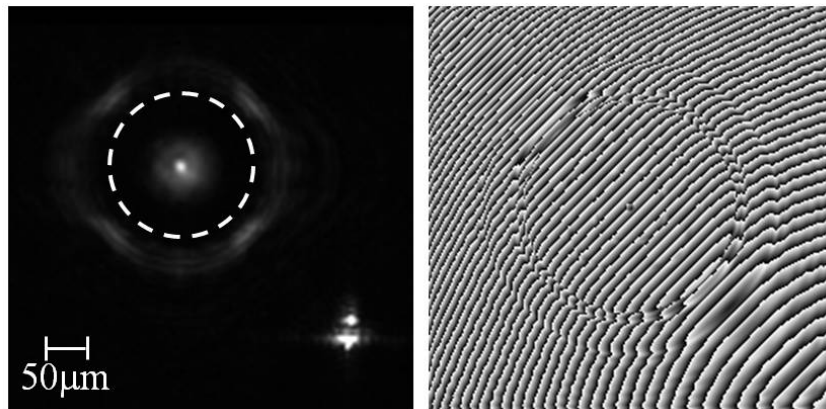
the trap depth [61].



**Figure 4.38:** *Left: Power-law beam of order 2 with signal region highlighted by dashed lines. Right: Phase pattern which gives the power-law beam.*

While the MRAF-optimised phase pattern does not always produce an accurate intensity pattern when applied to a physical device and feedback can be required,

for the case of simple power-law intensity distributions we have found that the output is smooth and accurate. In particular we have generated power laws with $\alpha$ ranging between 2 and 0.5. Figure 4.38 shows the light pattern in the output plane as detected by the CCD camera, while Figure 4.39 shows the intensity profiles of $\alpha = 2$ (parabolic) and $\alpha = 0.5$ distributions. At fixed order, we have also varied the radius $r_0$ between 27 $\mu$m and 103 $\mu$m. The size of the signal region is chosen so that the uncontrolled intensity in the noise region is well separated from the power-law pattern. This minimises the effect of the noise region on atoms loaded in the power-law trap.
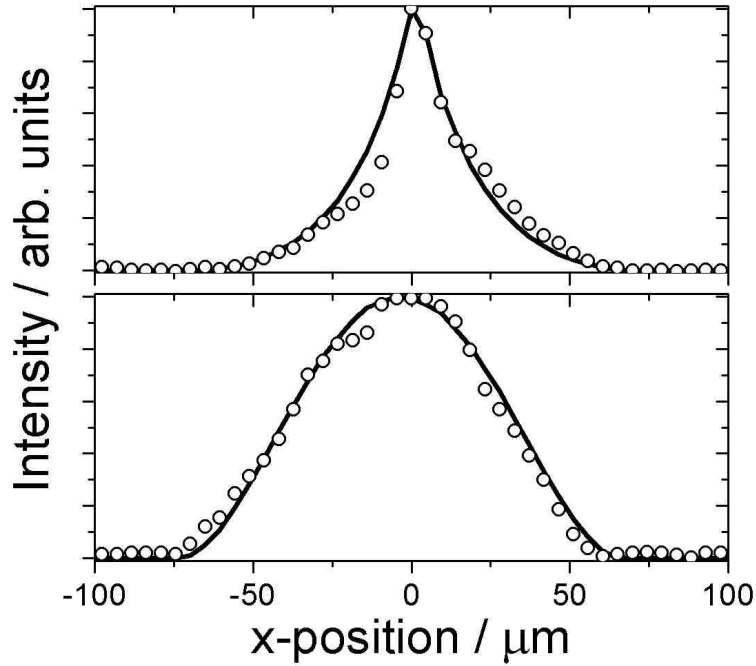


**Figure 4.39:** *Profiles of power-law intensity distributions with $\alpha = 0.5$ (top) and $\alpha = 2$ (bottom). The measured curves (open circles) are extracted from images such as the one shown in Figure 4.38, while the predicted curves (solid lines) are determined by the MRAF algorithm.*

### 4.13.2   Off-plane pattern

For the optical patterns presented here to be suitable for 3D trapping of cold atoms, we need to know how the patterns vary out of the Fourier plane. To do this we move the camera on a translation stage away from the SLM. We move $300\mu$m out of the plane and find that the pattern broadens from a $1/e^2$ waist of $96\mu$m to $101\mu$m, while the beam profile does not vary significantly, as is shown in Figure 4.40.

This $300\mu$m distance is greater than the width of all the power-law distributions we realised, hence two perpendicular power-law beams, each tailored by an SLM,

**Figure 4.40:** *Moving the camera away from the SLM, we investigate the dispersion of our simple optical patterns. The pattern does not change from the profile required, but does broaden by 25% over 300µm translation.*

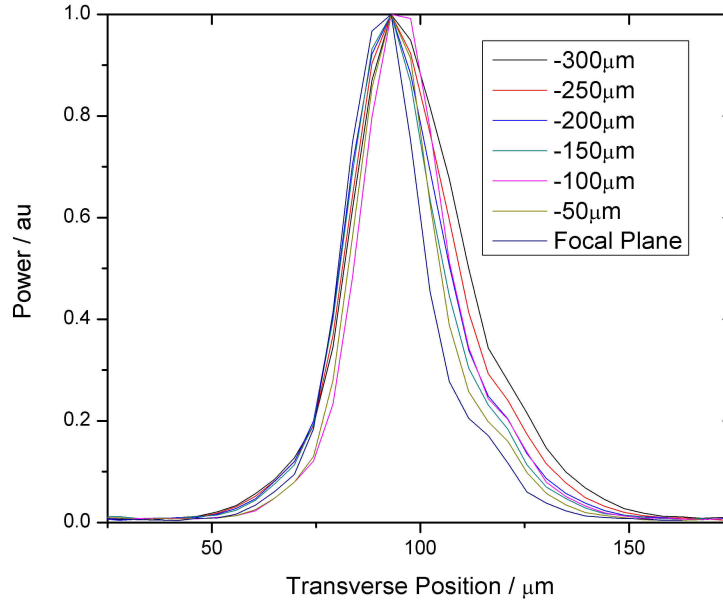can provide three-dimensional confinement. Alternatively, a light sheet can be used to add confinement along the axis of the SLM beam.

### 4.13.3  Power Variation

As the optical trap depth will depend on laser power, it is important that we know how both the peak power and the total power in the optical trap evolve during any variation of the pattern.

Our first approach is to program patterns with different $\alpha$ which all have the same width $w$. We apply the MRAF output to the SLM and illuminate with a constant laser power. We measure the power in the first order using our CCD camera while we vary the beam order. As is shown in Figure 4.41, the peak power (trap depth) increases as we lower the order of the power-law trap, which can be understood if one considers the integral of the beam profile over the plane. Encouragingly, when the mixing parameter is kept constant and the beam order is varied, the total power in the first order remains constant. This result allows us the flexibility to keep the trap depth constant by varying the laser power, as shown in Figure 4.42. This can be achieved in an experiment by passing the laser beam before the optical fibre through an AOM and varying the attenuation, as in Section 2.3.3. By varying the total power in a linear fashion, we can keep the peak power constant as the power-law is changed. We can, in fact, keep the peak power constant across all the mixing parameters used in this diagnosis, allowing us more flexibility in creating sequences. If we find that different mixing parameters gives us higher-quality optical traps for
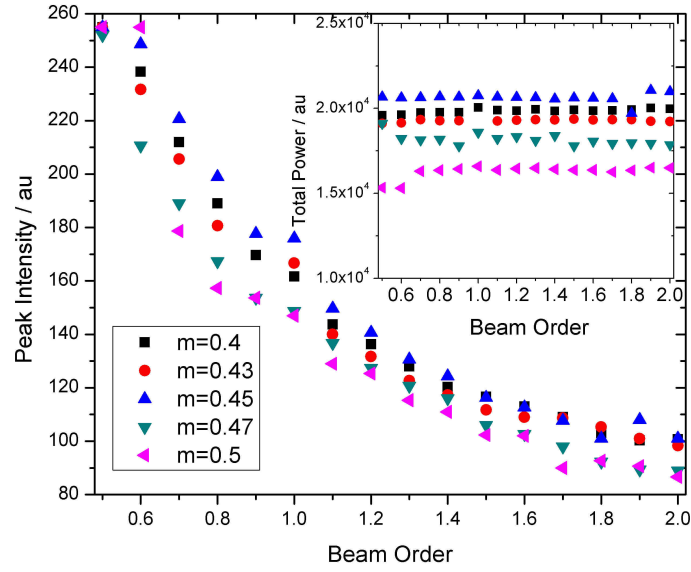
**Figure 4.41:** *Variation of peak power and total power versus power-law when the illuminating laser power and the pattern width are kept constant. As expected, the peak intensity, and thus the trap depth, increases as the power-law decreases. The total power in the first order remains constant.*



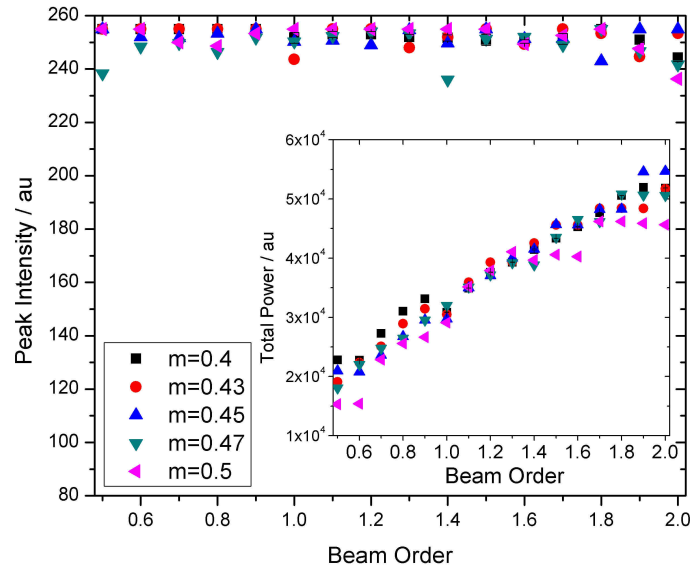**Figure 4.42:** *Variation of peak power and total power versus power-law when the pattern width is kept constant but the illuminating laser power is varied. The trap depths can be kept constant as the mixing parameter and the beam order are varied by adjusting the laser power.*

different beam orders, we can compensate the loss of power from the measure region by varying the laser power.
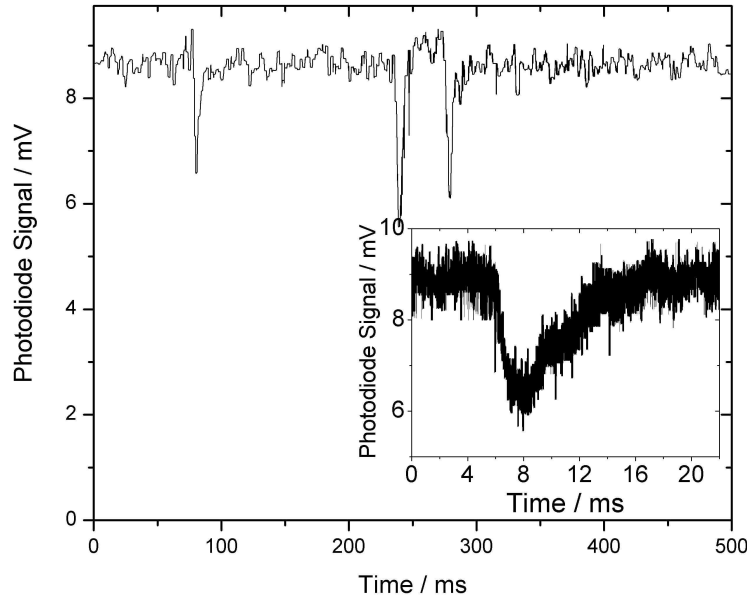
### 4.13.4   Dynamic Manipulation



**Figure 4.43:** *The outset shows a sequence moving from beam order 0.5 to beam order 2 in steps of 0.1, with the light being collected by a photodiode. Beam orders 0.5 and 1 are calculated using a different phase guess, and we can see that the light level flickers during the transitions between one of these holograms and any of the others. During transitions between any of the other beam orders, however, the optical power remains constant. The inset shows one of these flickers enlarged.*

In moving from one optical pattern to the next, it is important that the optical trap depth is accurately controlled during the transition of the liquid crystals of the SLM. The authors of [137] noted that in a ferroelectric SLM substantial flicker between frames can occur due to changes in the state of individual pixels. We find that this problem also exists in our nematic liquid crystal SLM, but can be solved by careful implementation of the MRAF algorithm.

To achieve dynamic power-law optical traps, we apply a sequence of phase patterns producing power laws with $\alpha$ going from 0.5 to 2 in steps of 0.1 at 25 Hz. We run a test sequence in which the patterns for beam order 0.5 and 1 were calculated separately to the others, using a different phase guess. The first diffracted order is separated from the other light and collected by a photodiode. As can be seen in Figure 4.43, we do see flicker when transforming between traps generated using different guess phases, but in the main see no flicker. Additionally, changing the phase pattern between beam order 1 and beam order 0.5 directly gives no flicker.
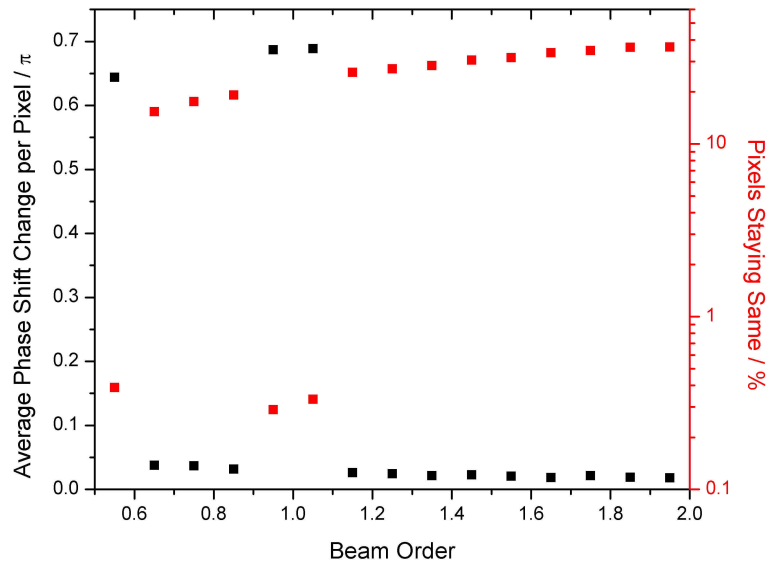
**Figure 4.44:** *While the SLM changes between phase gratings with the same initial conditions, over* 10% *of the pixels remain constant, and the mean change in the phase shift per pixel is around* $\frac{\pi}{40}$. *However, changing to the phase gratings calculated with a different phase guess causes far fewer pixels to remain the same, and the average change of the phase shift to be much greater.*
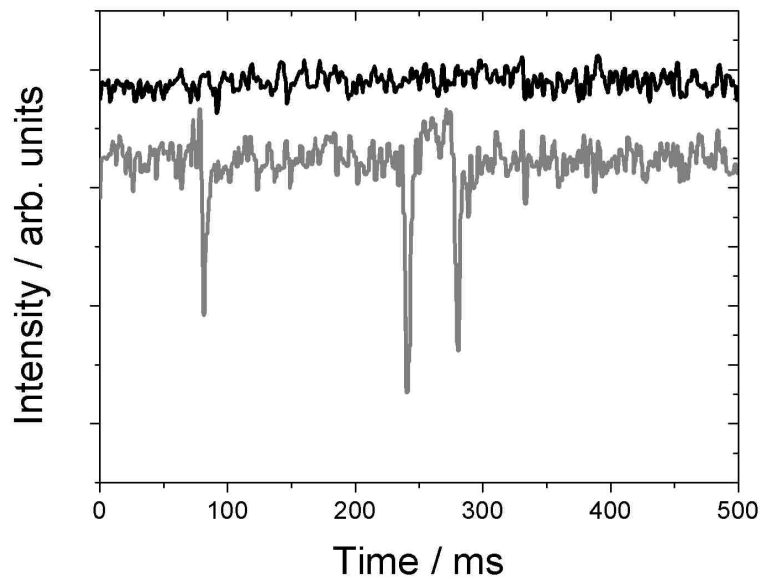


**Figure 4.45:** *Substantial flicker can occur as the SLM switches between patterns (lower trace, duplicated from Figure 4.43). By minimising the level of phase change per SLM pixel, this flicker can be removed (upper trace - offset for clarity).*

We find that when transferring between two power-law traps generated with the same guess phase, the average phase change per pixel is $\frac{\pi}{40}$ and on average 72% of the pixels change their retardance. However, in transferring between two power-law traps generated with a different guess phase, the average phase change increase to $\frac{2\pi}{3}$ and 99.7% of the pixels have to change their retardance (see Figure 4.44).

To overcome this, the retardation patterns are recalculated using the same guess phase for all orders. This results in a sequence in which 70% of pixels change their phase shift at each step, but only by $0.025\pi$ on average. As shown in the upper trace of Figure 4.45, we can no longer measure any flicker between consecutive patterns.

## 4.14 Quantum degeneracy in a power-law optical trap

### 4.14.1 Adiabaticity Conditions

In the previous section, we showed that the size and order of a power-law trap can be dynamically varied by refreshing the phase pattern on the SLM. Moreover, the trap depth can be controlled by varying the optical power illuminating the SLM. This gives full flexibility in designing sequences. How fast a sequence can then be implemented is limited by the requirement that changes in the trapping potential must be slow compared to the thermalisation time of the trapped atoms, which is determined by the elastic collision rate. Additionally, changes must be slow with respect to the motion of the atoms in the trap. In the case of a harmonic trap characterised by a frequency $\omega$, any compression or expansion of the trap must satisfy $\frac{\mathrm{d}\omega/\omega}{\mathrm{d}t} << \omega$ [157].

Similarly, in our generic power-law trap such an adiabaticity condition can be formulated for each of the three parameters (radius, depth and order), given that they can be varied independently. The condition therefore is that the relative change of a parameter per unit time be much less than the characteristic oscillation frequency of an atom in the trap. For the traps considered in this work, this is of the order of $\sqrt{A/m}/r_0$ where $m$ is the atomic mass [158]. Hence the adiabaticity conditions can be written as:

$$\frac{\Delta k/k}{\Delta t} \ll \frac{1}{r_0}\sqrt{\frac{A}{m}}, \tag{4.21}$$

where $k = A, r_0, \alpha$. The SLM can vary $\alpha$ and $r_0$ in small but discrete steps, and it takes $\Delta t \approx 10$ ms to change from one pattern to the next, as estimated by the duration of the flicker shown in Figure 4.43. For the transformations considered below, $\Delta\alpha = 0.1$, $\Delta r_0 \leq 3$ $\mu$m, and the characteristic oscillation frequencies are several kHz. These parameters ensure that (4.21) is satisfied for $k = r_0, \alpha$. The trap depth on the other hand can be varied continuously, hence $\Delta A$ can be taken as the total change over a sequence, and $\Delta t$ as the total duration of that sequence. We expect the evaporative cooling sequence and the adiabatic transformation described below to last about one second, for which (4.21) is satisfied.

### 4.14.2 Evaporative cooling sequence

We assume that two power-law beams are crossed to form a three-dimensional trap. We assume for simplicity that this trap is spherically symmetric (which can be realized by modifying the aspect ratio of the light distributions shown in Section 4.13.1), but our results are also valid in the case of asymmetric traps as long as the trap order is the same in all directions.

As for any all-optical scheme, our approach is suitable for all internal states, atomic mixtures and molecules. Laser-cooled atoms from a MOT can be captured into a broad (radius $r_0 = 50~\mu$m), 910 $\mu$K deep parabolic ($\alpha = 2$) optical trap. This is the deepest trap shown in Figure 4.46. Following (4.18) and (4.19), an optical power of 14 W in each beam is needed for such a trap at a wavelength of 1060 nm.

From experiments in which similar conditions have been realized in practice [98], we take as our starting point $N = 3 \times 10^5$ atoms with a temperature $T = 91~\mu$K, resulting in a phase-space density $D = 10^{-4}$ and an elastic collision rate $\kappa \sim 2000~\text{s}^{-1}$. This elastic collision rate is sufficiently high that a first stage of adiabatic compression is not necessary. However this could be included (by reducing the trap radius and increasing the depth at constant power) if the starting conditions required it, hence evaporation can be optimized for a broad range of experimental parameters. We note moreover that the chosen initial atom number is conservative, and that increasing the trap size results in more atoms being captured [98], ultimately leading to a larger condensate.
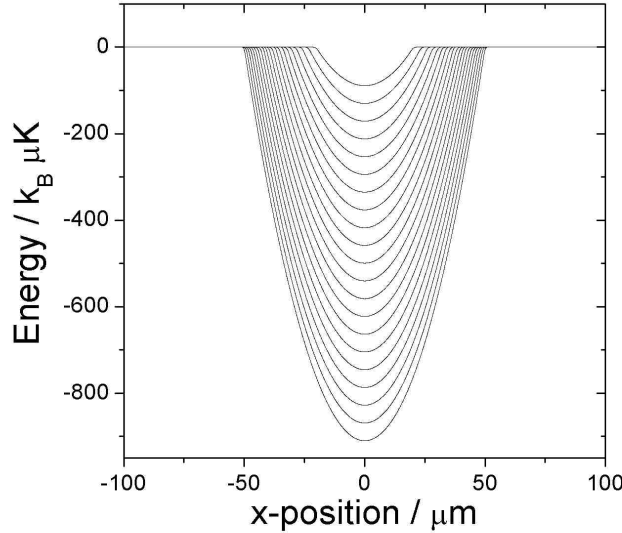


**Figure 4.46:** *A power-law trap of order 2 is decreased in depth and width such that atoms are evaporatively cooled at constant elastic collision rate.*
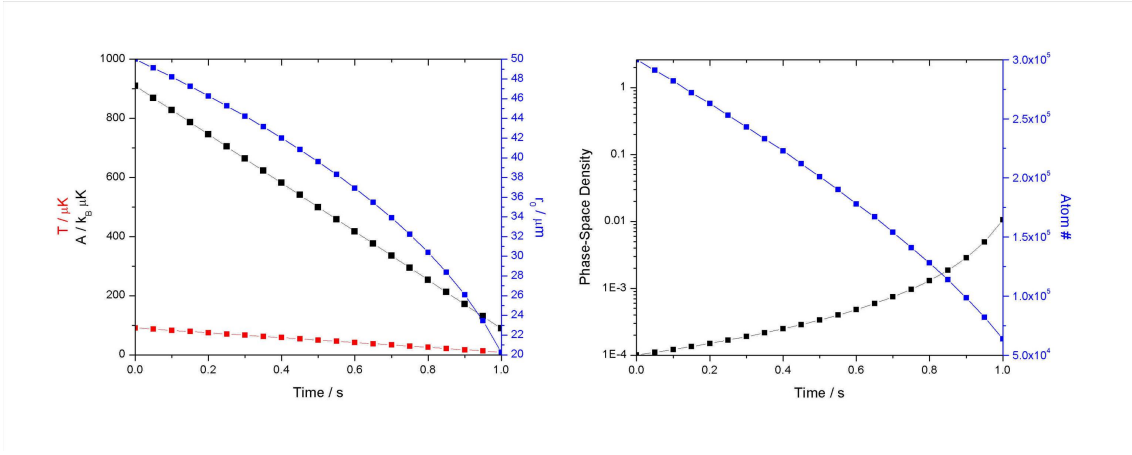
**Figure 4.47:** *(left) The evolution of the parabolic trap parameters and the tempera-
ture of the Bose gas during the evaporative cooling sequence. (right) The evaporation
loses almost one order of magnitude of the atom number, and the phase-space den-
sity at the end of the evaporation is two orders of magnitude lower than required for
BEC.*

A possible evaporation sequence is shown in Figure 4.46. The trap depth is
gradually lowered to force evaporation, while the trap radius is adjusted to main-
tain optimal conditions. In particular, we choose to keep the elastic collision rate
constant, as opposed to selecting a sequence of runaway evaporation. Given our
starting conditions, this ensures that the atomic number density does not increase
to the point where three-body recombination losses become significant. The trap
order is kept at 2 because smaller values would result in decreased efficiency of the
evaporation process [159]. The efficiency is defined as:

$$\gamma = -\frac{\mathrm{d}\ln D}{\mathrm{d}\ln N}, \tag{4.22}$$

which is equivalent to $N \propto 1/D^{\frac{1}{\gamma}} \propto T^{\frac{3}{2\gamma}} V^{\frac{1}{\gamma}}/N^{\frac{1}{\gamma}}$, where $V$ is the effective volume
occupied by the atoms. This relation can be used to express the dependence of $N$
on $V$ and $T$, which is then substituted in the condition for the elastic collision rate
$\kappa \propto T^{1/2}N/V = $ constant. Next we express $T$ and $V$ in terms of the trap depth
and radius respectively: $T \propto A$ and $V \propto r_0^3$, assuming the truncation parameter
$\eta = A/(k_B T)$ is kept fixed throughout evaporation. The condition for constant $\kappa$
finally becomes:

$$\frac{A^{\frac{\gamma}{2}+2}}{r_0^{3\gamma}} = \text{constant}, \tag{4.23}$$

which is used to plot the intermediate steps of the evaporation sequence in Figure
4.46. For this we assume $\gamma = 3$ and $\eta = 10$ (i.e. evaporation near stagnation), as
typical for evaporation in optical traps [160, 92, 93, 98]. Similarly to these exper-
iments, we expect evaporation to work on timescales of seconds. Hence the SLM
needs to be refreshed at a rate less than 20 Hz to produce the intermediate steps.

Given that this is much smaller than the characteristic trap frequency, we do not expect significant parametric heating [161] from residual intensity flicker at the refresh rate.

We stop the evaporation below the critical phase-space density with the final trap radius and depth 20 $\mu$m and 84 $\mu$K respectively. At this point $D = 0.011$ and $N = 6 \times 10^4$ atoms remain in the trap (see Figure 4.47). From this point we can follow one of the two routes to degeneracy using the adiabatic transformation described in the Section 4.14.3.

### 4.14.3   Adiabatic Transformations
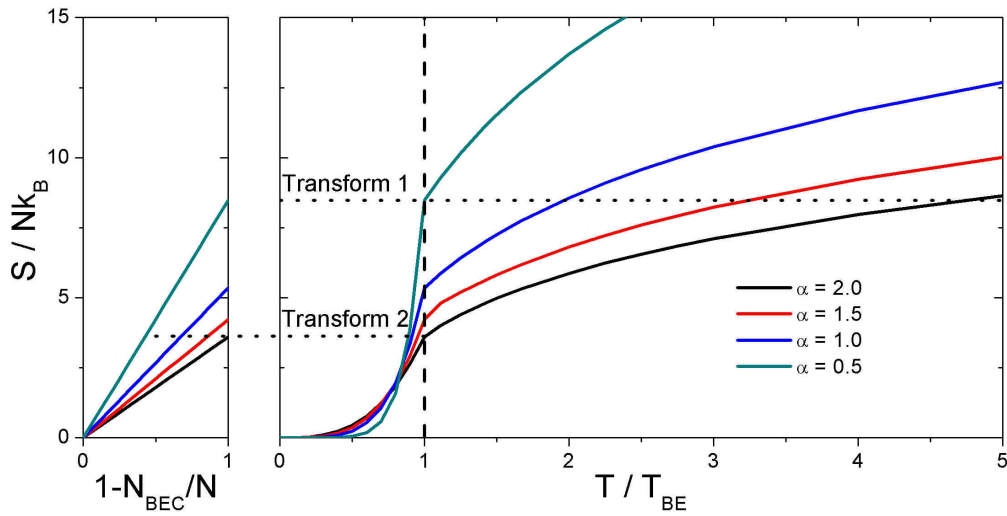


**Figure 4.48:**  *The entropy of a Bose gas in a power-law trap of order $\alpha$ as a function of (left) condensate fraction and (right) temperature above and below $T_{BE}$. The two dotted lines represent transformations at constant entropy. By transforming from a power-law trap of order 2 containing a gas at $T/T_{BE} = 4.7$ to a power-law trap of order 0.5, the gas reaches the critical temperature (upper dotted line). Starting from $T = T_{BE}$ in the $\alpha = 2$ trap, an adiabatic transformation to $\alpha = 0.5$ leads to a condensate fraction of about 0.6 (lower dotted line).*

As shown in [63], the phase-space density of a collisional gas can be increased adiabatically and reversibly, without loss of atoms, by reducing the trap order. This is different from compressing or expanding a trap while keeping the same order, in which case the temperature and the number density change so as to keep the phase-space density constant. In the following, we consider adiabatic transformations in which the trap order goes from $\alpha = 2$ to 0.5, starting from the parabolic trap at the end of the evaporation sequence (i.e. the smallest trap in Figure 4.46).

For such a transformation to be reversible, it must be slow compared to the thermalization time. We estimate that the elastic collision rate during our sequence does not drop significantly from the value of 2000 s$^{-1}$ during evaporation, so a

sequence lasting about one second (as suggested in Section 4.14.1) satisfies this requirement. We can therefore impose that the entropy $S$ is constant during the transformation, with $S$ defined by (1.42).

The entropy of a Bose gas in a power-law potential above and below the critical temperature $T_{BE}$ was found in (1.42), which can be combined with (1.37) to give the plot in Figure 4.48. We highlight two potential transformations of interest, one which takes the gas to the critical temperature and another which starts with a gas on the cusp of BEC which we transform across the transition to increase the condensate fraction efficiently.

**Transformation to $T_{BE}$**

We define our first transformation such that at $\alpha = 0.5$ the atoms reach the critical temperature for Bose-Einstein condensation, i.e. $T = T_{BE}$.

The entropy per particle $S/Nk_B = 8.47$ at the critical temperature for $\alpha = 0.5$ (see upper dotted line in Figure 4.48). This means that the entropy per particle at the beginning of the adiabatic transformation, i.e. for $\alpha = 2$, must also be $8.47k_B$. This corresponds to $T/T_{BE} = 4.7$ and $D_1 = 0.011$ in the parabolic trap, as achieved at the end of the evaporation. We solve (1.42) numerically to find $z(\alpha)$ and use (1.37) to determine $\frac{T}{T_{BE}}(\alpha)$ for the intermediate steps of the adiabatic sequence as shown in Figure 4.49.
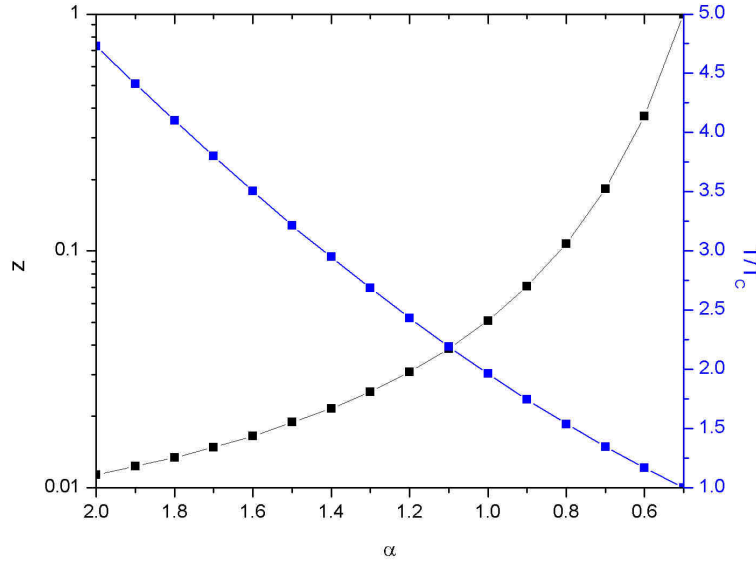


**Figure 4.49:** *The temperature and critical temperature both decrease by lowering the power-law order $\alpha$ (Figure 4.50) but the ratio $T/T_{BE}$ also decreases. The fugacity increases by two orders of magnitude.*

To calculate the evolution of our optical trap we need to specify the trap depth $A(\alpha)$ and size $r_0(\alpha)$ required for this sequence. We start by imposing $A(\alpha) = 10k_BT(\alpha)$ to avoid further evaporation during the transformation. Secondly, the end

point of the sequence is determined by imposing a peak density $\rho = 1.8 \times 10^{14}$ cm$^{-3}$, which gives a moderate rate of atom loss due to three-body recombination of 1s$^{-1}$ [162]. We then use the critical condition $\rho \lambda_{dB}^3 = 2.612$ to calculate $T_{BE} = 582$ nK in the $\alpha = 0.5$ trap. To find the trap size $r_0(0.5)$, we consider the expression for $T_{BE}$ in a generic power-law trap [163]:

$$k_B T_{BE} = \left[ \frac{N\hbar^3}{(2m)^{\frac{3}{2}}} \frac{6\sqrt{\pi} A^{\frac{3}{\alpha}}}{r_0^3 \Gamma\left(1 + \frac{3}{\alpha}\right) \zeta\left(\frac{3}{2} + \frac{3}{\alpha}\right)} \right]^{\frac{1}{\frac{3}{2} + \frac{3}{\alpha}}}, \tag{4.24}$$

and we solve it for $r_0$ to find $r_0(0.5) = 59$ $\mu$m.

Having fixed the trap parameters at the start and the end of the sequence, we assume for simplicity a linear interpolation for $r_0(\alpha)$. We use (4.24), in conjunction with $\frac{T}{T_{BE}}(\alpha)$ from entropy conservation, to determine $T(\alpha)$ and $T_{BE}(\alpha)$ individually, as shown in Figure 4.50.
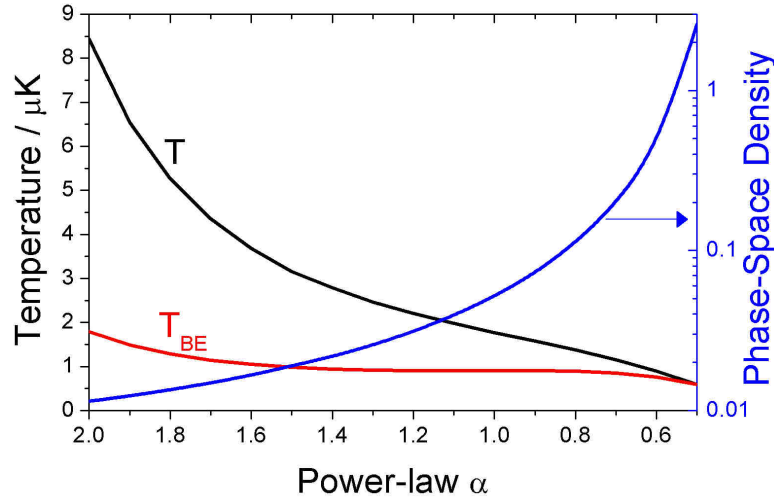


**Figure 4.50:** *The temperature and critical temperature decrease by changing the power-law order $\alpha$, until they are equal. The phase-space density of the gas increases by about a factor 230 to 2.612.*

This now allows us to find $A(\alpha)$, and the resulting trap profiles are shown in Figure 4.51 and the parameter variation is plotted in Figure 4.52.

The optical power needed for the final trap ($\alpha = 0.5$) is 36 mW per beam, which is 0.26% of the power at the start of evaporation. Such a large dynamic range can be achieved by varying the power illuminating the SLM, e.g. with a motorized rotating waveplate followed by a Glan-Taylor polarizer, and by changing the power emitted by the laser [98]. Towards the end of the adiabatic transformation, the trap is so shallow that the effect of gravity cannot be neglected. It is possible to compensate for it either with a magnetic field gradient, or by designing "tilted" intensity patterns.

**Figure 4.51:** *The power-law trap is adiabatically transformed from order 2 to order 0.5 and the trap depth and size are varied so as to reach the critical temperature at the end of the sequence. The inset shows in greater detail the final stages of the adiabatic transformation.*
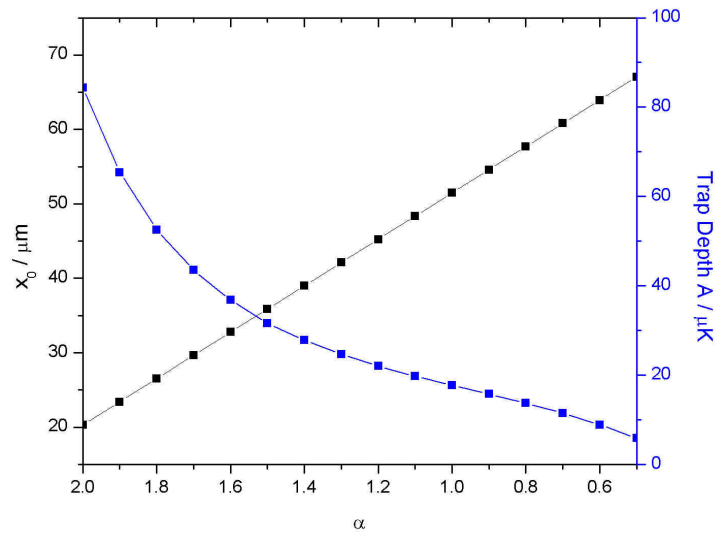


**Figure 4.52:** *The evolution of the trap parameters during the adiabatic sequence.*
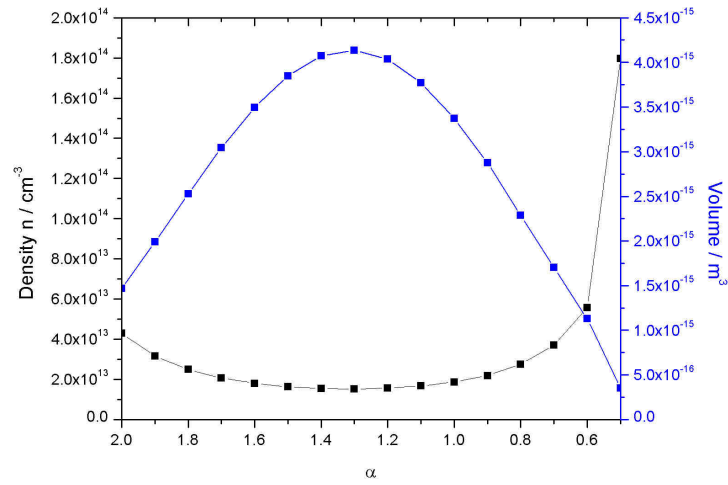
**Figure 4.53:** *The density of atoms in the trap initially decreases before reaching a peak at $\alpha = 0.5$, while the volume is initially increased but is minimised at $\alpha = 0.5$.*

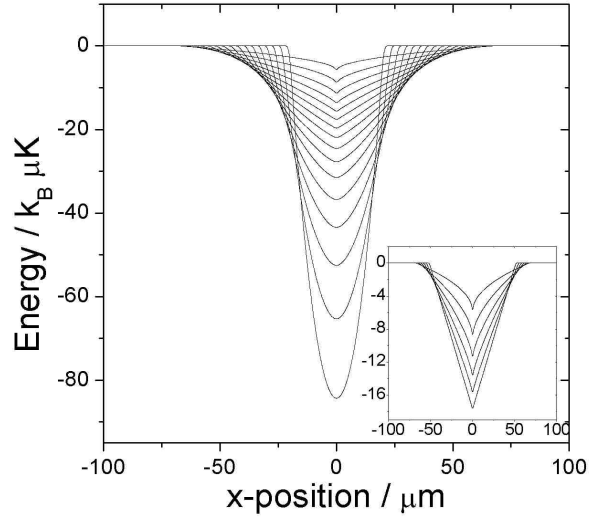We see from Figure 4.50 that the adiabatic transformation achieves a significant gain in phase-space density. Intuitively, the gas undergoes an expansion and its temperature decreases. However the change in trap order causes an increase in *peak* density which is especially pronounced at the end of the sequence (Figure 4.53). The volume of the trap and the gas density follow opposite trends. At $\alpha = 1.3$ the volume is maximised while the density is minimised. At the end of the sequence we obtain the minimum volume which is one-third of the initial volume, while the peak density reaches its maximum of 4 times the initial density. We estimate that only 5% of atoms are lost due to three-body recombination for a sequence that lasts 1s, which justifies our assumption of constant atom number throughout the adiabatic transformation. In conclusion, about 20% of the laser-cooled atoms loaded into the initial optical trap remain when the sequence terminates at the BEC transition,
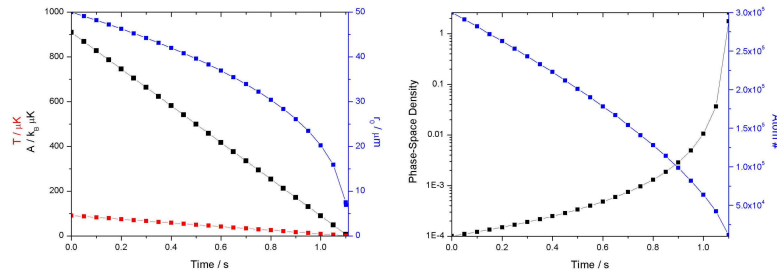


**Figure 4.54:** *(left) The evolution of the parabolic trap parameters and the temperature of the Bose gas during the evaporative cooling sequence which reaches the BEC transition. (right) The evaporation now leaves only 3% of the atoms when the phase-space density causes the gas to transition to a BEC.*
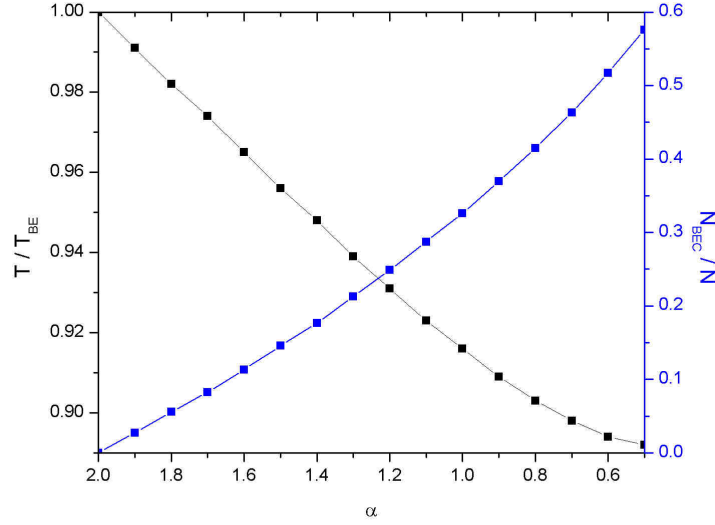
**Figure 4.55:** *(left) The evolution of the parabolic trap parameters and the tempera-ture during the evaporation sequence which reaches the BEC transition. (right) The evaporation now leaves only 3% of the atoms at the transition to a BEC.*

which is higher than in any other all-optical technique implemented so far.

### Transformation from $T_{BE}$

Evaporation can be continued in the parabolic trap for 101.5ms to reach the BEC transition at the efficiency assumed in Section 4.14.2, for which the trap parameters, phase-space density and number of atoms evolution are shown in Figure 4.54.

At this point $10^4$ atoms remain in the trap - which is only 3% of the initial atom number. In this case however the adiabatic change of trap order (see lower dotted line in Figure 4.48) provides a new method to cross the BEC transition in a reversible way, similarly to the dimple technique [96].

The critical entropy per particle in the parabolic trap is $3.60k_B$. From the conser-vation of entropy, we find that varying $\alpha$ from 2 to 0.5 leads to $T/T_{BE} \simeq 0.89$. The condensate fraction $N_{BEC}/N \simeq 0.6$ is found using (1.38), as shown in the left side of Figure 4.48 and in Figure 4.55, hence $N_{BEC} \simeq 6000$ at the end of the adiabatic transformation. As a final comment on our method, if larger atom numbers can be obtained (particularly in the original loading of the optical trap), our sequence could be combined with *in-situ* imaging [156] to provide a reversible method to investigate the BEC transition.

## 4.15   Ring Traps for the Investigation of Superfluidity

Now that we have a method for achieving Bose-Einstein Condensation, we would like to use our apparatus to perform interesting science with the ultracold gas. The purpose of the continuous ring trap that we have been using in examples throughout this chapter is the investigation of superfluidity effects. Superfluidity in dilute ultracold atomic gases has been demonstrated through the presence of a critical velocity [18], the formation of arrays of vortices under rotation [20] and the observation of persistent flow [22] of an ultracold gas in a ring trap, which can be interpreted as pinning of a macroscopic vortex state.

The ring trap is programmed to have an intensity $I_0$ with two bright spots of intensity $I_0 + I_p$, given by

$$
\begin{aligned}
I(x,y) = {}& I_0 \exp(-2(\sqrt{x^2 + y^2} - R)^2/w^2) \\
& + I_p \exp(-2((x + R\sin\theta)^2 + (y - R\cos\theta)^2)/w^2) \\
& + I_p \exp(-2((x - R\sin\theta)^2 + (y + R\cos\theta)^2)/w^2),
\end{aligned}
\tag{4.25}
$$

where $R$ is the radius of the ring, $\theta$ is the angular position of the bright spots, and $w$ is the $1/e^2$ waist of the Gaussian ring potential. Our feedback algorithm has given us a ring trap with an rms error of 4%, as shown in Figure 4.30.

The trapping potential $U(x,y)$ is given by

$$
U(x,y) = \frac{3\pi c^2 \Gamma}{2\omega_0^3 \delta} \frac{P}{\pi\left((R+w)^2 - (R-w)^2\right)} \exp\left(-2\frac{\left(\sqrt{x^2 + y^2} - R\right)^2}{w^2}\right), \tag{4.26}
$$

where we propose to generate a ring trip of radius $R = 80\mu$m with $w = 25\mu$m using $P = 10$mW of power at 1060nm to confine $10^5$ $^{87}$Rb atoms. This gives a peak trap depth of 52.3nK, and a trap frequency (extracted by performing a parabolic fit to the trap profile) of $\omega = 2\pi \times 29$ Hz. The density of atoms in the ring is assumed to be uniform, and we assume that the trap size off-plane is twice the thickness of the ring $r$.

Superflow can be induced by "stirring" the atoms in the ring potential by rotating the bright spots within the pattern, as shown in Figure 4.56a). The experiments reported in [22] showed superflow of atoms with angular momentum $\hbar$ and $2\hbar$, which for their trap corresponds to a rotational frequency of around 7 Hz and 14 Hz respectively. The maximum rate at which our SLM can refresh the whole pattern is 500 Hz, which allows a maximum of 70 steps within one complete rotation of our ring trap. The difference between consecutive positions of the bright spots ($25\mu$m waist) is $7\mu$m, which should thus be sufficiently small that the motion of the stirring appears continuous to the atoms. Once superflow has begun, the stirring beams can be gradually removed, as shown in Figure 4.56b). As in [20], we plan to ramp the value $I_p$ to zero within 20 ms, which allows us to refresh the pattern ten times.
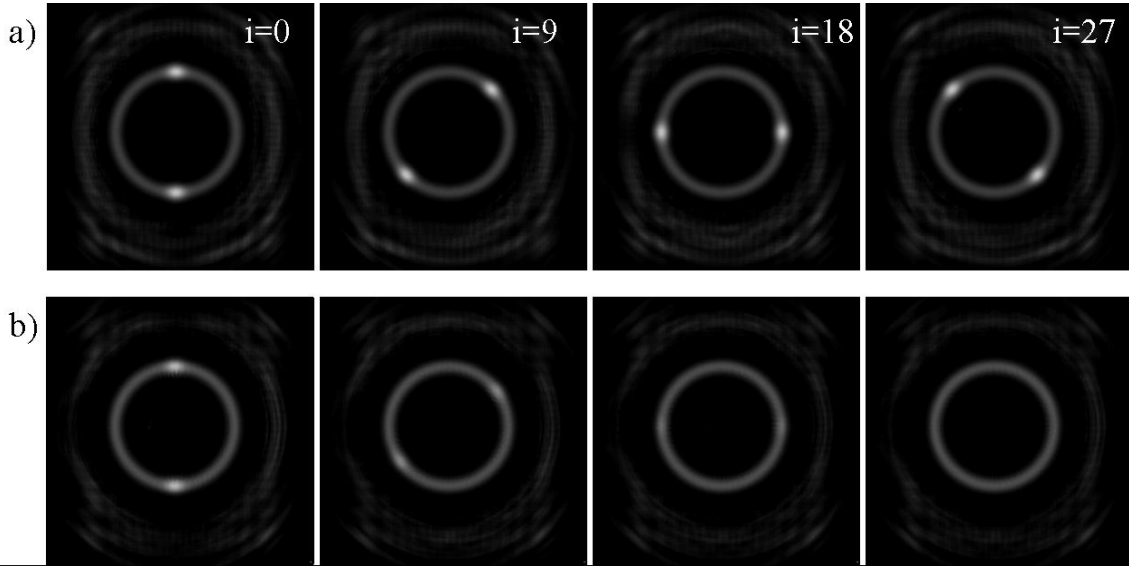
**Figure 4.56:** *a) The pattern can be rotated to stir the ultracold gas. We show equally-spaced snapshots from the first half of a 70-step sequence. b) Once stirring has been completed, the bright spots can be slowly removed to leave a uniform ring trap.*

If the BEC was made to travel at velocities above the speed of sound, the supersonic flow would decay through the formation of vortices and the excitation of collective modes. The speed of sound in a BEC is $\sqrt{\mu/m}$ where $\mu$ is the chemical potential and $m$ is the atomic mass, which corresponds to a critical rotational frequency of 58 Hz for the experiment reported in [22]. As this frequency would restrict us to a sequence containing only 8 steps per full rotation, we will remain well below the maximum speed for the observation of persistent flow.

Whilst we have used a limited power to implement the feedback algorithm, our SLM can be illuminated by up to 3.5 Wcm$^{-2}$. We could, for example, illuminate the SLM with 360 mW of 1060 nm light to generate a ring of radius $80\mu$m and waist $25\mu$m, giving us 10 mW in the measure region; using (1.25), this corresponds to a ring trap of depth 52 nK for $^{87}$Rb atoms. The light pattern shown here is two-dimensional, and disperses quickly away from the Fourier plane. To confine atoms to the Fourier plane we will add an orthogonal light sheet with a trapping frequency close to that of the ring trap. The chemical potential of a BEC in such a ring trap is calculated using the Thomas-Fermi approximation as shown in Section 1.5.2. The density profile of a condensate in our ring trap is

$$N_0 \left| \Phi_0 \left( r, z \right) \right|^2 = m \frac{\mu - \frac{1}{2} m \omega^2 \left( \left( r - R \right)^2 + z^2 \right)}{4 \pi \hbar^2 a_s}. \qquad (4.27)$$

Normalisation of the wavefunction thus gives the chemical potential as

$$\mu = \hbar \omega \sqrt{\frac{2 N a_s}{\pi R}}, \qquad (4.28)$$

where $R$ is the radius of the ring as before, $\omega = 2\pi \times 20$ Hz is the radial trapping

frequency, $N$ is the number of trapped atoms and $a_s$ is the s-wave scattering length. In the absence of magnetic fields, this is $106a_0$ for $^{87}$Rb [164], with $a_0$ the Bohr radius. For $10^5$ $^{87}$Rb atoms in the ring trap described above, the chemical potential is 18 nK. This is around one third of the trap depth given above, thus making trapping possible [123]. The residual fluctuations in the output of the feedback algorithm give us a roughness of $\mu/9$, lower than the value reported in [22], which should allow us to observe superflow in this trap.

## 4.16   Summary and Prospects

We have shown that computer generated holographic techniques supplemented with a feedback algorithm can produce flexible, smooth and dynamic all-optical traps for the purposes of trapping ultracold atoms.

A number of algorithms for generating holographic atom traps have been tested, both programmatically and with a physical SLM. The aberrations that have so far restricted the use of such patterns for investigations with cold atoms have now been overcome, and all that remains is for the experiments presented above to be integrated into the cold atoms experiment in St Andrews. In particular, we have shown that we can generate optical traps for the cooling of the cold gas and the experimental investigations of superfluidity can be performed using the same diffractive optical element.

We have shown that the dynamic manipulation of the optical traps can be achieved by varying the hologram on the SLM, and demonstrated that by minimising the differences between subsequent holograms we can reduce any flicker below our detection levels. In future, it would be advisable to measure with greater accuracy any flicker for small changes in the holograms, e.g. by measuring the light levels of a single camera pixel during the evolution.

The techniques look likely to open a wide range of exciting experiments. The feedback methods will also benefit from using the atoms as a sensitive probe of discrepancies in the feedback loop. Further improvements to the MRAF algorithm have been suggested since the work presented here which improve the quality of the calculated output of the IFTA, but still utilizes our feedback method in order to make the actual optical traps sufficiently smooth to trap atoms [154].

We have used an SLM to holographically generate power-law intensity patterns of different orders and sizes, and we have shown how a sequence of these can be used as a dynamic optical trap for fast and efficient production of Bose-Einstein condensates. Starting from realistic assumptions, we have calculated the trap parameters throughout the sequence. We have also presented the adiabaticity criteria for a generic transformation that goes beyond the standard case of the compression and expansion in a harmonic trap. A future step will be the study of evaporative cooling and adiabatic transformations in more complex trap geometries. We have also characterised a ring trap for the investigation of superfluidity to prove the ability of our feedback method in improving the smoothness of optical traps.

# Chapter 5

# Conclusions and Outlook

In this thesis, I have presented work carried out in St Andrews to achieve a compact and flexible apparatus for cold atoms, using non-standard techniques in both the cooling and the manipulation stages of the experiment.

Chapter 2 contained the results of pulsed MOT loading experiments with $^{87}$Rb in a stainless steel single vacuum chamber. The technique of Light Induced Atomic Desorption proved to be unsuitable for loading large MOTs at low background pressures, while pulsing the atomic dispenser loaded MOTs up to $10^8$ atoms with a rapidly varying background pressure when single pulses were applied. Over many pulses of the dispenser, however, the vacuum chamber was heated and the background pressure rose. Active cooling of the vacuum chamber and electrical feedthroughs may limit this buildup of pressure in any future stainless steel chamber.

These results encouraged us to instead opt for building a new Pyrex vacuum chamber which allows us to better use LIAD as a source of MOTs of up to $8 \times 10^7$ at lower pressure, as described in Chapter 3. While LIAD depletes the atom reservoir over many pulses, this depletion can be compensated by running the dispenser continuously at a low value. Measurements of the lifetime of atoms loaded from the LIAD-assisted MOT into a magnetic trap showed that the LIAD effect greatly assisted storage of atoms by a factor of 6 in the magnetic trap when compared to magnetically trapped atoms loaded under constant background pressure. Vacuum-related problems have temporarily halted progress in this apparatus, but a thorough cleaning of the chamber and regeneration of the pumps will allow the experiment to progress to evaporative cooling soon.

In the final chapter of this thesis, I have outlined our alternative approach to flexible manipulation of ultracold atoms using a Spatial Light Modulator to generate holographic atom traps. We have successfully demonstrated that these holographic atom traps can be calculated and aberrations in the physical implementation can be reduced to acceptable levels. The feedback algorithm we have used can create a variety of experimentally interesting traps for cold atoms, and I have highlighted two of these proposals especially.

The SLM will soon be integrated into the experimental apparatus of Chapter 3 and an improved feedback algorithm using cold atoms as a sensitive probe of optical aberrations gives hope for further improvements to the quality of holographic atom traps.

The evaporative cooling of the atoms will be performed in the holographic power-law optical trap after pre-cooling in the quadrupole magnetic field, and the BEC transition can be crossed reversibly using our dynamic and adiabatic evolution of the power-law trap.

The dynamic ring trap will be used for investigations into superfluid effects in cold atoms, with the potential for future manipulations to the trap geometry to produce novel experiments.

I have no doubt that the future of cold atomic physics will be shaped by more flexible trapping potentials, and hope that the work here will contribute to widespread use of holographic atom traps.

# Bibliography

[1] M. Glazer and J. Wark. *Statistical Mechanics, a Survival Guide.* Oxford University Press, 2001.

[2] W. Pauli. On the Connexion between the Completion of Electron Groups in an Atom with the Complex Structure of Spectra. *Z. Phys.*, 31:765, 1925.

[3] S. N. Bose. Plancks Gesetz und Lichtquantenhypothese (Planck's Law and Light Quantum Hypothesis). *Z. Phys.*, 26:178, 1924.

[4] A. Einstein. Quantentheorie des einatomigen idealen Gases. *Sitzungsber. Kgl. Preuss. Akas. Wiss.*, page 261, 1924.

[5] A. Einstein. Quantentheorie des einatomigen idealen Gases. *Sitzungsber. Kgl. Preuss. Akas. Wiss.*, page 3, 1925.

[6] E. Fermi. Zur Quantelung des Idealen Einatomigen Gases (On Quantization of Perfect Monatomic Gases). *Z. Phys.*, 36:902, 1926.

[7] P. A. M. Dirac. On the Theory of Quantum Mechanics. *Proc. Roy. Soc. A*, 112:661, 1926.

[8] W. Ketterle. Nobel Lecture: When atoms behave as waves: Bose-Einstein condensation and the atom laser. *Rev. Mod. Phys.*, 74:1131, 2002.

[9] M. H. Anderson, J. R. Ensher, M. R. Matthews, C. E. Wieman, and E. A. Cornell. Observation of Bose–Einstein Condensation in a Dilute Atomic Vapor. *Science*, 269:198, 1995.

[10] C. C. Bradley, C. A. Sackett, J. J. Tollett, and R. G. Hulet. Evidence of Bose–Einstein Condensation in an Atomic Gas with Attractive Interactions. *Phys. Rev. Lett.*, 75:1687, 1995.

[11] K. B. Davis, M. O. Mewes, M. R. Andrews, N. J. van Druten, D. S. Durfee, D. M. Kurn, and W. Ketterle. Bose-Einstein Condensation in a Gas of Sodium Atoms. *Phys. Rev. Lett.*, 75:3969, 1995.

[12] B. DeMarco and D. S. Jin. Onset of Fermi Degeneracy in a Trapped Atomic Gas. *Science*, 285:1703, 1999.

[13] F. London. The $\lambda$-phenomenon of liquid helium and the Bose-Einstein degeneracy. *Nature*, 141:643, 1938.

[14] N. Bogoliubov. On the theory of superfluidity. *J. Phys.*, 11:23, 1947.

[15] C. A. Regal, M. Greiner, and D. S. Jin. Observation of Resonance Condensation of Fermionic Atom Pairs. *Phys. Rev. Lett.*, 92:040403, 2004.

[16] M. W. Zwierlein, C. A. Stan, C. H. Schunck, S. M. F. Raupach, A. J. Kerman, and W. Ketterle. Condensation of pairs of fermionic atoms near a Feshbach Resonance. *Phys. Rev. Lett.*, 92:120403, 2004.

[17] L. N. Cooper. Bound Electron Pairs in a Degenerate Fermi Gas. *Phys. Rev.*, 104:1189, 1956.

[18] C. Raman, M. Köhl, R. Onofrio, D. S. Durfee, C. E. Kuklewicz, Z. Hadzibabic, and W. Ketterle. Evidence for a Critical Velocity in a Bose-Einstein Condensed Gas. *Phys. Rev. Lett.*, 83:2502–2505, 1999.

[19] K. W. Madison, F. Chevy, V. Bretin, and J. Dalibard. Stationary States of a Rotating Bose-Einstein Condensate: Routes to Vortex Nucleation. *Phys. Rev. Lett.*, 86:4443, 2001.

[20] J. R. Abo-Shaeer, C. Raman, J. M. Vogels, and W. Ketterle. Observation of Vortex Lattices in Bose-Einstein Condensates. *Science*, 292:476–479, 2001.

[21] M. W. Zwierlein, J. R. Abo-Shaeer, A. Schirotzek, C. H. Schunck, and W. Ketterle. Vortices and superfluidity in a strongly interacting Fermi gas. *Nature*, 435:1047–1051, 2005.

[22] C. Ryu, M. F. Andersen, P. Cladé, Vasant Natarajan, K. Helmerson, and W. D. Phillips. Observation of Persistent Flow of a Bose-Einstein Condensate in a Toroidal Trap. *Phys. Rev. Lett.*, 99:260401, 2007.

[23] A. Ramanathan, K. C. Wright, S. R. Muniz, M. Zelan, W. T. Hill, C. J. Lobb, K. Helmerson, W. D. Phillips, and G. K. Campbell. Superflow in a Toroidal Bose-Einstein Condensate: An Atom Circuit with a Tunable Weak Link. *Phys. Rev. Lett.*, 106(13):130401, 2011.

[24] I. Bloch. Ultracold quantum gases in optical lattices. *Nat. Phys.*, 1:23–30, 2005.

[25] J. Quintanilla, S. T. Carr, and J. J. Betouras. Metanematic, smectic, and crystalline phases of dipolar fermions in an optical lattice. *Phys. Rev. A*, 79:031601, 2009.

[26] M. Greiner, O. Mandel, T. Esslinger, T. W. Hänsch, and I. Bloch. Quantum phase transition from a superfluid to a Mott insulator in a gas of ultracold atoms. *Nature*, 415:39, 2002.

[27] M. Lewenstein, A. Sanpera, V. Ahufinger, B. Damski, A. Sen(De), and U. Sen. Ultracold atomic gases in optical lattices: mimicking condensed matter physics and beyond. *Adv. Phys.*, 56:243–379, 2007.

[28] R. Jördens, N. Strohmaier, K. Günter, H. Moritz, and T. Esslinger. A Mott insulator of fermionic atoms in an optical lattice. *Nature*, 455:204–207, 2008.

[29] U. Schneider, L. Hackermüller, S. Will, Th. Best, I. Bloch, T. A. Costi, R. W. Helmes, D. Rasch, and A. Rosch. Metallic and Insulating Phases of Repulsively Interacting Fermions in a 3D Optical Lattice. *Science*, 322:1520–1525, 2008.

[30] J. Simon, W. S. Bakr, R. Ma, M. E. Tai, P. M. Preiss, and M. Greiner. Quantum simulation of antiferromagnetic spin chains in an optical lattice. *Nature*, 472:307–312, 2011.

[31] S. Trebst, U. Schollwöck, M. Troyer, and P. Zoller. d-Wave Resonating Valence Bond States of Fermionic Atoms in Optical Lattices. *Phys. Rev. Lett.*, 96:250402, 2006.

[32] K. A. Kuns, A. M. Rey, and A. V. Gorshkov. *d*-wave superfluidity in optical lattices of ultracold polar molecules. *Phys. Rev. A*, 84:063639, 2011.

[33] J. Billy, V. Josse, Z. Zuo, A. Bernard, B. Hambrecht, P. Lugan, D. Clément, L. Sanchez-Palencia, P. Bouyer, and A. Aspect. Direct observation of Anderson localization of matter waves in a controlled disorder. *Nature*, 453:891, 2008.

[34] G. Roati, C. DErrico, L. Fallani, M. Fattori, C. Fort, M. Zaccanti, G. Modugno, M. Modugno, and M. Inguscio. Anderson localization of a non-interacting BoseEinstein condensate. *Nature*, 453:895, 2008.

[35] S. S. Kondov, W. R. McGehee, J. J. Zirbel, and B. DeMarco. Three-Dimensional Anderson Localization of Ultracold Matter. *Science*, 334(6052):66–68, 2011.

[36] R. N. Palmer and D. Jaksch. High-Field Fractional Quantum Hall Effect in Optical Lattices. *Phys. Rev. Lett.*, 96:180407, 2006.

[37] S.-L. Zhu, H. Fu, C.-J. Wu, S.-C. Zhang, and L.-M. Duan. Spin Hall Effects for Cold Atoms in a Light-Induced Gauge Potential. *Phys. Rev. Lett.*, 97:240401, 2006.

[38] G. K. Brennen, C. M. Caves, P. S. Jessen, and I. H. Deutsch. Quantum Logic Gates in Optical Lattices. *Phys. Rev. Lett.*, 82:1060–1063, 1999.

[39] H. Weimer, M. Müller, I. Lesanovsky, P. Zoller, and H. P. Büchler. A Rydberg quantum simulator. *Nat. Phys.*, 6:382, 2010.

[40] D. Solenov and D. Mozyrsky. Cold Atom Qubits. *Journal of Computational and Theoretical Nanoscience*, 8:481, 2011.

[41] C. Weitenberg, S. Kuhr, K. Mølmer, and J. F. Sherson. Quantum computation architecture using optical tweezers. *Phys. Rev. A*, 84:032322, 2011.

[42] C. J. Foot. *Atomic Physics*. OUP, 2005.

[43] H. J. Metcalf and P. van der Straten. *Laser Cooling and Trapping*. Springer, New York, 1999.

[44] A. Ashkin. Acceleration and Trapping of Particles by Radiation Pressure. *Phys. Rev. Lett.*, 24:156, 1970.

[45] A. Ashkin. Atomic-Beam Deflection by Resonance-Radiation Pressure. *Phys. Rev. Lett.*, 25:1321, 1970.

[46] J. P. Gordon and A. Ashkin. Motion of atoms in a radiation trap. *Phys. Rev. A*, 21:1606, 1980.

[47] S. Chu, L. Holberg, J. E. Bjorkholm, A. Cable, and A. Ashkin. Three-Dimensional Viscous Confinement and Cooling of Atoms by Resonance Radiation Pressure. *Phys. Rev. Lett.*, 55:48, 1985.

[48] A. Ashkin and J. P. Gordon. Stability of radiation-pressure particle traps: an optical Earnshaw theorem. *Opt. Lett.*, 8:511, 1983.

[49] E. L. Raab, M. Prentiss, A. Cable, S. Chu, and D. E. Pritchard. Trapping of Neutral Sodium Atoms with Radiation Pressure. *Phys. Rev. Lett.*, 59:2631, 1987.

[50] P. D. Lett, W. D. Phillips, S. L. Rolston, C. E. Tanner, R. N. Watts, and C. I. Westbrook. Optical molasses. *J. Opt. Soc. Am. B*, 6:2084, 1989.

[51] P. D. Lett, R. N. Watts, C. I. Westbrook, W. D. Phillips, P. L. Gould, and H. J. Metcalf. Observation of Atoms Laser Cooled below the Doppler Limit. *Phys. Rev. Lett.*, 61:169, 1988.

[52] J. Dalibard and C. Cohen-Tannoudji. Laser cooling below the Doppler limit by polarization gradients: simple theoretical models. *J. Opt. Soc. Am. B*, 6:2023, 1989.

[53] D. W. Sesko, T. G. Walker, and C. E. Wieman. Behavior of neutral atoms in a spontaneous force trap. *J. Opt. Soc. Am. B*, 8:946, 1991.

[54] W. Ketterle, K. B. Davis, M. A. Joffe, A. Martin, and D. E. Pritchard. High Densities of Cold Atoms in a Dark Spontaneous-Force Optical Trap. *Phys. Rev. Lett.*, 70:2253, 1993.

[55] M. H. Anderson, W. Petrich, J. R. Ensher, and E. A. Cornell. Reduction of light-assisted collisional loss rate from a low-pressure vapor-cell trap. *Phys. Rev. A*, 50:R3597, 1994.

[56] C. G. Townsend, N. H. Edwards, K. P. Zetie, C. J. Cooper, J. Rink, and C. J. Foot. High-density trapping of cesium atoms in a dark magneto-optical trap. *Phys. Rev. A*, 53:1702, 1996.

[57] W. Petrich, M. H. Anderson, J. R. Ensher, and E. A. Cornell. Behavior of atoms in a compressed magneto-optical trap. *J. Opt. Soc. Am. B*, 11:1332, 1994.

[58] N. Masuhara, J. M. Doyle, J. C. Sandberg, D. Kleppner, and T. J. Greytak. Evaporative Cooling of Spin-Polarized Atomic Hydrogen. *Phys. Rev. Lett.*, 61:935, 1988.

[59] W. Petrich, M. H. Anderson, J. R. Ensher, and E. A. Cornell. Stable, Tightly Confining Magnetic Trap for Evaporative Cooling of Neutral Atoms. *Phys. Rev. Lett.*, 74:3352–3355, 1995.

[60] D. E. Pritchard. Cooling neutral atoms in a magnetic trap for precision spectroscopy. *Phys. Rev. Lett.*, 51:1336, 1983.

[61] R. Grimm, M. Weidemüller, and Y. B. Ovchinnikov. Optical Dipole Traps for Neutral Atoms. In Benjamin Bederson and Herbert Walther, editors, *Advances In Atomic, Molecular, and Optical Physics*, volume 42, pages 95 – 170. Academic Press, 2000.

[62] A. G. Truscott, K. E. Strecker, W. I. McAlexander, G. B. Partridge, and R. G. Hulet. Observation of Fermi Pressure in a Gas of Trapped Atoms. *Science*, 291(5513):2570–2572, 2001.

[63] P. W. H. Pinkse, A. Mosk, M. Weidemüller, M. W. Reynolds, T. W. Hijmans, and J. T. M. Walraven. Adiabatically Changing the Phase-Space Density of a Trapped Bose Gas. *Phys. Rev. Lett.*, 78:990–993, 1997.

[64] C. Pethick and H. Smith. *Bose-Einstein condensation in dilute gases.* Cambridge University Press, Cambridge, UK, 2002.

[65] C. Monroe, W. Swann, H. Robinson, and C. Wieman. Very Cold Trapped Atoms in a Vapor Cell. *Phys. Rev. Lett.*, 65:1571–1574, 1990.

[66] W. D. Phillips and H. Metcalf. Laser Deceleration of an Atomic Beam. *Phys. Rev. Lett.*, 48:596–599, 1982.

[67] R. Gaggl, L. Windholz, C. Umfer, and C. Neureiter. Laser Cooling of a Sodium Atomic-Beam Using the Stark Effect. *Phys. Rev. A*, 49:1119–1121, 1994.

[68] W. Ketterle, A. Martin, M. A. Joffe, and D. E. Pritchard. Slowing and Cooling Atoms in Isotropic Laser Light. *Phys. Rev. Lett.*, 69:2483–2486, 1994.

[69] M. Zhu, C. W. Oates, and J. L. Hall. Continuous High-Flux Monovelocity Atomic-Beam Based on a Broad-Band Laser-Cooling Technique. *Phys. Rev. Lett.*, 67:46–49, 1991.

[70] Ertmer, W. and Blatt, R. and Hall, J. L. and Zhu, M. Laser Manipulation of Atomic Beam Velocities: Demonstration of Stopped Atoms and Velocity Reversal. *Phys. Rev. Lett.*, 54:996–999, 1985.

[71] C. J. Myatt, N. R. Newbury, R. W. Ghrist, S. Loutzenhiser, and C. E. Wieman. Multiply loaded magneto-optical trap. *Opt. Lett.*, 21:290–292, 1996.

[72] J. Fortágh and C. Zimmermann. Magnetic microtraps for ultracold atoms. *Rev. Mod. Phys.*, 79:235–289, 2007.

[73] S. Wildermuth, P. Krüger, C. Becker, M. Brajdic, S. Haupt, A. Kasper, R. Folman, and J. Schmiedmayer. Optimized magneto-optical trap for experiments with ultracold atoms near surfaces. *Phys. Rev. A*, 69:030901, 2004.

[74] M. Vangeleyn, P. F. Griffin, E. Riis, and A. S. Arnold. Laser cooling with a single laser beam and a planar diffractor. *Opt. Lett.*, 35(20):3453–3455, 2010.

[75] D. A. Smith, S. Aigner, M. Hofferberth, S. andGring, M. Andersson, S. Wildermuth, S. Krüger, P.and Schneider, T. Schumm, and J. Schmiedmayer. Absorption imaging of ultracold atoms on atom chips. *Opt. Express*, 19(9):8471–8485, 2011.

[76] A. E. Leanhardt, Y. Shin, A. P. Chikkatur, D. Kielpinski, W. Ketterle, and D. E. Pritchard. Bose–Einstein Condensates near a Microfabricated Surface. *Phys. Rev. Lett.*, 90:100404, 2003.

[77] C. Wieman, G. Flowers, and S. Gilbert. Inexpensive laser cooling and trapping experiment for undergraduate laboratories. *Am. J. Phys.*, 63:317–330, 1995.

[78] J. Fortagh, A. Grossmann, T. W. Hänsch, and C. Zimmermann. Fast loading of a magneto-optical trap from a pulsed thermal source. *J. Appl. Phys.*, 84:6499–6501, 1998.

[79] P. F. Griffin, K. J. Weatherill, and C. S. Adams. Fast switching of alkali atom dispensers using laser-induced heating. *Rev. Sci. Instrum.*, 76:093102, 2005.

[80] E. Mariotti, M. Meucci, P. Bicchi, C. Marinelli, and L. Moi. An efficient photo-atom source. *Opt. Commun.*, 134:121–126, 1997.

[81] A. Gozzini, F. Mango, J. H. Xu, G. Alzetta, F. Maccarrone, and R. A. Bernheim. Light-Induced Ejection of Alkali Atoms in Polysiloxane Coated Cells. *Il Nuovo Cimento D*, 15:709–722, 1993.

[82] M. Meucci, E. Mariotti, P. Bicchi, C. Marinelli, and L. Moi. Light-Induced Atom Desorption. *Europhys. Lett.*, 25:639–643, 1994.

[83] C. Marinelli, K. A. Nasyrov, S. Bocci, B. Pieragnoli, A. Burchianti, V. Biancalana, E. Mariotti, and L. Atutov, S. N.and Moi. A new class of photo-induced phenomena in siloxane films. *Eur. Phys. J. D*, 13:231–235, 2001.

[84] E. B. Alexandrov, M. V. Balabas, D. Budker, D. English, D. F. Kimball, C.-H. Li, and V. V. Yashchuk. Light-induced desorption of alkali-metal atoms from paraffin coating. *Phys. Rev. A*, 66:042903, 2002.

[85] A. Cappello, C. de Mauro, A. Bogi, A. Burchianti, S. Di Renzone, A. Khanbekyan, C. Marinelli, E. Mariotti, L. Tomassetti, and L. Moi. Light induced atomic desorption from dry-film coatings. *J. Chem. Phys.*, 127:044706, 2007.

[86] S. N. Atutov, V. Biancalana, P. Bicchi, C. Marinelli, E. Mariotti, M. Meucci, A. Nagel, K. A. Nasyrov, S. Rachini, and L. Moi. Light-induced diffusion and desorption of alkali metals in a siloxane film: Theory and experiment. *Phys. Rev. A*, 60:4693–4700, 1999.

[87] A. Burchianti, C. Marinelli, A. Bogi, J. Brewer, K. Rubahn, H.-G. Rubahn, F. Della Valle, E. Mariotti, V. Biancalana, S. Veronesi, and L. Moi. Light-induced atomic desorption from porous silica. *Europhys. Lett.*, 67:983–989, 2004.

[88] W. Hänsel, P. Hommelhoff, T. W. Hänsch, and J. Reichel. Bose–Einstein condensation on a microelectronic chip. *Nature*, 413:498–501, 2001.

[89] B. P. Anderson and M. A. Kasevich. Loading a vapor-cell magneto-optic trap using light-induced atom desorption. *Phys. Rev. A*, 63:023404, 2001.

[90] C. Klempt, T. van Zoest, T. Henninger, O. Topic, E. Rasel, W. Ertmer, and J. Arlt. Ultraviolet light-induced atom desorption for large rubidium and potassium magneto-optical traps. *Phys. Rev. A*, 73:013410, 2006.

[91] A. Hatakeyama, K. Enomoto, N. Sugimoto, and T. Yabuzaki. Atomic alkali-metal gas cells at liquid-helium temperatures: Loading by light-induced atom desorption. *Phys. Rev. A*, 65:022904, 2002.

[92] T. Kinoshita, T. Wenger, and D. S. Weiss. All-optical Bose-Einstein condensation using a compressible crossed dipole trap. *Phys. Rev. A*, 71:011602(R), 2005.

[93] J.-F. Clément, J.-P. Brantut, M. Robert-de Saint-Vincent, R. A. Nyman, A. Aspect, T. Bourdel, and P. Bouyer. All-optical runaway evaporation to Bose-Einstein condensation. *Phys. Rev. A*, 79:061406(R), 2009.

[94] M. Zaiser, J. Hartwig, D. Schlippert, U. Velte, N. Winter, V. Lebedev, W. Ertmer, and E. M. Rasel. Simple method for generating Bose-Einstein condensates in a weak hybrid trap. *Phys. Rev. A*, 83:035601, 2011.

[95] Y.-J. Lin, A. R. Perry, R. L. Compton, I. B. Spielman, and J. V. Porto. Rapid production of $^{87}$Rb Bose-Einstein condensates in a combined magnetic and optical potential. *Phys. Rev. A*, 79:063631, 2009.

[96] D. M. Stamper-Kurn, H.-J. Miesner, A. P. Chikkatur, S. Inouye, J. Stenger, and W. Ketterle. Reversible Formation of a Bose-Einstein Condensate. *Phys. Rev. Lett.*, 81:2194–2197, 1998.

[97] M. C. Garrett, A. Ratnapala, E.D. van Ooijen, C. J. Vale, K. Weegink, S.K. Schnelle, O. Vainio, N. R. Heckenberg, H. Rubinsztein-Dunlop, and M. J. Davis. Growth dynamics of a Bose-Einstein condensate in a dimple trap without cooling. *Phys. Rev. A*, 83:013630, 2011.

[98] D. Jacob, E. Mimoun, L. De Sarlo, M. Weitz, J. Dalibard, and F. Gerbier. Production of sodium Bose-Einstein condensates in an optical dimple trap. *New J. Phys.*, 13:065022, 2011.

[99] R. Folman, P. Krüger, D. Cassettari, B. Hessmo, T. Maier, and J. Schmiedmayer. Controlling Cold Atoms using Nanofabricated Surfaces: Atom Chips. *Phys. Rev. Lett.*, 84:4749–4752, 2000.

[100] D. Müller, E. A. Cornell, M. Prevedelli, P. D. D. Schwindt, A. Zozulya, and D. Z. Anderson. Waveguide atom beam splitter for laser-cooled neutral atoms. *Opt. Lett.*, 25(18):1382–1384, 2000.

[101] D. Cassettari, B. Hessmo, R. Folman, T. Maier, and J. Schmiedmayer. Beam Splitter for Guided Atoms. *Phys. Rev. Lett.*, 85:5483–5487, 2000.

[102] W. Hänsel, J. Reichel, P. Hommelhoff, and T. W. Hänsch. Magnetic Conveyor Belt for Transporting and Merging Trapped Atom Clouds. *Phys. Rev. Lett.*, 86:608–611, 2001.

[103] R. Schmied, D. Leibfried, R. J. C. Spreeuw, and S. Whitlock. Optimized magnetic lattices for ultracold atomic ensembles. *New J. Phys.*, 12(10):103029, 2010.

[104] P. Böhi, M. F. Riedel, J. Hoffrogge, J. Reichel, T. W. Hänsch, and P. Treutlein. Coherent manipulation of BoseEinstein condensates with state-dependent microwave potentials on an atom chip. *Nat. Phys.*, 5:592–597, 2009.

[105] S. Hofferberth, I. Lesanovsky, B. Fischer, J. Verdu, and J. Schmiedmayer. Radiofrequency dressed-state potentials for neutral atoms. *Nat. Phys.*, 2:710, 2006.

[106] B. E. Sherlock, M. Gildemeister, E. Owen, E. Nugent, and C. J. Foot. Time-averaged adiabatic ring potential for ultracold atoms. *Phys. Rev. A*, 83:043408, 2011.

[107] P. F. Griffin, E. Riis, and A. S. Arnold. Smooth inductively coupled ring trap for atoms. *Phys. Rev. A*, 77:051402, 2008.

[108] G.-B. Jo, J. Guzman, C. K. Thomas, P. Hosur, A. Vishwanath, and D. M. Stamper-Kurn. Ultracold Atoms in a Tunable Optical Kagome Lattice. *arXiv*, 1109:1591, 2011.

[109] A. M. Rey, V. Gritsev, I. Bloch, E. Demler, and M. D. Lukin. Preparation and Detection of Magnetic Quantum Phases in Optical Superlattices. *Phys. Rev. Lett.*, 99:140601, 2007.

[110] R. A. Williams, J. D. Pillet, S. Al-Assam, B. Fletcher, M. Shotter, and C. J. Foot. Dynamic optical lattices: two-dimensional rotating and accordion lattices for ultra-cold atoms. *Opt. Express*, 16:16977–16983, 2008.

[111] R. Zhang, N. V. Morrow, P. R. Berman, and G. Raithel. Laser cooling in an optical lattice that employs Raman transitions. *Phys. Rev. A*, 72:043409, 2005.

[112] N. Lundblad, P. J. Lee, I. B. Spielman, B. L. Brown, W. D. Phillips, and J. V. Porto. Atoms in a Radio-Frequency-Dressed Optical Lattice. *Phys. Rev. Lett.*, 100:150401, 2008.

[113] M. Karski, L. Förster, J.-M. Choi, A. Steffen, N. Belmechri, W. Alt, D. Meschede, and A. Widera. Imprinting patterns of neutral atoms in an optical lattice using magnetic resonance techniques. *New Journal of Physics*, 12(6):065027, 2010.

[114] P. Würtz, T. Langen, T. Gericke, A. Koglbauer, and H. Ott. Experimental Demonstration of Single-Site Addressability in a Two-Dimensional Optical Lattice. *Phys. Rev. Lett.*, 103:080404, 2009.

[115] S. K. Schnelle, E. D. van Ooijen, M. J. Davis, N. R. Heckenberg, and H. Rubinsztein-Dunlop. Versatile two-dimensional potentials for ultra-cold atoms. *Opt. Express*, 16(3):1405–1412, 2008.

[116] K. Henderson, C. Ryu, C. MacCormick, and M. G. Boshier. Experimental demonstration of painting arbitrary and dynamic potentials for Bose–Einstein condensates. *New J. Phys.*, 11:043030, 2009.

[117] B. Zimmermann, T. Müller, J. Meineke, T. Esslinger, and H. Moritz. High-resolution imaging of ultracold fermions in microscopically tailored optical potentials. *New J. Phys.*, 13(4):043007, 2011.

[118] D. G. Grier. A revolution in optical manipulation. *Nature*, 424:810–816, 2003.

[119] D. McGloin, G. Spalding, H. Melville, W. Sibbett, and K. Dholakia. Applications of spatial light modulators in atom optics. *Opt. Express*, 11(2):158–166, 2003.

[120] S. Franke-Arnold, J. Leach, M. J. Padgett, D. Lembessis, V. E.and Ellinas, A. J. Wright, J. M. Girkin, P. Ohberg, and A. S. Arnold. Optical ferris wheel for ultracold atoms. *Opt. Express*, 15:8619–8625, 2007.

[121] S. Bergamini, Darquié B., M. Jones, L. Jacubowiez, A. Browaeys, and P. Grangier. Holographic generation of microtrap arrays for single atoms by use of a programmable phase modulator. *J. Opt. Soc. Am. B*, 21:1889–1894, 2004.

[122] D. P. Rhodes, D. M. Gherardi, J. Livesey, D. McGloin, H. Melville, T. Freegarde, and K. Dholakia. Atom guiding along high order Laguerre-Gaussian light beams formed by spatial light modulation. *J. Mod. Opt.*, 53(4):547–556, 2006.

[123] V. Boyer, R. M. Godun, G. Smirne, D. Cassettari, C. M. Chandrashekar, A. B. Deb, Z. J. Laczik, and C. J. Foot. Dynamic manipulation of Bose-Einstein condensates with a spatial light modulator. *Phys. Rev. A*, 73:031402, 2006.

[124] J. Kruse, C. Gierl, M. Schlosser, and G. Birkl. Reconfigurable site-selective manipulation of atomic quantum systems in two-dimensional arrays of dipole traps. *Phys. Rev. A*, 81:060308, 2010.

[125] F. K. Fatemi, M. Bashkansky, and Z. Dutton. Dynamic high-speed spatial manipulation of cold atoms using acousto-optic and spatial light modulation. *Opt. Express*, 15:3589–3596, 2007.

[126] X. He, P. Xu, J. Wang, and M. Zhan. Rotating single atoms in a ring latticegenerated by a spatial light modulator. *Opt. Express*, 17:21007–21014, 2009.

[127] W. S. Bakr, J. I. Gillen, A. Peng, S. Fölling, and M. Greiner. A quantum gas microscope for detecting single atoms in a Hubbard-regime optical lattice. *Nature*, 462:74–77, 2009.

[128] J. F. Sherson, C. Weitenberg, M. Endres, M. Cheneau, I. Bloch, and S. Kuhr. Single-atom-resolved fluorescence imaging of an atomic Mott insulator. *Nature*, 467:68–72, 2010.

[129] G. Whyte and J. Courtial. Experimental demonstration of holographic three-dimensional light shaping using a Gerchberg-Saxton algorithm. *New J. Phys.*, 7:117, 2005.

[130] L. Torralbo-Campo. *A Compact Apparatus for Ultracold Atoms*. PhD thesis, University of St Andrews, 2012.

[131] M. Taglieber, A. C. Voigt, F. Henkel, S. Fray, T. W. Hänsch, and K. Dieckmann. Simultaneous magneto-optical trapping of three atomic species. *Phys. Rev. A*, 73:011402(R), 2006.

[132] S. Bartalini, I. Herrera, L. Consolino, L. Pappalardo, N. Marino, G. D'Arrigo, and F.S. Cataliotti. Full characterization of the loading of a magneto-optical trap from an alkali metal dispenser. *Eur. Phys. J. D*, 36:101–104, 2005.

[133] K. L. Moore, T. P. Purdy, K. W. Murch, S. Leslie, S. Gupta, and D. M. Stamper-Kurn. Collimated, single-pass atom source from a pulsed alkali metal dispenser for laser-cooling experiments. *Rev. Sci. Intstrum.*, 76:023106, 2005.

[134] S. Haslinger, R. Amsuess, Ch. Koller, C. Hufnagel, N. Lippok, J. Majer, J. Verdu, S. Schneider, and J. Schmiedmayer. Electron beam driven alkali metal atom source for loading a magneto-optical trap in a cryogenic environment. *Appl. Phys. B*, 102:819–823, 2010.

[135] T. Esslinger, I. Bloch, and T. W. Hänsch. Bose-Einstein condensation in a quadrupole-Ioffe-configuration trap. *Phys. Rev. A*, 58:R2664–R2667, 1998.

[136] L. Brandt, C. Muldoon, T. Thiele, J. Dong, E. Brainis, and A. Kuhn. Spatial light modulators for the manipulation of individual atoms. *Appl. Phys. B*, 102:443, 2011.

[137] V. Boyer, C. M. Chandrashekar, Z. J. Laczik, and C. J. Foot. Dynamic optical trap generation using FLC SLMs for the manipulation of cold atoms. *J. Mod. Opt.*, 51:2235, 2004.

[138] M. A. Seldowitz, J. P. Allebach, and D. W. Sweeney. Synthesis of digital holograms by direct binary search. *Appl. Opt.*, 26:2788–2798, 1987.

[139] M. Clark and R. Smith. A direct-search method for the computer design of holograms. *Opt. Commun.*, 124:150, 1996.

[140] M. Mitchell. *An Introduction to Genetic Algorithms*. MIT Press, Cambridge, MA, 1998.

[141] R. W. Gerchberg and W. O. Saxton. A practical algorithm for the determination of the phase from image and diffraction plane pictures. *Optik*, 35:237–246, 1972.

[142] V. Soifer, V. Kotlyar, and L. Doskolovich. *Iterative Methods for Diffractive Optical Elements Computation*. Taylor & Francis, Bristol, PA, 1997.

[143] M. Pasienski and B. DeMarco. A high-accuracy algorithm for designing arbitrary holographic atom traps. *Opt. Express*, 16:2176, 2008.

[144] M. Pasienski. *Transport Properties Of Ultracold Atoms In A Disordered Optical Lattice*. PhD thesis, University of Illinois at Urbana-Champaign, 2011.

[145] C. Henkel, P. Krüger, R. Folman, and J. Schmiedmayer. Fundamental limits for coherent manipulation on atom chips. *Appl. Phys. B*, 76:173, 2003.

[146] V. G. Rousseau, G. G. Batrouni, D. E. Sheehy, J. Moreno, and M. Jarrell. Pure Mott phases in confined ultracold atomic systems. *Phys. Rev. Lett.*, 104:167201, 2010.

[147] J.-S. Bernier, Ch. Kollath, A. Georges, L. De Leo, F. Gerbier, C. Salomon, and M. Köhl. Cooling fermionic atoms in optical lattices by shaping the confinement. *Phys. Rev. A*, 79:061601, 2009.

[148] T. Kinoshita, T. Wenger, and D. S. Weiss. Observation of a One-Dimensional Tonks-Girardeau Gas. *Science*, 305:1125, 2004.

[149] E. Kaminishi, R. Kanamoto, J. Sato, and T. Deguchi. Exact yrast spectra of cold atoms on a ring. *Phys. Rev. A*, 83:031601, 2011.

[150] B. Olmos and I. Lesanovsky. Rydberg rings. *Phys. Chem. Chem. Phys.*, 13:4208, 2011.

[151] W. Zhang, L. Li, and W. Guo. Hard core bosons on the dual of the bowtie lattice. *Phys. Rev. B*, 82:134536, 2010.

[152] P. Soltan-Panahi, J. Struck, P. Hauke, A. Bick, W. Plenkers, C. Meineke, G. and-Becker, P. Windpassinger, M. Lewenstein, and K. Sengstock. Multi-component quantum gases in spin-dependent hexagonal lattices. *Nat. Phys.*, 7:434, 2011.

[153] D. Solenov and D. Mozyrsky. Macroscopic two-state systems in trapped atomic condensates. *Phys. Rev. A*, 82:061601, 2010.

[154] A. L. Gaunt and Z. Hadzibabic. Robust Optical Sculpting For Manipulating Ultracold Atoms. *arXiv*, 1111:5941, 2011.

[155] J. Liang, R. N. Kohn Jr, M. F. Becker, and D. J. Heinzen. 1.5% root-mean-square flat-intensity laser beam formed using a binary-amplitude spatial light modulator. *Appl. Opt.*, 48:1955–1962, 2009.

[156] M. R. Andrews, M.-O. Mewes, N. J. van Druten, D. S. Durfee, D. M. Kurn, and W. Ketterle. Direct, Nondestructive Observation of a Bose Condensate. *Science*, 273:84–87, 1996.

[157] W. Ketterle, D. S. Durfee, and D. M. Stamper-Kurn. Making, probing and understanding Bose–Einstein condensates. In M. Inguscio, S. Stringari, and C. E. Wieman, editors, *Bose–Einstein Condensation in Atomic Gases*, Proceedings of the International School of Physics "Enrico Fermi", Course CXL, pages 67–176, Amsterdam, 1999. IOS Press.

[158] L. D. Landau and E. M. Lifshitz. *Mechanics*. Butterworth-Heinemann, 1993.

[159] W. Ketterle and N. J. van Druten. Evaporative cooling of atoms. In Benjamin Bederson and Herbert Walther, editors, *Advances in Atomic, Molecular, and Optical Physics*, volume 37, pages 181–236. Academic Press, 1996.

[160] K. M. O'Hara, M. E. Gehm, S. R. Granade, and J. E. Thomas. Scaling laws for evaporative cooling in time-dependent optical traps. *Phys. Rev. A*, 64:051403, 2001.

[161] T. A. Savard, K. M. O'Hara, and J. E. Thomas. Laser-noise-induced heating in far-off resonance optical traps. *Phys. Rev. A*, 56:R1095–R1098, 1997.

[162] A. Marte, T. Volz, J. Schuster, S. Dürr, G. Rempe, E. G. M. van Kempen, and B. J. Verhaar. Feshbach Resonances in Rubidium 87: Precision Measurement and Analysis. *Phys. Rev. Lett.*, 89:283202, 2002.

[163] F. Dalfovo, S. Giorgini, L. P. Pitaevskii, and S. Stringari. Theory of Bose-Einstein condensation in trapped gases. *Rev. Mod. Phys.*, 71:463–512, 1999.

[164] J. L. Roberts, N. R. Claussen, J. P. Burke Jr, C. H. Greene, E. A. Cornell, and C. E. Wieman. Resonant magnetic field control of elastic scattering in cold $^{85}$Rb. *Phys. Rev. Lett.*, 81:5109–5112, 1998.